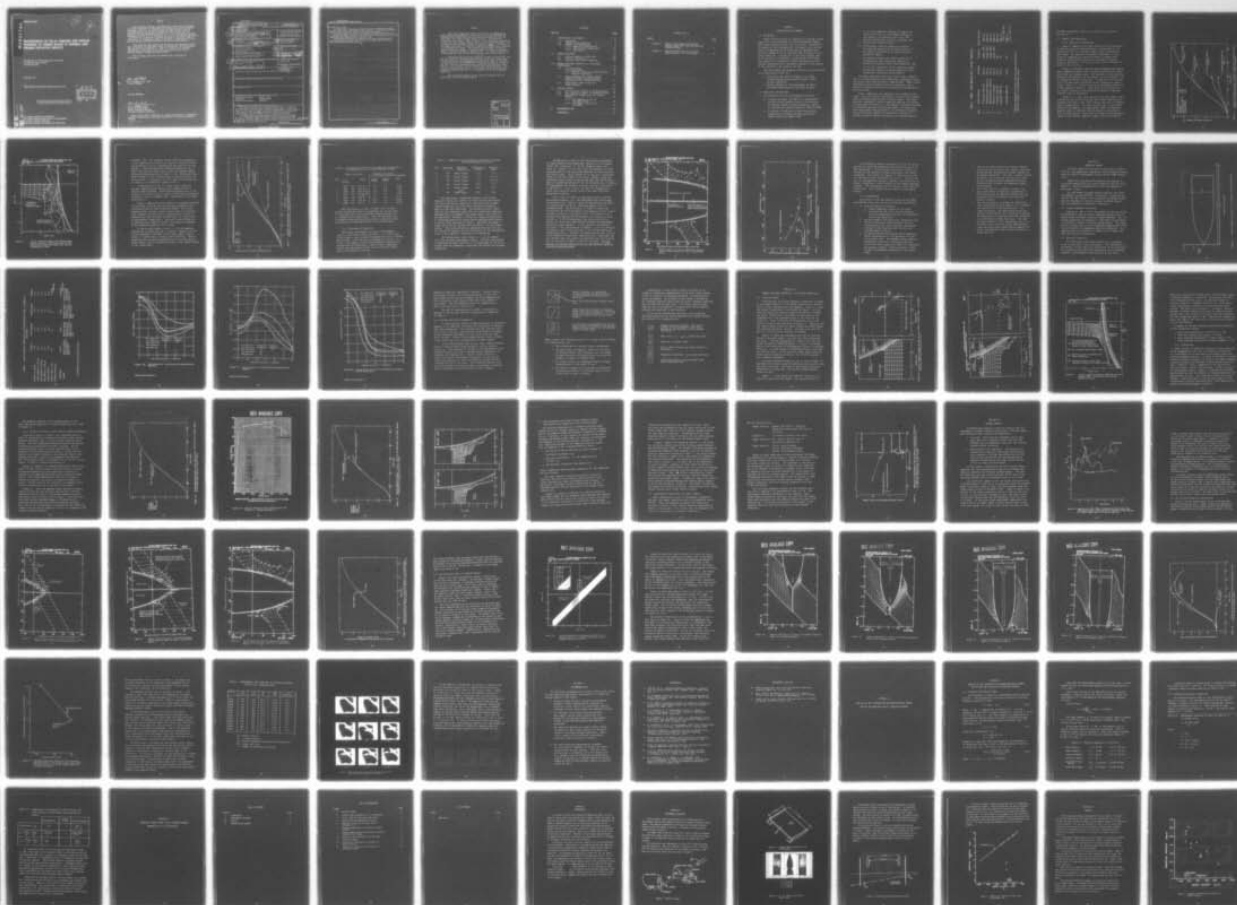


UNCLASSIFIED

F/G 21/5

1 OF 2

ADA041780



AD A 041 780

AFML-TR-76-208

20

J

**INVESTIGATION OF LOCAL DAMAGE AND IMPULSE
DELIVERED TO TURBINE BLADES BY NORMAL AND
OBLIQUE PROJECTILE IMPACTS**

**UNIVERSITY OF DAYTON RESEARCH INSTITUTE
300 COLLEGE PARK AVENUE
DAYTON, OH 45469**

JANUARY 1977

FINAL REPORT FOR PERIOD ENDING JUNE 30, 1976

DDC
RECEIVED
JUL 18 1977
A

Approved for public release; distribution unlimited

AD No. —
DDC FILE COPY

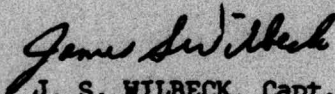
**AIR FORCE MATERIALS LABORATORY
AIR FORCE WRIGHT AERONAUTICAL LABORATORIES
AIR FORCE SYSTEMS COMMAND
WRIGHT-PATTERSON AIR FORCE BASE, OHIO 45433**

NOTICE

When Government drawings, specifications, or other data are used for any purpose other than in connection with a definitely related Government procurement operation, the United States Government thereby incurs no responsibility nor any obligation whatsoever; and the fact that the government may have formulated, furnished, or in any way supplied the said drawings, specifications, or other data, is not to be regarded by implication or otherwise as in any manner licensing the holder or any other person or corporation, or conveying any rights or permission to manufacture, use, or sell any patented invention that may in any way be related thereto.

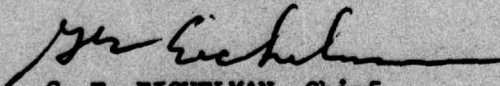
This report has been reviewed and cleared for open publication and/or public release by the appropriate Office of Information (OI) in accordance with AFR 190-170 and DODD 5230.9. There is no objection to unlimited distribution of this report to the public at large or by DDC to the National Technical Information Service (NTIS).

This technical report has been reviewed and is approved for publication.



J. S. WILBECK, Capt. USAF
Project Engineer

FOR THE COMMANDER



G. E. EICHELMAN, Chief
Metals Behavior Branch
Metals & Ceramics Division
Air Force Materials Laboratory

Copies of this report should not be returned unless return is required by security considerations, contractual obligations, or notice on a specific document.

UNCLASSIFIED

SECURITY CLASSIFICATION OF THIS PAGE (When Data Entered)

19 REPORT DOCUMENTATION PAGE		READ INSTRUCTIONS BEFORE COMPLETING FORM	
1. REPORT NUMBER AFML-TR-76-208	2. GOVT ACCESSION NO.	3. RECIPIENT'S CATALOG NUMBER	
4. TITLE (and Subtitle) INVESTIGATION OF LOCAL DAMAGE AND IMPULSE DELIVERED TO TURBINE BLADES BY NORMAL AND OBLIQUE PROJECTILE IMPACTS.		5. TYPE OF REPORT & PERIOD COVERED Final Report for Period Ending June 30, 1976	
6. AUTHOR(s) M./Rosenblatt, T. R./Isbelle, (CRT) P. F./Fry, J. P./Barber, H. R./Taylor (UDRI)		7. PERFORMING ORG. REPORT NUMBER	
8. PERFORMING ORGANIZATION NAME AND ADDRESS University of Dayton 300 College Park Avenue Dayton OH 45469		9. CONTRACT OR GRANT NUMBER(s) F33615-75-C-5052	
10. CONTROLLING OFFICE NAME AND ADDRESS Air Force Materials Laboratory (LLN) Wright-Patterson AFB OH 45433		10. PROGRAM ELEMENT, PROJECT, TASK AREA & WORK UNIT NUMBERS 7351 735106, 735106A1	
11. MONITORING AGENCY NAME & ADDRESS (if different from Controlling Office) Final rept. Jan 75 - Jul 76		11. REPORT DATE January 1977	
12. DISTRIBUTION STATEMENT (of this Report) Approved for public release; distribution unlimited.		12. NUMBER OF PAGES 78	
13. DISTRIBUTION STATEMENT (of the abstract entered in Block 20, if different from Report)		13. SECURITY CLASS. (of this report) UNCLASSIFIED	
14. SUPPLEMENTARY NOTES		14a. DECLASSIFICATION/DOWNGRADING SCHEDULE	
15. KEY WORDS (Continue on reverse side if necessary and identify by block number) Foreign Object Damage Computer Codes Fan Blades Oblique Impacts Numerical Calculations Composites			
16. ABSTRACT (Continue on reverse side if necessary and identify by block number) Jet engine fan blades can be damaged by bullet impacts, or damage can occur when debris from the runway is ingested by the engine. Often, the impact can cause the fan blade to break into fragments which are also ingested by the engine. The local damage and impulse characteristics delivered to simulated blades from .50-caliber projectile impacts are examined. A combined approach involving numerical calculations and experiments is used to investigate damage and momentum transfer mechanisms for normal and oblique projectile impacts on Titanium, Aluminum, Boron-Aluminum, and			

DD FORM 1 JAN 73 1473

EDITION OF 1 NOV 63 IS OBSOLETE

UNCLASSIFIED

SECURITY CLASSIFICATION OF THIS PAGE (When Data Entered)

OVER NEXT PAGE

UNCLASSIFIED

SECURITY CLASSIFICATION OF THIS PAGE(When Data Entered)

Graphite-Epoxy plates.

The normal impact calculations compare well with the experimental results. The major uncertainty in axisymmetric impact problems is in determining realistic dynamic material properties, especially for composite materials.

The oblique impact experiments and numerical calculations demonstrate the fundamental importance of projectile yaw and rotation in determining the projectile-target damage and momentum transfer characteristics.

Blade material ductility, and compressive and tensile strengths are the most important material properties involved in fan blade damage and momentum transfer from hard projectile impacts.

PREFACE

A031 761
This report summarizes research conducted by the University of Dayton Research Institute with a subcontract to California Research and Technology for the Air Force Materials Laboratory, Wright-Patterson Air Force Base, Ohio, under Contract F33615-75-C-5052. The program was divided into three phases. Work on Phase I of this contract was presented in AFML-TR-76-34, entitled "Ordnance Impacts on Jet Engine Fan Blades". The experimental work performed in Phase II, entitled "Impact of Soft Bodies on Jet Engine Fan Blades", is presented in UDRI-TR-76-33, ^{NR} and will be published as an AFML Technical Report. The numerical work performed in Phase II, entitled "Numerical Analyses of Soft Body Impacts on Rigid and Deformable Targets", has been presented in AFML-TR-76-202. This report describes the work performed in Phase III and summarizes much of the work of Phase I.

A040030
This contractual effort was conducted in support of Project No. 7351 and Task 735106 for the Metals Behavior Branch of the Metals and Ceramics Division during the period January 1975 to July 1976. Part of this work, concerned with ballistic perforation of engine fan blading, was funded by the Joint Technical Coordinating Group for Aircraft Survivability, under Project 5.1.2.9 entitled, "Fan and Turbine Blade Damage Tolerance". This work was jointly monitored by Mr. J. M. Frederick of the Air Force Aero Propulsion Laboratory and Capt. J. S. Wilbeck of the Air Force Materials Laboratory.

This report was submitted by the authors in February 1977 for publication as an AFML Technical Report.

ACCESSION for	
NRIS	White Section <input checked="" type="checkbox"/>
DOC	Buff Section <input type="checkbox"/>
UNANNOUNCED	<input type="checkbox"/>
JUSTIFICATION.....	
BY	
DISTRIBUTION/AVAILABILITY CODES	
Dist.	AVAIL. and/or SPECIAL
A	

CONTENTS

<u>Section</u>	<u>Page</u>
I. INTRODUCTION AND SUMMARY	1
1.1 Background.	1
1.2 Objective and Approach.	1
1.3 Summary and Conclusions	4
1.3.1 Numerical Calculations	4
1.3.2 Experimental Comparisons	11
1.3.3 Conclusions.	16
II. NUMERICAL METHOD	18
2.1 Initial Geometric Conditions.	18
2.2 Material Properties	18
2.3 Fracture and Crack Propagation.	26
III. NORMAL-INCIDENCE IMPACTS OF .50-CALIBER PROJECTILES.	29
3.1 Titanium Blades	29
3.1.1 Zoning Test	33
3.1.2 Effects of Brittle versus Ductile Tensile Properties.	36
3.2 Boron-Aluminum and Graphite-Epoxy Composite Blades and Quantitative Comparisons with Titanium Blades.	41
3.3 Experimental Comparisons for Normal Impacts.	42
IV. OBLIQUE IMPACTS.	45
4.1 60° Projectile Impact on Titanium Blade	47
4.2 45° Projectile Impact on Aluminum Plates.	54
4.3 Experimental Comparisons for Oblique Impacts	63
4.3.1 60° Impacts on 1/8-in. Titanium Plates.	63
4.3.2 45° Impacts on 1/2-in. Aluminum	63
V. RECOMMENDATIONS.	69
REFERENCES	70

CONTENTS (Cont'd)

Section	Page
INTRODUCTION AND SUMMARY	1
APPENDIX A	1
DETAILS OF THE TITANIUM AND ALUMINUM	1
MATERIAL MODELS AND OF THE SEMI-ELLIPTICAL	1
COORDINATE METHOD.	72
APPENDIX B	18
PROJECTILE IMPACT ONTO THICK ALUMINUM	18
TARGETS MOUNTED AT 45° TO TRAJECTORY	79
III. NORMAL IMPACTS OF .50-CALIBER	18
PROJECTILES	18
3.1 Titanium Plates	18
3.1.1 Loading Test	18
3.1.2 Effects of Projectile Velocity	18
3.1.3 Projectile Properties	18
3.2 Boron-Aluminum and Graphite-Epoxy	18
3.2.1 Composite Plates and Quantities	18
3.2.2 Composites with Titanium Plates	18
3.2.3 Experimental Comparison for	18
Normal Impacts	18
IV. OBLIQUE IMPACTS	18
4.1 60° Projectile Impact on Titanium Plate	18
4.2 45° Projectile Impact on Aluminum Plates	18
4.3 Experimental Comparisons for Oblique	18
Impacts	18
4.3.1 60° Impact on 1/8-in.	18
Titanium Plates	18
4.3.2 45° Impact on 1/8-in.	18
Aluminum	18
V. RECOMMENDATIONS	18
REFERENCES	18

SECTION I

INTRODUCTION AND SUMMARY

1.1 Background

Impacts of projectiles or fragments on rotating turbine blades can cause substantial or even catastrophic damage. Such impacts produce severe local distortion. Depending on the nature of the blade material, the impact site, and the relative dimensions of the blade and the impacting body, the local damage may be so extensive that a portion of the blade breaks off. In addition to such local damage, some of the projectile's momentum is transferred to the blade. This impulse will dynamically deflect the blade, possibly causing interference with stationary elements of the engine, or even failure of the blade at the hub.

The local damage and momentum transfer to the blade need to be understood in order to:

- o help assess the possible damage to an engine or blade design from projectile impacts under various conditions
- o provide guidance in the development of impact-resistant blade materials and blade designs.

1.2 Objectives and Approach

The objectives of this investigation have been:

- a. To adapt and apply the WAVE-L 2-D hydrodynamic-elastic-plastic numerical code to the analyses of specific normal-incidence projectile impacts on titanium and composite material turbine blades.
- b. To develop a technique for more realistically simulating 3-D oblique-incidence projectile impacts within the WAVE-L code.

- c. To use these numerical methods to examine the *nature* and *extent* of local damage produced by such impacts, including the *hole size*, and *material deformation, fracture, cracking, and delamination* around the hole.
- d. To determine, from the numerical solutions, the time-and space-resolved characteristics of the impulse delivered to the blade from the projectile impact.
- e. By comparing results of several solutions, to determine how local damage and impulse are affected by different basic blade materials, and
- f. To test the credibility of the numerical method and material models by making comparisons with independent experimental observations.

The basic numerical code used in this study is WAVE-L. This is a general-purpose, two-dimensional Lagrangian finite-difference code based on Wilkin's HEMP method¹. WAVE-L treats hydrodynamic-elastic-plastic material properties, and in addition, contains provisions for treating the propagation of explicit cracks.

Table 1 summarizes the numerical cases treated in this study. All cases involve .50-caliber core projectile impacts onto flat plates which represent turbine blades. The blade material properties, and the numerical modeling of fracture are described in Section II. The numerical solutions obtained by California Research & Technology (CRT), and comparisons with experimental data obtained by the University of Dayton Research Institute (UDRI) are discussed in Section III (normal incidence impacts) and Section IV (oblique impacts).

TABLE 1. IMPACT CASES ANALYZED FOR A .50-CAL. PROJECTILE

CASE	BLADE MATERIAL	THICKNESS	OBLIQUITY	IMPACT VELOCITY
1	*TITANIUM (6-AL-4V)	1/8-IN.	NORMAL (90°)	1600 FPS
2	BORON-ALUMINUM COMPOSITE	1/8-IN.	NORMAL (90°)	1600 FPS
3	GRAPHITE-EPOXY COMPOSITE	1/8-IN.	NORMAL (90°)	1600 FPS
4	"BRITTLE" TITANIUM	1/8-IN.	NORMAL (90°)	1600 FPS
5	TITANIUM (6-AL-4V)	1/8-IN.	60°	1600 FPS
6	ALUMINUM (6061-T6)	1/2-IN.	45°	1665 FPS (V ₅₀ + 100 FPS)
7	ALUMINUM (6061-T6)	1/2-IN.	45°	1886 FPS (V ₅₀ + 321 FPS)

* ANALYSES PERFORMED WITH BOTH FINE AND COARSE RESOLUTION TO EVALUATE ADEQUACY OF COMPUTATIONAL ZONING

The UDRI experimental reports are contained in Appendix B and Reference 14.

1.3 Summary and Conclusions

1.3.1 Numerical Calculations

Figure 1 summarizes the time histories of the percentage of initial projectile momentum which is transferred to the target plate for all the normal impact cases calculated in this study. The important influence of ductility is illustrated by comparing the curves for Case 1 (Titanium with realistic 10% ductility) and Case 4 ("brittle" Titanium, having no ductility). Ten percent ductility increases the momentum transfer by about 50 percent.

Figure 1 illustrates that the Boron-Aluminum and Graphite-Epoxy composites (Cases 2 and 3) behave quantitatively differently than the Titanium cases. The *ductility* of the realistic Titanium is responsible for the longer time to "decouple" from the projectile-target interaction. In addition, the *compressive yield* and *tensile strengths* of the Titanium are approximately a factor of 3 greater than the corresponding properties of the composite materials. These material characteristics are clearly important in determining the amount of momentum transfer from the projectile.

Figures 2, 3, and 4 show the projectile and target configurations at the end of the normal (90°) impact numerical calculations for Case 1 (Ti), Case 2 (B-Al), and Case 3 (Graphite-Epoxy), respectively. The right vertical axis is the projectile axis of symmetry. The approximate region of fractured material which is detached from the target is indicated on each of these figures. Note that this region is substantially larger in the brittle composite targets than in the ductile

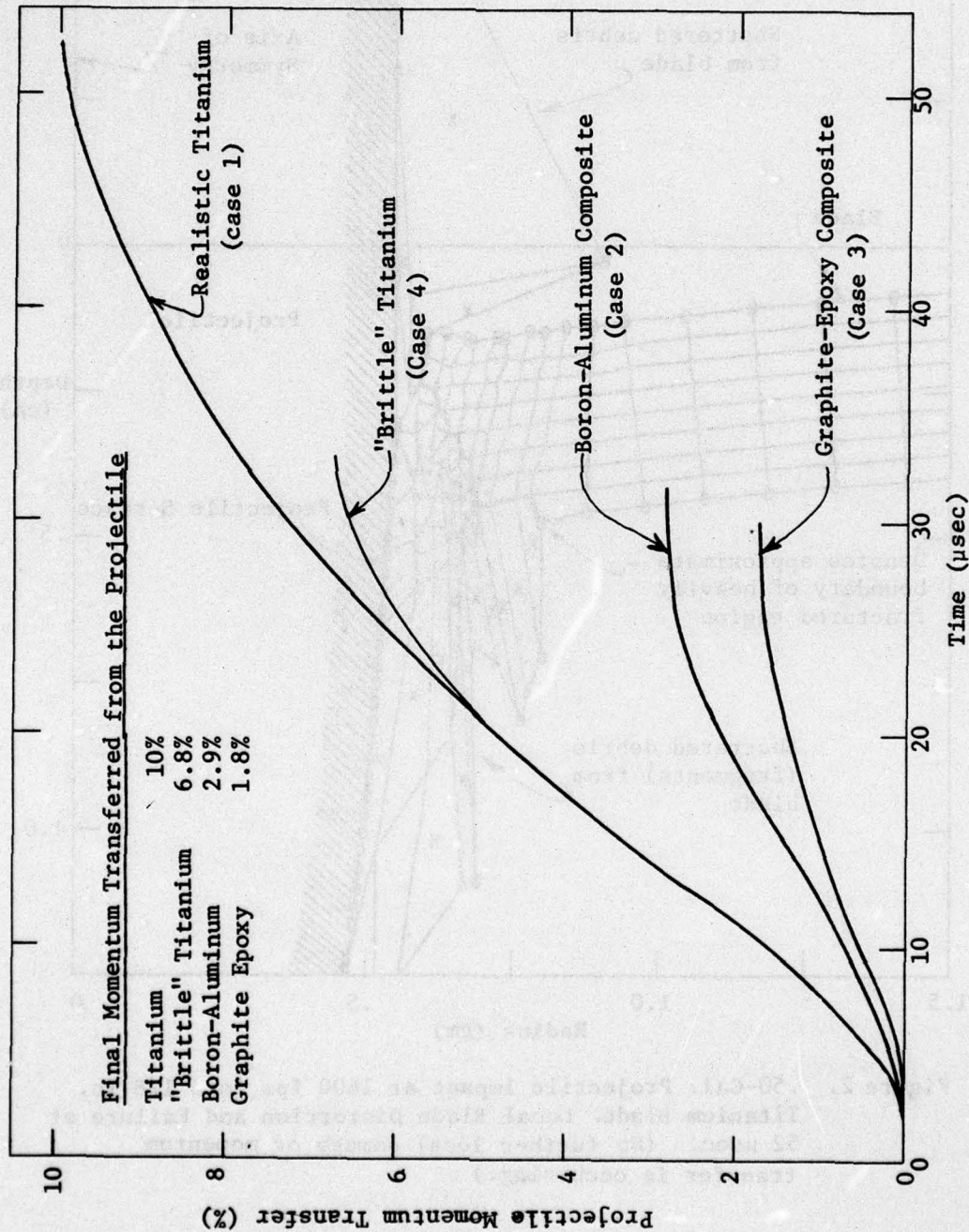


Figure 1. Comparison Showing Transfer of Projectile Momentum to Different Blade Materials by 1600 fps Normal Impact of .50-Cal. Projectile

CALIFORNIA RESEARCH AND TECHNOLOGY WAVE-L CODE
 RUN NO 2070-CASE 4 DUC RIGID BODY PENETRATION INTO TITANIUM
 CYCLE 4972

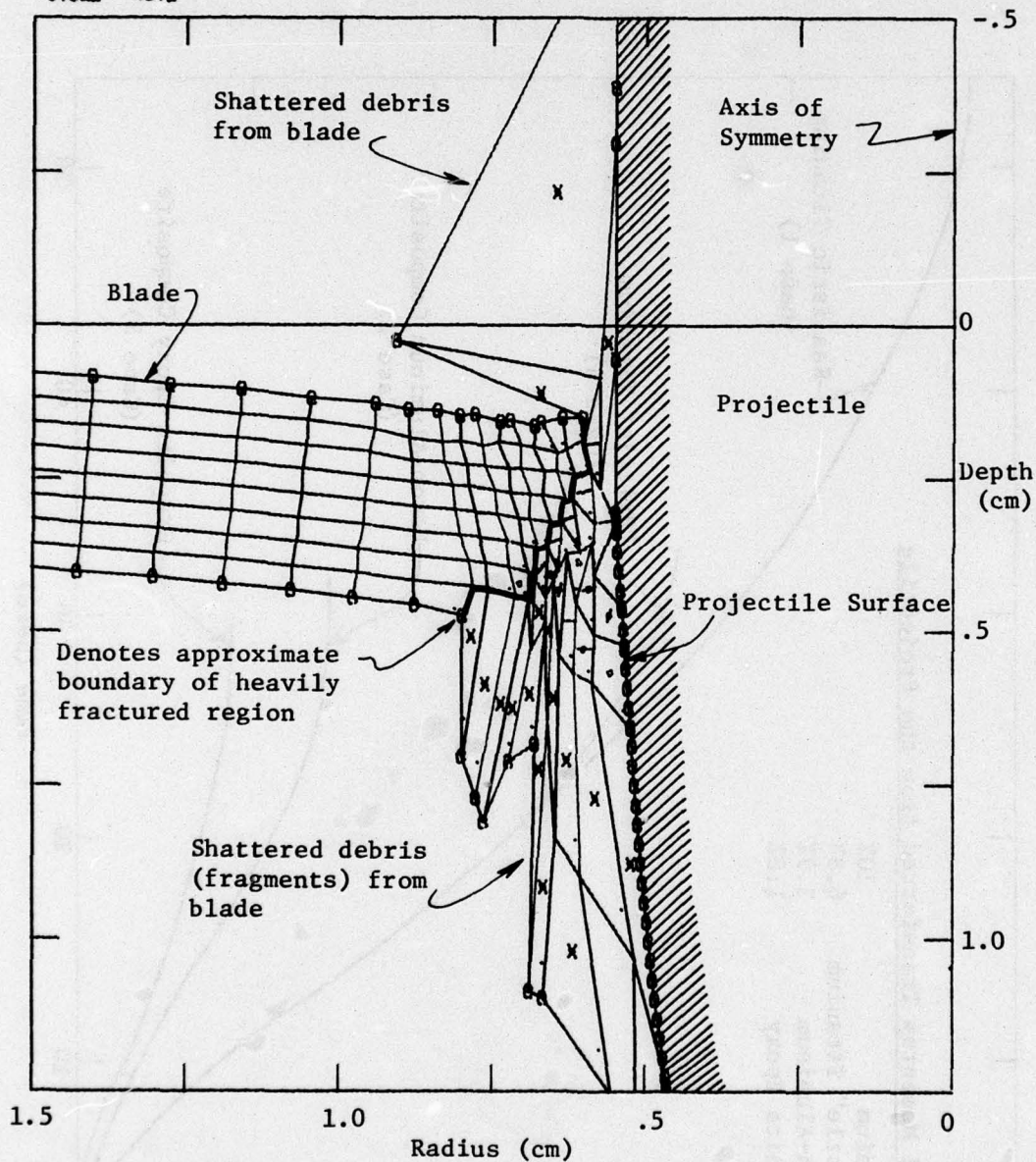


Figure 2. .50-Cal. Projectile Impact at 1600 fps into 1/8 in. Titanium Blade. Local Blade Distortion and Failure at 52 μ sec. (No further local damage or momentum transfer is occurring.)

CALIFORNIA RESEARCH AND TECHNOLOGY WAVE-L CODE
 RUN NO 2070-CASE 2 RIGID BODY PENETRATION INTO B/AL
 CYCLE 2249

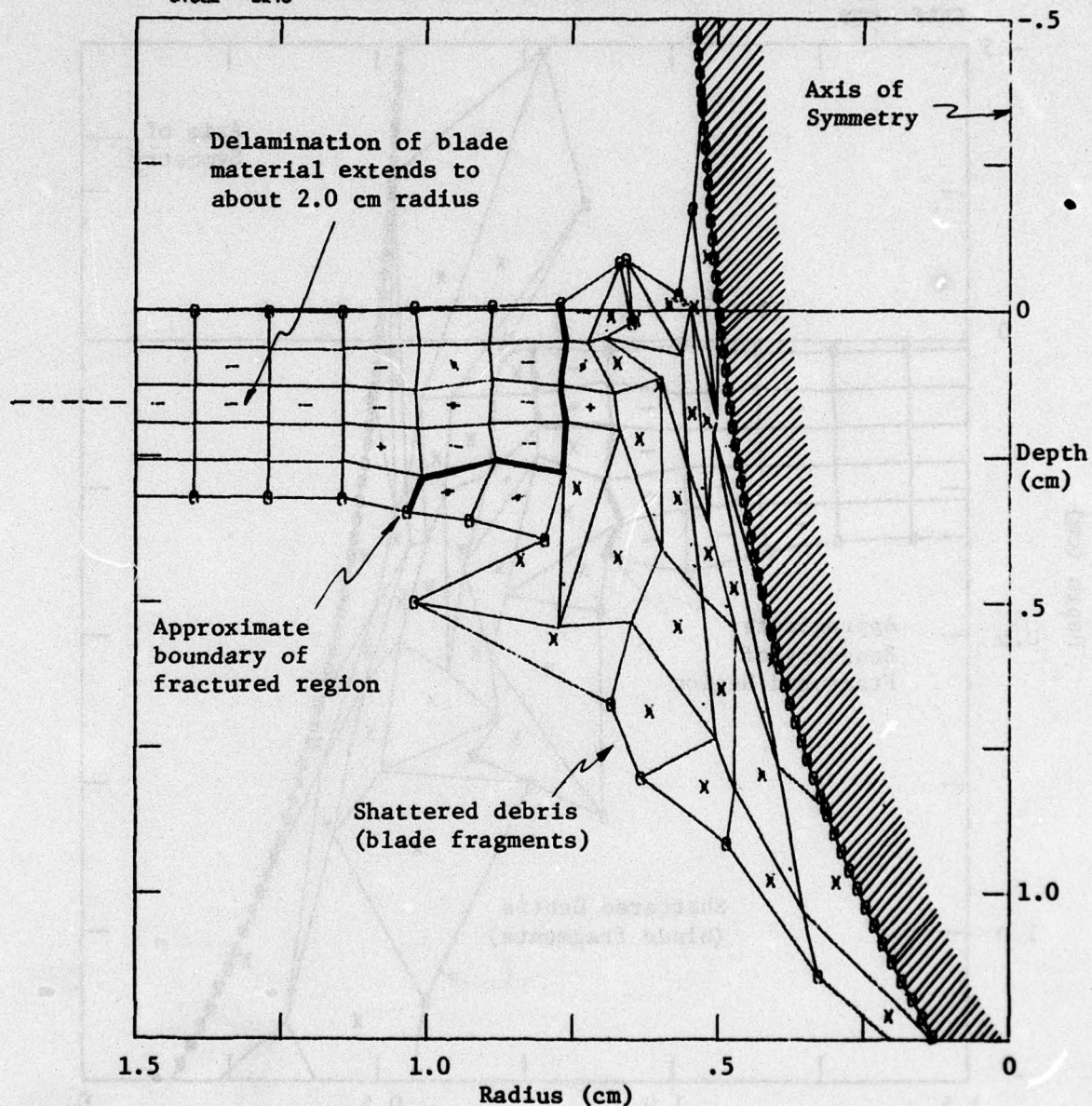


Figure 3. .50-Cal. Projectile Impact into B-Al Blade at 1600 fps. Grid Distortion at 30 μ sec Showing Heavily-Shattered Region Near Hole and Delamination of Blade Extending out from Hole. (Material is strongly anisotropic and is weak in depth direction)

05 APR 76 CALIFORNIA RESEARCH AND TECHNOLOGY WAVE-L CODE
 RUN NO 2070-CASE 9 RIGID BODY PENETRATION INTO GRAPHITE-EPOXY
 CYCLE 2076

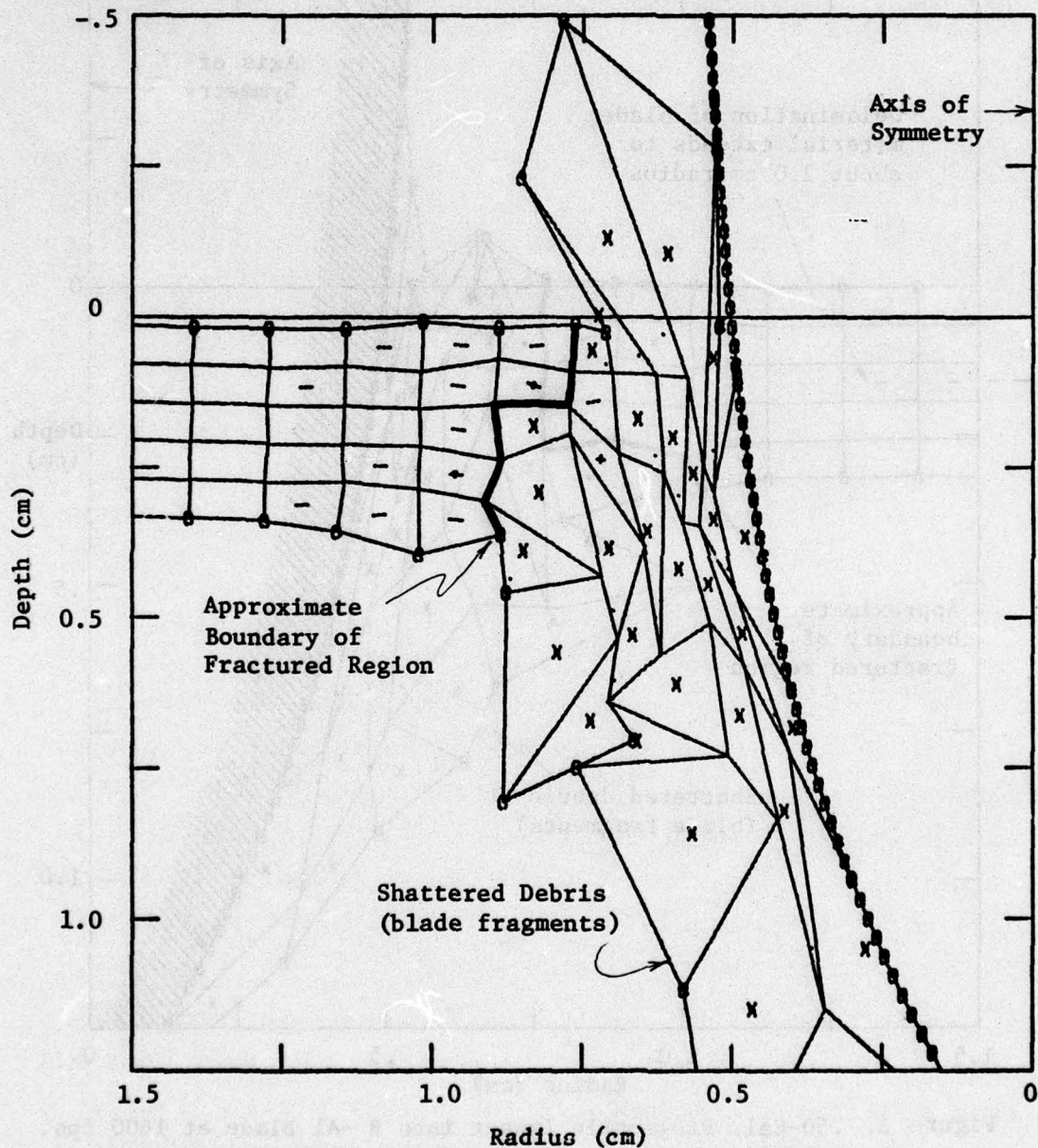


Figure 4. .50 Cal. Projectile Impact into Graphite/Epoxy Blade at 1600 fps. Grid Distortion at 31 usec Showing Heavily-Shattered Region Near Hole and Delamination of Blade.

Titanium. Also, the composite plates suffered delamination, or ply separation, even beyond the region of severe fracture. (An anisotropic tensile strength model was used for the composites.) The Boron-Aluminum suffered delamination out to about 2 cm from the impact point, while the Graphite-Epoxy exhibited delamination out to about 1.2 cm. The greater momentum transfer to the Titanium plate as compared to the composite plates is responsible for the larger plate deflection in Figure 2, as compared to Figures 3 and 4.

A modification of the 2-D plane strain equations has been completed which improves the simulation of 3-D oblique impact problems. This modified approach uses a *semi-elliptical coordinate method* in place of the usual cylindrical coordinates of the 2-D WAVE-L code. The method is described in Section 4.1.

Figure 5 compares the time histories of momentum transfer to the target plate for the three oblique-incidence cases calculated using the semi-elliptical method. The 1/2-in. Aluminum plates in Cases 6 and 7 receive more of the projectiles' momenta than the 1/8-in. Titanium plate in Case 5. (Aluminum was used for these thicker plates to reduce costs of experimental comparisons.) The lower velocity impact on an Aluminum plate (Case 6) transfers the largest percentage of the projectile momentum to the target.

In constructing Figures 1 and 5, *all* of the momentum transferred to target material is plotted. However, not all of this momentum is retained in the target plate, since a portion is carried away in target debris material. Table 2 summarizes the calculated momentum which is carried away in target debris, and the momentum retained in the intact portion of the target plate.

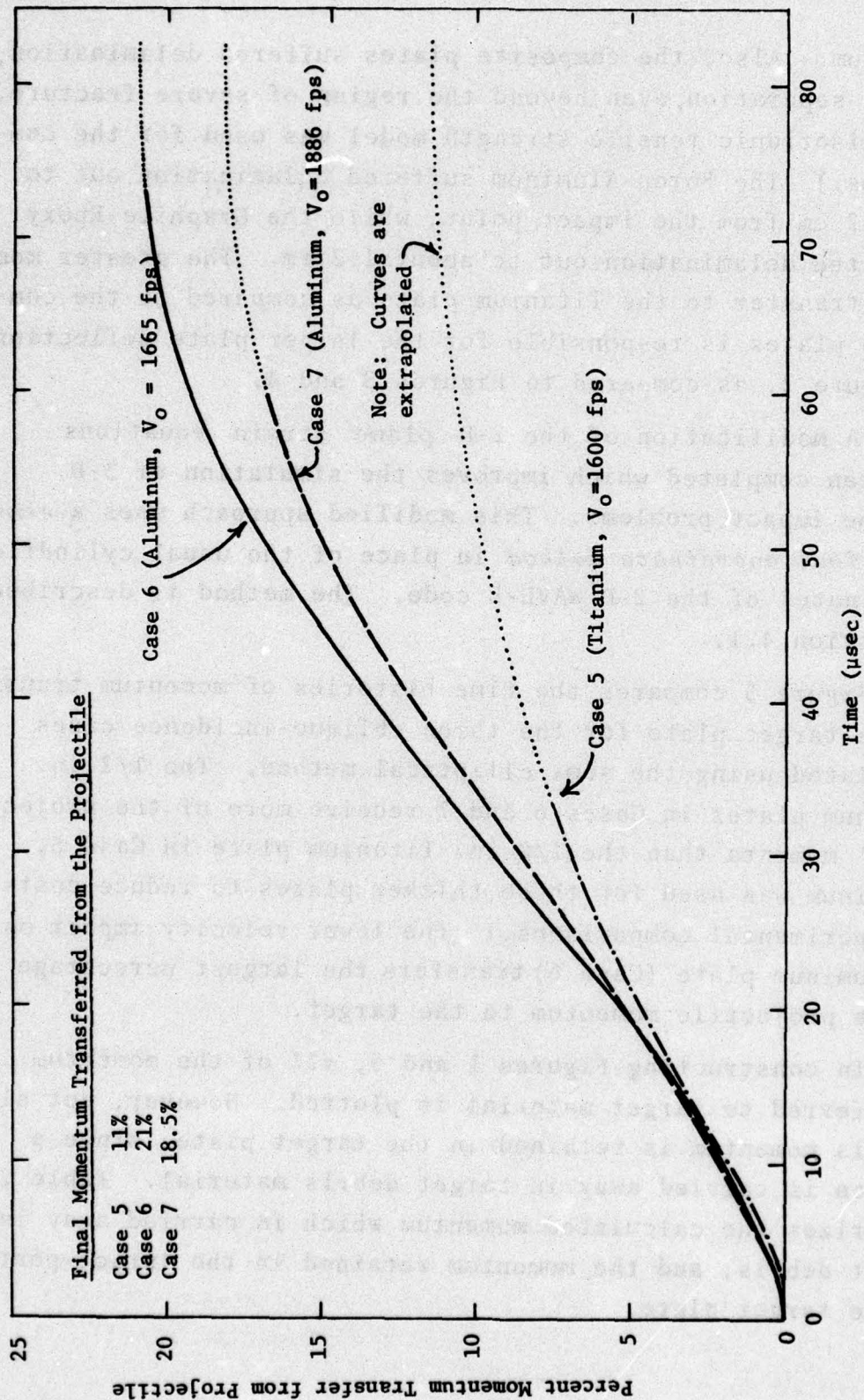


Figure 5. Comparison Showing Transfer of Projectile Momentum to a 1/8-in. Titanium Blade at 60° Obliquity and to two 1/2-in. Aluminum Blades at 45° Obliquity.

Table 2. Percentage of Projectile Axial Momentum Transferred to Target Debris and to Intact Portion of Plate

Case	Impact Conditions			Momentum Transferred (% of Initial Projectile Momentum)		
	V_o (ft/sec)	θ	Target	Intact Target	Target Debris	Total
1	1600	90°	1/8" Ti	8.2	1.8	10.0%
2	1600	90°	1/8" B-Al	1.0	1.9	2.9%
3	1600	90°	1/8" Gr-Ep	0.5	1.3	1.8%
4	1600	90°	1/8" Brittle Ti	2.3	4.5	6.8%
5	1600	60°	1/8" Ti	9.0	2.0	11.0%
6	1655	45°	1/2" Al	20.0	1.0	21.0%
7	1886	45°	1/2" Al	16.0	2.5	18.5%

Note that Cases 2, 3, and 4 in Table 2 use an ideal brittle failure model which is responsible for the fact that in those cases most of the transferred momentum (about 70%) is trapped in the target debris. Thus, any uncertainty in the amount of material ductility can have an important effect on predictions of momentum transfer to the intact target.

1.3.2 Experimental Comparisons

Experimental measurements were made of the momentum transfer to the intact targets for Cases 1, 2, 3, and 5, and of the change in total projectile momentum for the 1/2" Aluminum Cases 6 and 7. (For some shots corresponding to Cases 1, 2, 3, and 5, the change in projectile momentum was measured, but the data were not consistent.) Table 3 shows a comparison between the experimental results and the predicted results based on the numerical solutions.

Table 3. Comparison of Experimental and Numerical Results
for Percent Momentum Transfer

Case	Obliquity	Momentum Transfer to	Experimental Value	Numerical Value
1	90°	Intact Target	7.6	8.2
2	90°	Intact Target	3.0	1.0-2.9
3	90°	Intact Target	1.0	0.5-1.8
5	60°	Intact Target	10.8	9.0
6	45°	Intact Target	38.0	21.0
7	45°	plus Target Debris	26.0	18.5

The predictions of momentum transfer to the intact *composite targets* are somewhat uncertain because the compressive yield and failure properties, especially under dynamic loading conditions, for both Boron-Aluminum and Graphite-Epoxy are not well understood. The perfectly brittle models used for both composites imply that the numerically predicted momentum which is trapped in the target debris (see Table 2) was maximized. Therefore, in Table 3, a range of uncertainty is indicated, based on the target debris momentum being between 0 and the value indicated in Table 2. Note that the experimental values do not include error estimates; the experiments exhibit some inconsistencies, especially with the B-Al and 45° oblique Al targets, but the exact nature of the experimental error is not completely understood (see Appendix B).

The normal impact cases (Cases 1, 2, and 3) compare well with the UDRI experimental results. The major uncertainty in *axisymmetric impact problems* is in determining the realistic dynamic material properties, especially the failure and strength properties.

As indicated in Table 3, the semi-elliptical technique for approximating three-dimensional behavior in a two-dimensional code worked well in the 60° Titanium impact case (Case 5). However, in this case, only 9% (compared to 10.8% experimentally) of the projectile momentum was transferred to the intact target. Also, projectile *yaw* was not a significant factor in this thin target (1/8") case. Figure 6 shows the projectile-target velocity field at 32 μ sec, and the development of translation and yaw for the 60° Titanium Case 5 solution. The development and influence of projectile yaw is discussed in Section 4.4. Cases 6 and 7, the two 45° Aluminum plate cases, were chosen as severe tests of the semi-elliptical approximation method.

Cases 6 and 7 revealed an important aspect of oblique penetration dynamics; i.e., the development and significance of projectile *yaw*. Figure 7 shows the experimental and numerical predictions for the 45° obliquity impacts into 1/2" Aluminum plates. The differences in Figure 7 between the calculations and the experiments corresponding to Cases 6 and 7 are due, we believe, to projectile yaw. The nature of the computational-experimental discrepancy can be broken up into two parts. 1) In the *experiment*, the projectiles have an initial yaw which could significantly influence the subsequent projectile target dynamics. In the numerical calculations, the ideal 0° yaw configuration is modeled. 2) In the *numerical* calculation, yaw of the projectile is not treated during the penetration process. However, the experiment and post analysis of the numerical calculations demonstrate that significant yaw will develop while the projectile penetrates the 1/2" Al plate. This is true even if there is zero yaw initially. The capability of treating projectile yaw can and should be added to the semi-elliptical method.

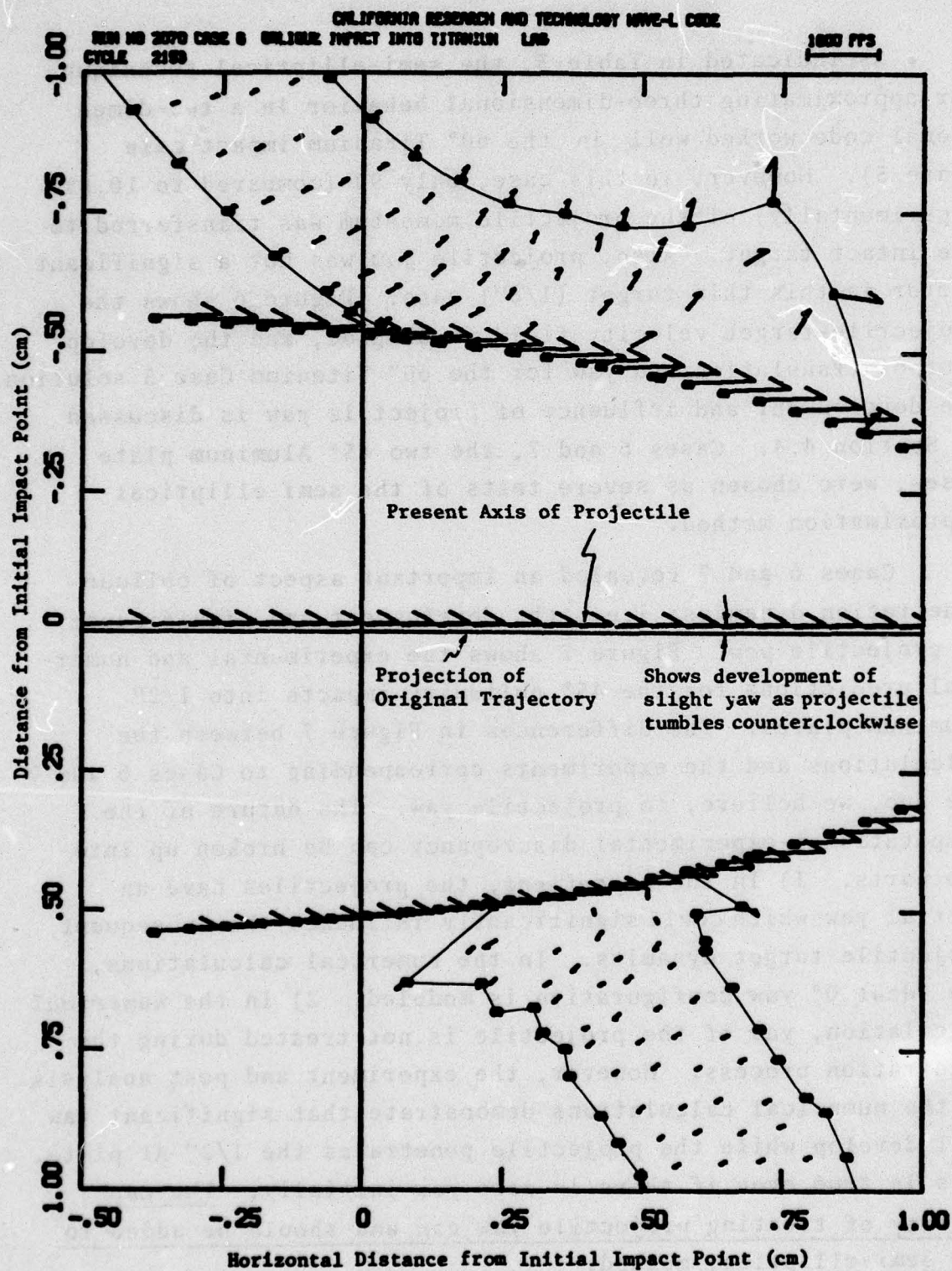


Figure 6. Velocity Field at 32.5 μ sec of a 1600 fps 60° Obliquity .50-Cal. Projectile Impact into 1/8-in. Titanium Blade (Case 5).

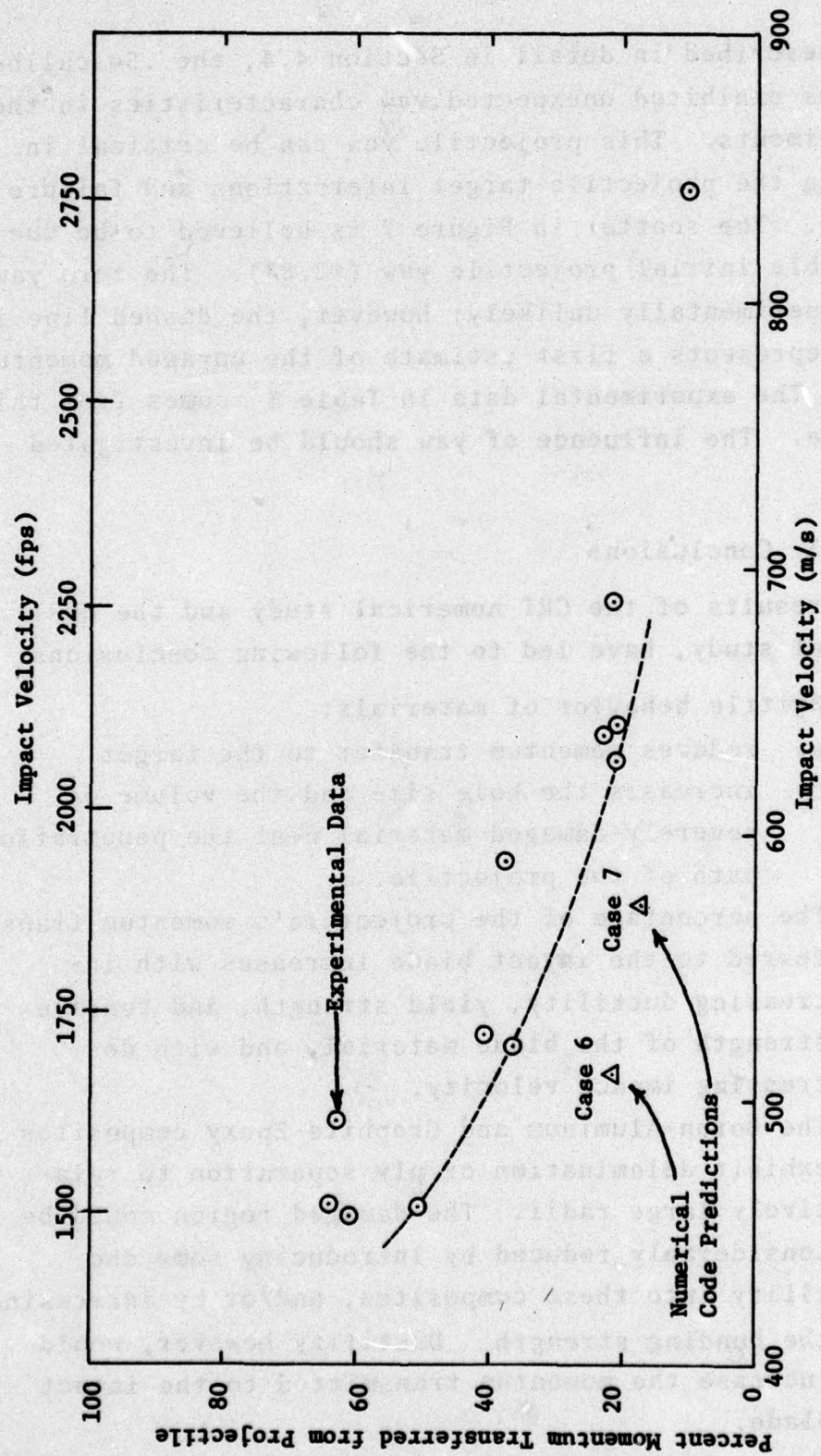


Figure 7. Percent Momentum Transferred from the Projectile as a Function of Impact Velocity for 45° Impacts on 1/2" Aluminum Plates.

As described in detail in Section 4.4, the .50-caliber projectiles exhibited unexpected yaw characteristics in the UDRI experiments. This projectile yaw can be critical in determining the projectile-target interactions and failure mechanisms. The scatter in Figure 7 is believed to be due to a variable initial projectile yaw ($\pm 2.8^\circ$). The zero yaw case is experimentally unlikely; however, the dashed line in Figure 7 represents a first estimate of the unyawed momentum transfer. The experimental data in Table 3 comes from this dashed line. The influence of yaw should be investigated further.

1.3.3 Conclusions

The results of the CRT numerical study and the UDRI experimental study, have led to the following conclusions:

1. Brittle behavior of materials:
 - a. reduces momentum transfer to the target
 - b. increases the hole size and the volume of severely-damaged material near the penetration path of the projectile.
2. The percentage of the projectile's momentum transferred to the intact blade increases with increasing ductility, yield strength, and tensile strength of the blade material, and with decreasing impact velocity.
3. The Boron-Aluminum and Graphite-Epoxy composites exhibit delamination or ply separation to relatively large radii. The damaged region could be considerably reduced by introducing some ductility into these composites, and/or by increasing the bonding strength. Ductility however, would increase the momentum transmitted to the intact blade.

4. Yaw, or the angle between the relative velocity vector and the projectile axis, appears important in determining the projectile-target interaction and damage mechanisms. Such yaw is usually present at impact, and it develops further due to asymmetric loading during the penetration process. Projectile yaw increases the momentum transfer to the target.
5. For *normal impacts on composite targets*, the major uncertainty in numerical calculations is the specification of important dynamic material properties such as ductility, and yield and failure surfaces.
6. The semi-elliptical 2-D method for simulating three-dimensional oblique impacts can be valuable both quantitatively and qualitatively. For large obliquities, the quantitative predictive ability of this method can be improved by adding the capability for treating yaw of the projectile as it penetrates through the target. The semi-elliptic method is still approximate, but it is far better than the plane strain approximation since the plane strain approximation ignores 3-D stress contributions from the radial motions of target material.

SECTION II

NUMERICAL METHOD

The basic numerical code used in this study is WAVE-L. This is a two-dimensional Lagrangian finite-difference method based on Wilkin's¹ hydrodynamic-elastic-plastic HEMP formulation.

WAVE-L has been previously employed for analyses of projectile penetrations into armor targets^{2,3} and into earth media^{4,5}. Generic documentation for the code appears in References 1 and 6.

For the normal-incidence impact solutions, the usual axisymmetric version of WAVE-L is employed. A modified version of the code, using a semi-elliptical coordinate method, has been developed to simulate oblique-incidence impacts. This new technique is described in Section 4.

2.1 Initial Geometric Conditions

Figures 8 and 9 show the details of the .50-caliber core projectile and the initial computational grid used to define normal-incidence projectile impact problems. The .50-caliber projectile is treated as a rigid body; its periphery is defined by a series of closely-spaced points. The target blade is divided into a net of Lagrangian computational cells. The net distorts to accommodate material deformation. The computational cells extend to a radius of 3" to match the UDRI experimental configuration.

2.2 Material Properties

As stated above, the steel projectile is considered to be a rigid body in the calculations. This assumption is reasonable, in that only minor distortions of the projectile are expected during impact and penetration of the Titanium, composite, and Aluminum blade materials in this study.

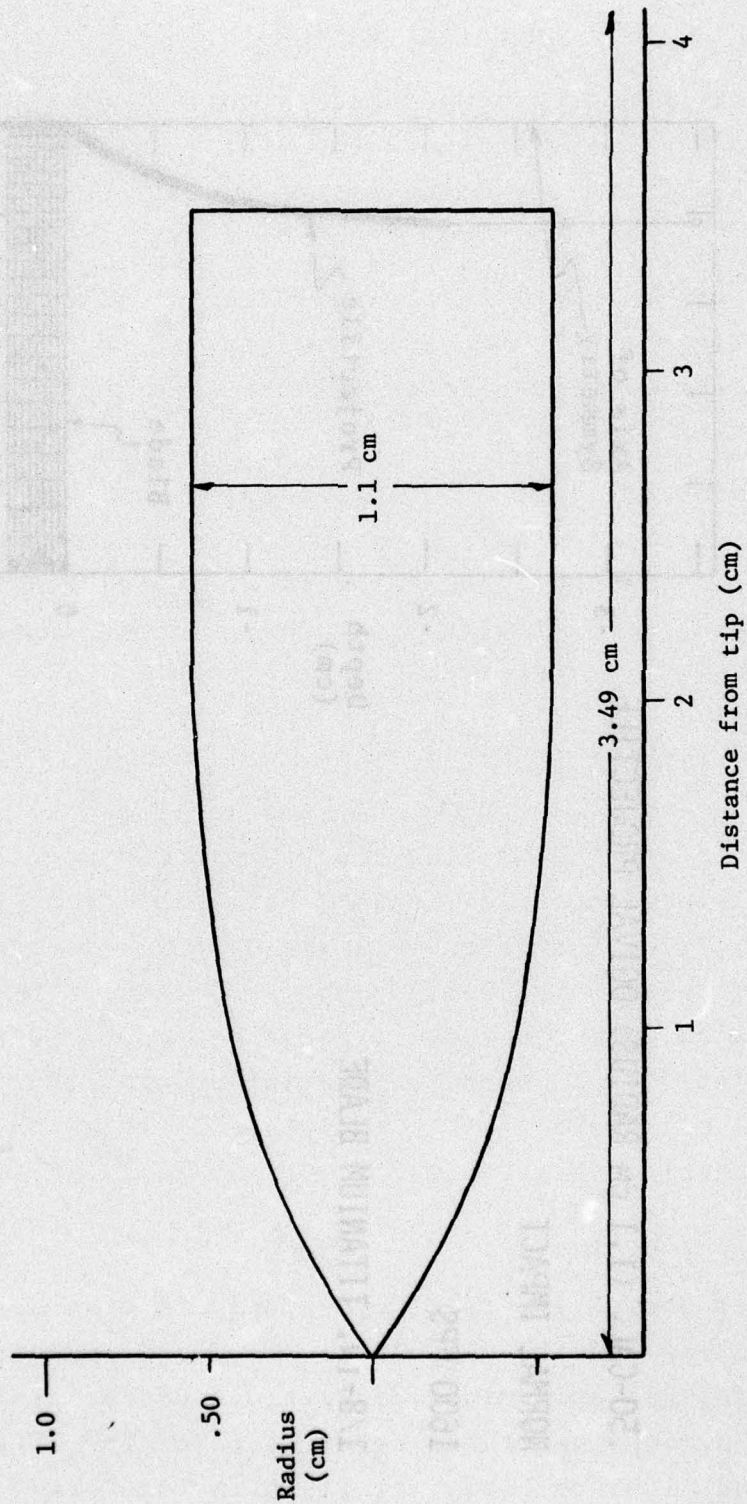


Figure 8. Projectile Shape is the Core of a .50-Caliber Armor-Piercing Bullet.

ILLUSTRATION OF NUMERICAL SOLUTION AND EXPERIMENTAL CORRELATION

.50-CAL. (1.1 CM RADIUS) OGIVAL PROJECTILE

NORMAL IMPACT

1600 FPS

1/8-IN. TITANIUM BLADE

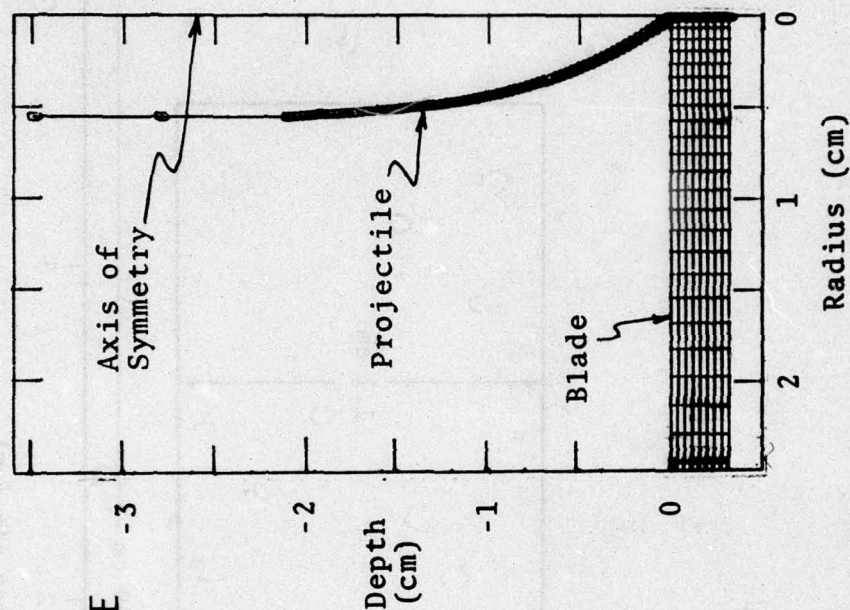


Figure 9. Initial Projectile and Computational Configuration for the 1/8-in. Normal Impact Cases.

The important properties used to model the Titanium alloy (Ti-6Al-4V), the Boron-Aluminum and Graphite-Epoxy composites, and Aluminum blade materials are summarized in Table 4.

Titanium was modeled as a hydrodynamic-elastic-plastic material with a yield value of 165 ksi in both tension and compression. A detailed description of the material model is in Appendix A. Failure in tension (leading to the explicit cracking described in Section 2.3) can only occur after the strain (ductility) reaches 10%. This simple model agrees well with experimental stress-strain curves for 6Al-4V Titanium alloy^{7,8}.

Both Boron-Aluminum and Graphite-Epoxy are considered brittle in tension, i.e., elastic to a brittle failure surface. No experimental data were found describing failure of these materials under compressive loads, so they were treated as elastic-perfectly plastic under compression. The failure surface is characterized by a von Mises criterion.

Test data^{9,10} show that the elastic properties and tensile failure properties of Boron-Aluminum and of Graphite-Epoxy are functions of the angle-ply orientation of the fibers (Figures 10, 11, and 12). The preferential orientations of fibers in turbine blades imply that even normal-incidence impacts on these composites will be three-dimensional in nature. Thus a bullet impact and penetration will lead to somewhat different material behavior in the direction *along* the blade, *across* the blade, and *through* the blade. Since the numerical method is two-dimensional (axisymmetric), the three-dimensional nature of the composite blade materials must be approximated. For the present study, this was done by averaging the elastic properties measured in all directions (i.e. ply orientation from $\theta=0$ to $\theta=90^\circ$ in Figures 10 to 12),

TABLE 4. ELASTIC-PLASTIC PROPERTIES OF BLADE MATERIALS USED IN NUMERICAL SOLUTIONS

	Titanium	Boron-Aluminum	Graphite-Epoxy	Aluminum
Density, ρ_0 , gm/cm ³	4.51	2.4	1.25	2.7
Young's Modulus, E, 10 ⁶ psi	16.3	20.0	5.3	10.7
Shear Modulus, G, 10 ⁶ psi	6.2	7.6	2.0	4.0
Bulk Modulus, K, 10 ⁶ psi	14.9	17.6	4.4	11.5
Poisson's Ratio, ν	0.32	0.31	0.30	0.34
Elastic Limit, Y, ksi	165	53	42	42 (work hardening)
Yielding and Failure:				
Compression	H-E-PP*	H-E-PP	H-E-PP	H-E-P (work hardening)
Tension	fails at 145,000 psi if generalized plastic strain exceeds 10%	Perfectly Brittle: fails at 53 ksi in plane (σ_{rr} or $\sigma_{\theta\theta}$), or at 20 ksi normal to blade (σ_{zz})	Perfectly Brittle: fails at 42 ksi in plane (σ_{rr} or $\sigma_{\theta\theta}$), or at 20 ksi normal to blade (σ_{zz})	Fails at 62 ksi if generalized plastic strain exceeds 11%

* hydrodynamic elastic-perfectly plastic

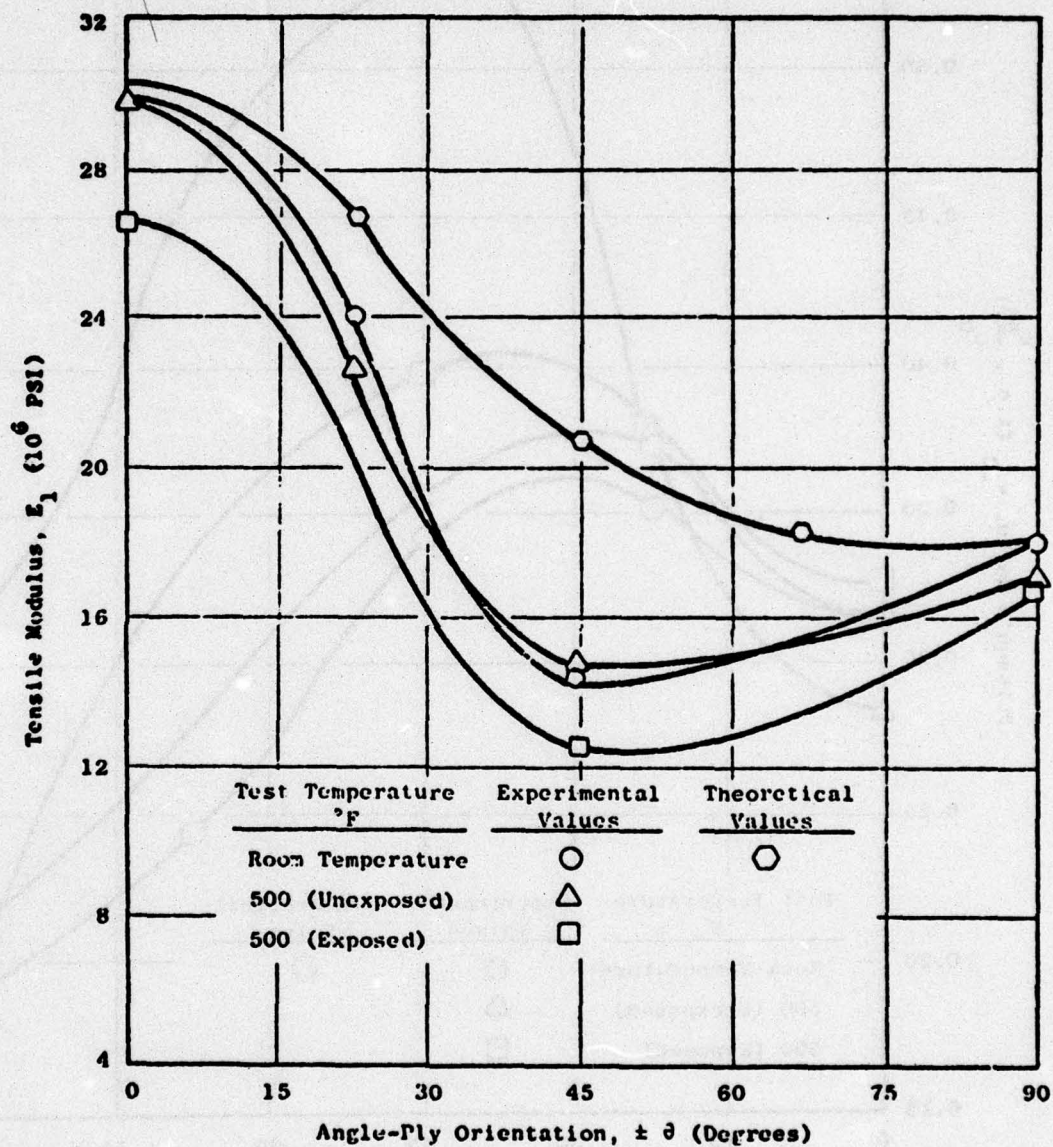


*Figure 10. Tensile Modulus Vs Ply Orientation for Angle-Plyed Al/B Composites

*Taken from Reference 9.

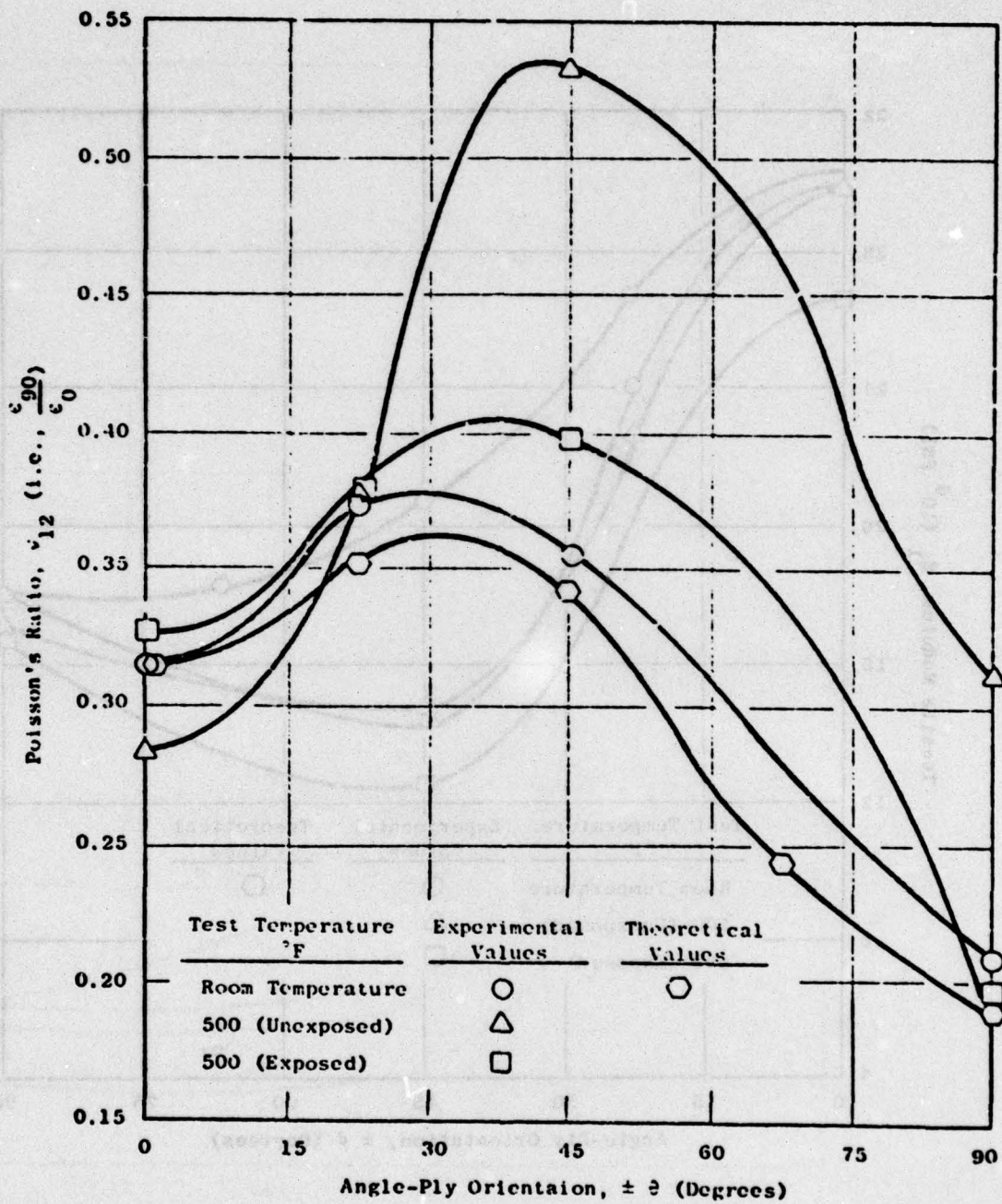


*Figure 11. Poisson's Ratio Vs Ply Orientation for Angle-Plyed Al/B Composites

*Taken from Reference 9

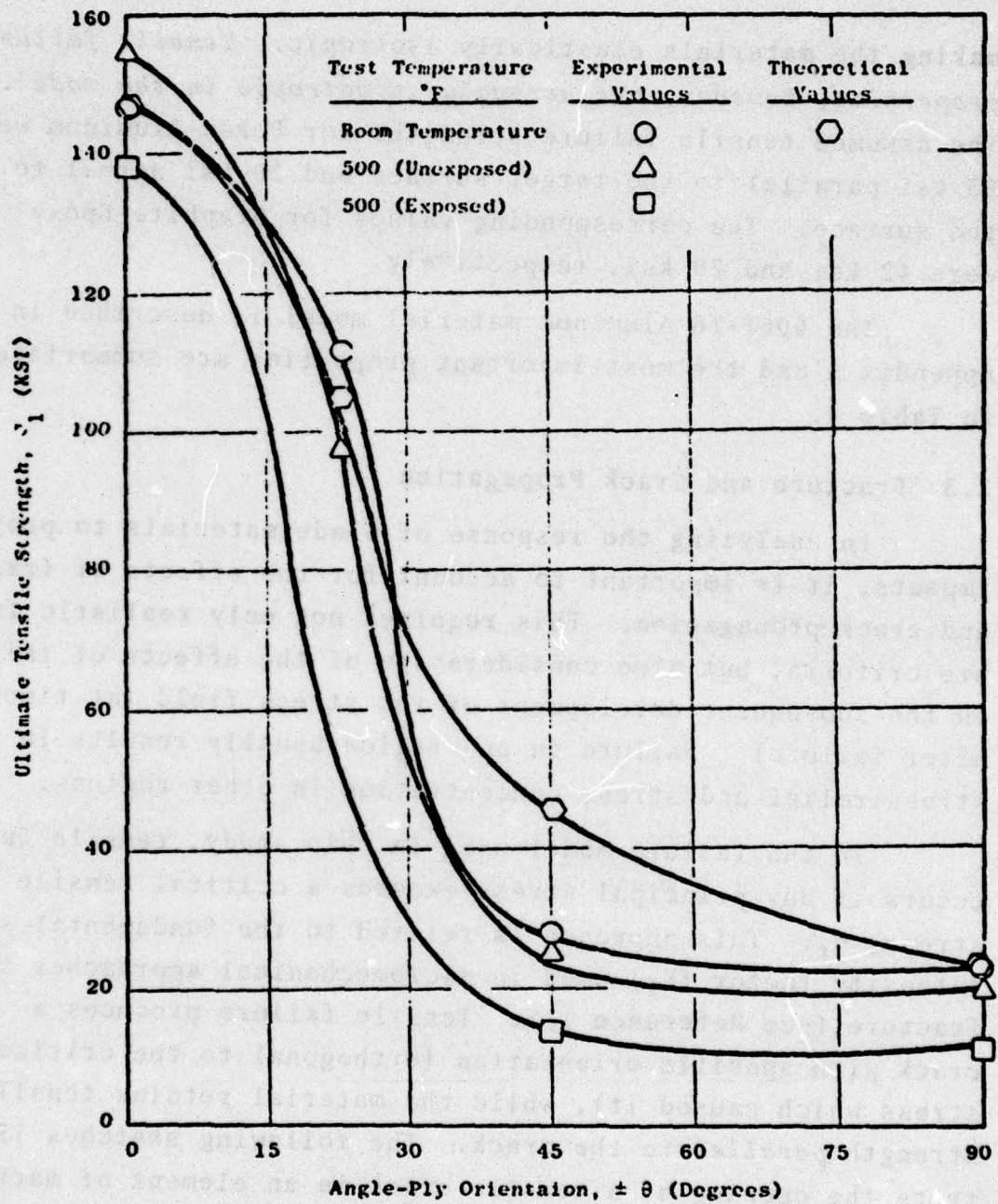


*Figure 12. Ultimate Tensile Strength Vs Ply Orientation for Angle-Plyed Al/B Composites

*Taken from Reference 9

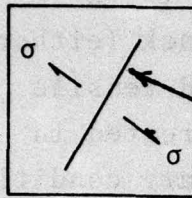
making the materials elastically isotropic. *Tensile failure properties, however, are strongly anisotropic in the model.* The assumed tensile failure strengths for Boron-Aluminum were 53 ksi parallel to the target surface and 20 ksi normal to the surface. The corresponding values for Graphite-Epoxy were 42 ksi and 20 ksi, respectively.

The 6061-T6 Aluminum material model is described in Appendix A and the most important properties are summarized in Table 4.

2.3 Fracture and Crack Propagation

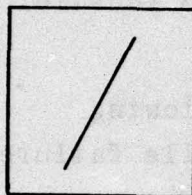
In analyzing the response of blade materials to projectile impacts, it is important to account for the effects of fracture and crack propagation. This requires not only realistic failure criteria, but also consideration of the effects of failure on the subsequent development of the stress field (at times after failure). Failure in one region usually results in both stress relief and stress concentration in other regions.

In the failure model used in this study, tensile failure occurs if any principal stress exceeds a critical tensile stress, σ_t . This approach is related to the fundamental stress intensity factor (K_I) used in micromechanical approaches to fracture (see Reference 11). Tensile failure produces a crack with specific orientation (orthogonal to the critical stress which caused it), while the material retains tensile strength *parallel* to the crack. The following sketches illustrate the opening of a tensile crack in an element of material and the subsequent tensile properties of that element:

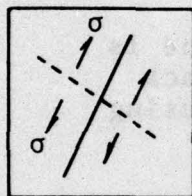


Tensile stresses (σ) exceed the critical tensile failure value (σ_t) in the indicated principal stress direction

Plane which experiences tensile stress $\sigma > \sigma_t$.



Crack opens and relieves the tensile stress such that no forces or tractions exist on the crack surfaces; i.e., zero normal and shear stress on the crack surface.



In the directions perpendicular to the crack surface, the material can maintain tensile stresses up to σ_t , the critical tensile failure value.

WAVE-L treats the following aspects of a single tensile fracture in a computational cell:

- o The orientation of a tensile crack is determined.
- o The crack width is computed. Stress relief occurs on the open crack's free surfaces; i.e., no normal or shear stresses are allowed across the crack free surfaces as long as it remains open.
- o If a crack closes, its subsequent tensile strength (perpendicular to the crack) is zero.
- o The tensile strength of the material is unaffected in directions parallel to the crack (this is true if the crack is open or closed).

Subsequently, if the tensile failure criterion is exceeded in a direction perpendicular to the first crack (either in the r-z plane or in the hoop direction), a second tensile crack can develop. The presence of two cracks is treated in an analogous fashion, except that the stress boundary conditions must be satisfied on each crack. If a third crack develops, then the cell is considered to be pulverized, and no tensile stresses are permitted in any direction.

As an aid in interpreting field plots, the following plotting conventions are used to indicate that tensile failure has occurred in a Lagrangian cell:



Single crack in r-z plane. The line is plotted in the direction of the crack (normal to the principle stress causing the crack.)



Hoop crack; i.e., $\sigma_{\theta\theta} > \sigma_t$ caused the crack.



Hoop and r-z plane cracks.



Two r-z plane cracks; only hoop tension is permitted.



Completely fractured - no tension permitted.



Generalized plastic strain exceeds input value (currently 10%).

SECTION III

NORMAL-INCIDENCE IMPACTS OF .50-CALIBER PROJECTILES

3.1 Titanium Blades

Starting with the initial geometric conditions in Figure 9, the normal impact of a .50-caliber projectile at 1600 fps into a 1/8-in. Titanium plate was analyzed. Figure 13 shows the projectile and plate 4 μ sec after the impact. At this time, the projectile nose has penetrated about 2/3 through the plate. Distortion of the plate is represented by the configuration of the Lagrangian grid in the left view in Figure 13. Local velocities of Titanium are seen in the velocity field in the right view in Figure 13. Material near the initial impact point has flowed outward and upward along the advancing projectile surface. Titanium on or near the nose tip is being driven downward and outward.

Figure 14 shows the Lagrangian grid and the velocity field 11 μ sec after impact. The nose has fully penetrated the plate. (Grossly distended cells ahead of the nose represent low-density shattered debris.) A layer of Titanium about 0.5-mm thick next to the projectile surface is severely distorted. A lesser degree of distortion extends several mm out into the plate. In the velocity field, debris from the front surface is moving up and out; the rest of the plate has a downward component.

The plate distortion after 30 μ sec is seen in Figure 15. Shattered debris moves along the projectile surface both ahead and behind the plate. The plate is appreciably depressed downward by the projectile, and tensile cracking appears around the hole.

Figure 2 is the final plot from this solution, at a time of 52 μ sec after the impact. The projectile nose is

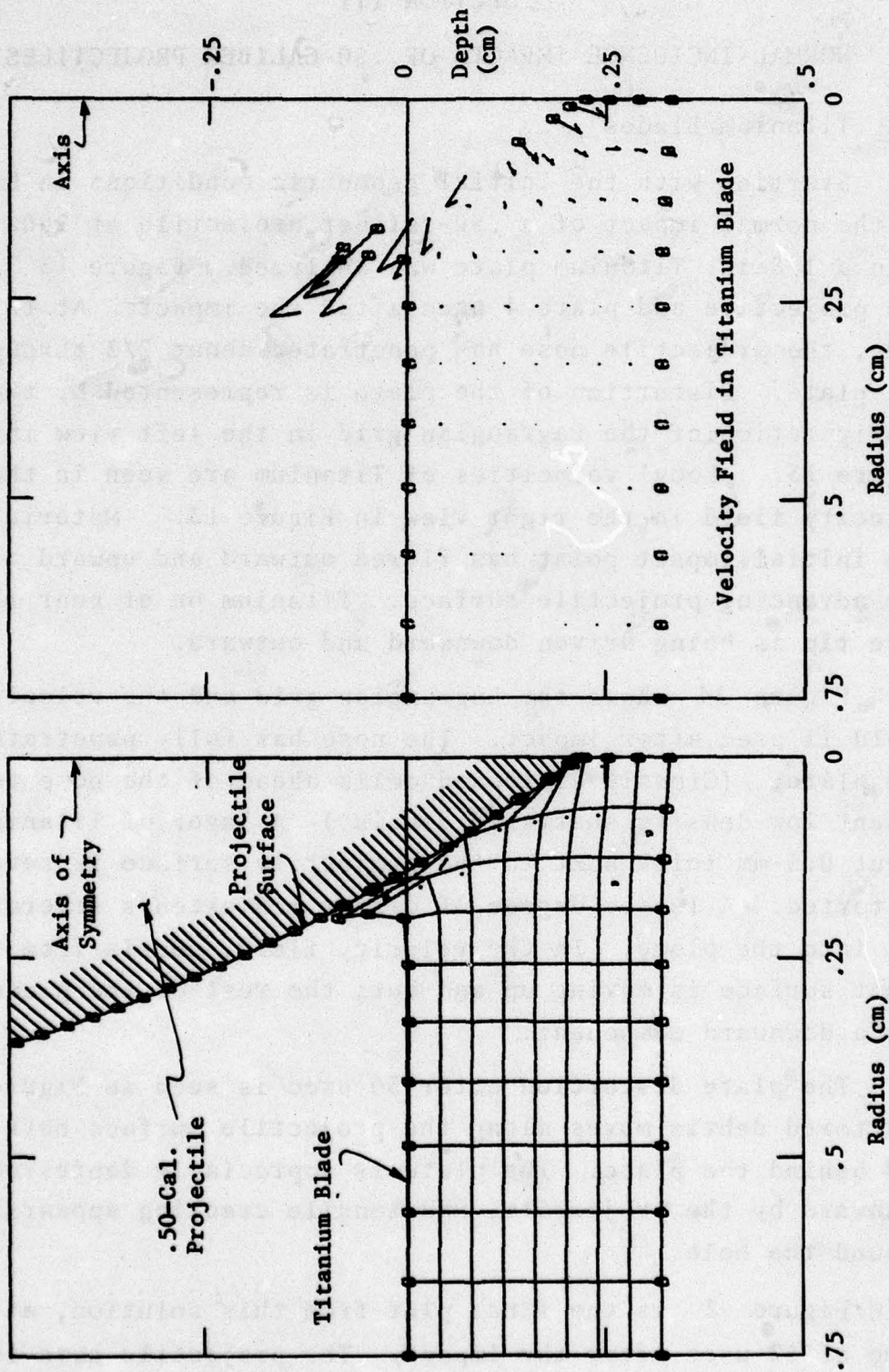


Figure 13. .50-Cal. Projectile Impact at 1600 fps into 1/8-in. Titanium Blade. Local Blade Distortion and Local Velocities at 4 μ sec.

CALIFORNIA RESEARCH AND TECHNOLOGY WAVE-L CODE
 RUN NO 8070-CR22 4 RIGID BODY PENETRATION IN TO TITANIUM
 CYCLE 784

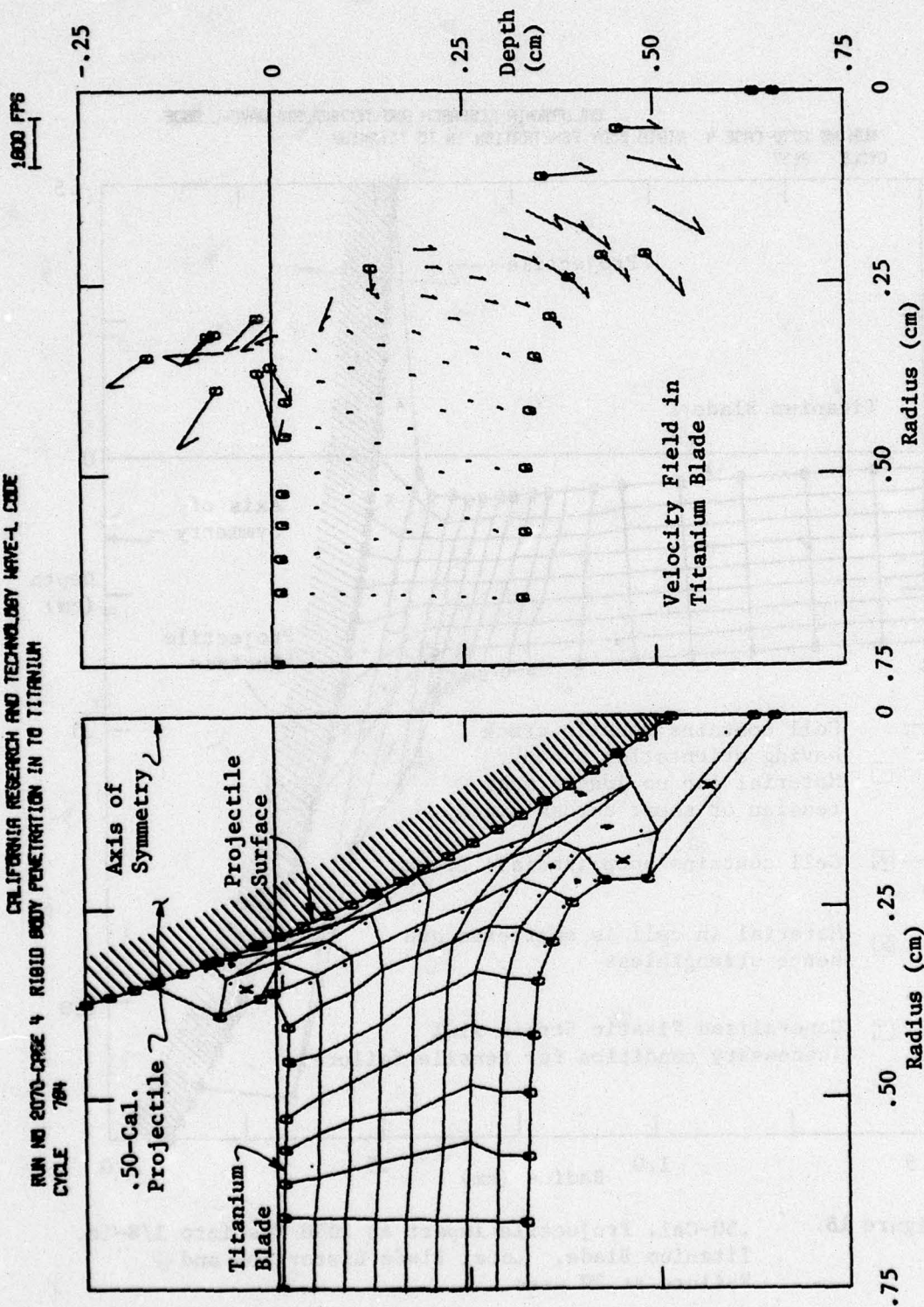


Figure 14. .50-Cal. Projectile Impact at 1600 fps into 1/8-in. Titanium Blade. Local Blade Distortion and Local Velocities at 11 μ sec.

CALIFORNIA RESEARCH AND TECHNOLOGY WAVE-L CODE
 RUN NO 2070-CASE 4 RIGID BODY PENETRATION INTO TITANIUM
 CYCLE 2137

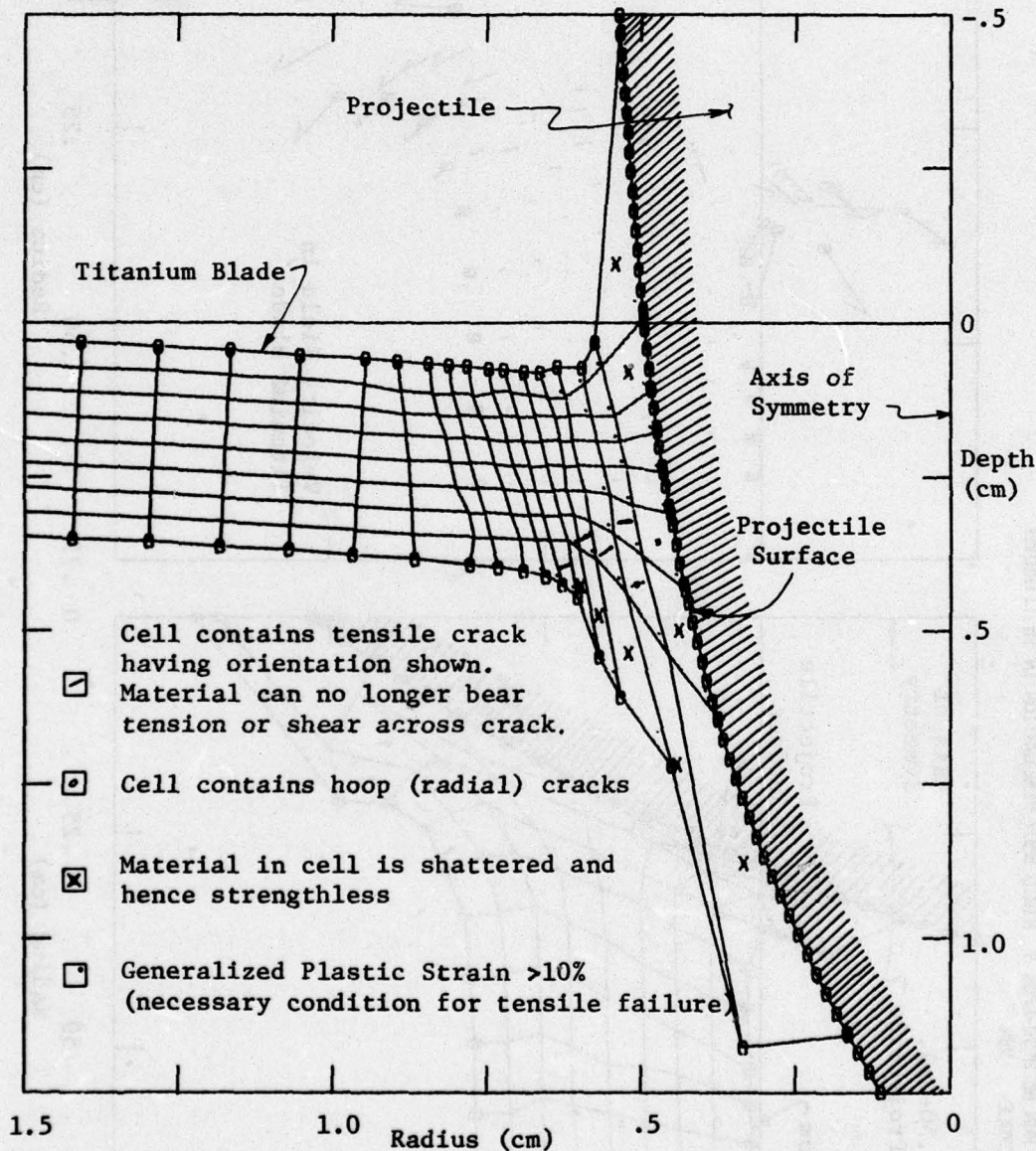


Figure 15. .50-Cal. Projectile Impact at 1600 fps into 1/8-in. Titanium Blade. Local Blade Distortion and Failure at 30 μ sec.

completely through the Titanium plate, and no further damage or momentum transfer is occurring. The analysis was therefore terminated at this point. An extensive region of shattered material is emerging from the rear of the plate. A much smaller mass of debris is ejected from the front surface. The heavy line in Figure 2 delineates severely damaged or cracked Titanium which will be removed to leave an open hole. The surface of the plate near the projectile has been pushed down about 1.5 mm. Some elastic rebound will occur, but some of this deflection is due to plastic distortion of the Titanium.

A summary of the most important quantitative predictions of this calculation follows:

- o Total axial momentum lost by projectile = 10%
- o Total mass removed from target = 1.22 gms
- o Axial momentum transferred to intact target = 8.2%
- o Axial momentum transferred to target fragments = 1.8%

3.1.1 Zoning Test

Since the cost of numerical solutions is quite sensitive to the computational cell size (or numerical resolution), it is desirable to use the coarsest resolution which will provide acceptable accuracy. In order to determine if coarser resolution could be employed for bullet-blade impact problems, a partial solution was performed in which larger cells were used. Figure 16 shows a comparison of the initial grid for this coarser zoning with the finer zoning described in the previous section. Figure 17 compares the Titanium plate distortions and the boundary of fractured material after approximately 30 μ sec. The solutions are seen to be quite similar. (The differences in the shattered region are due to deletions of grossly-distorted cells. This region has no effect on continuing damage or impulse.)

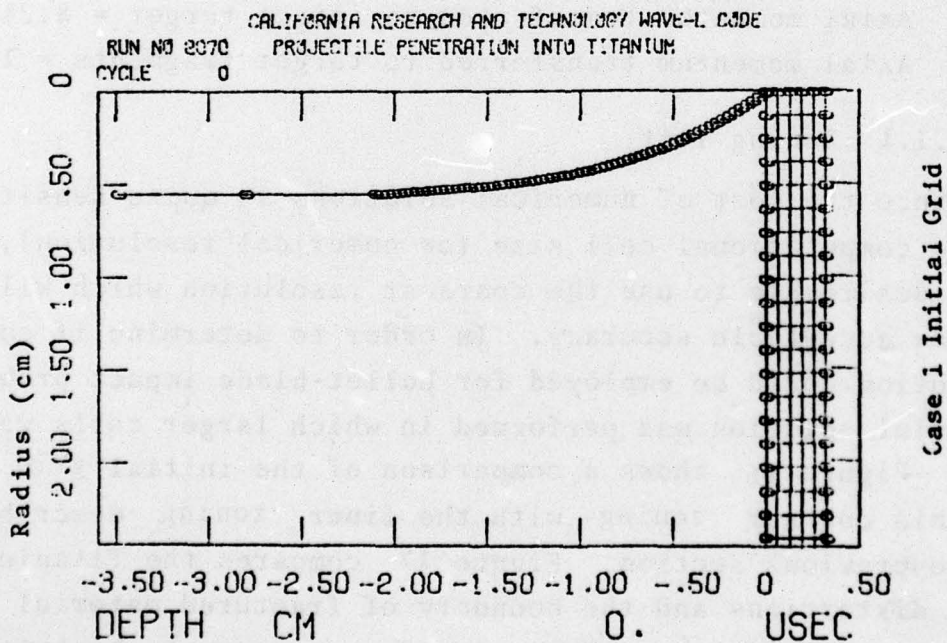
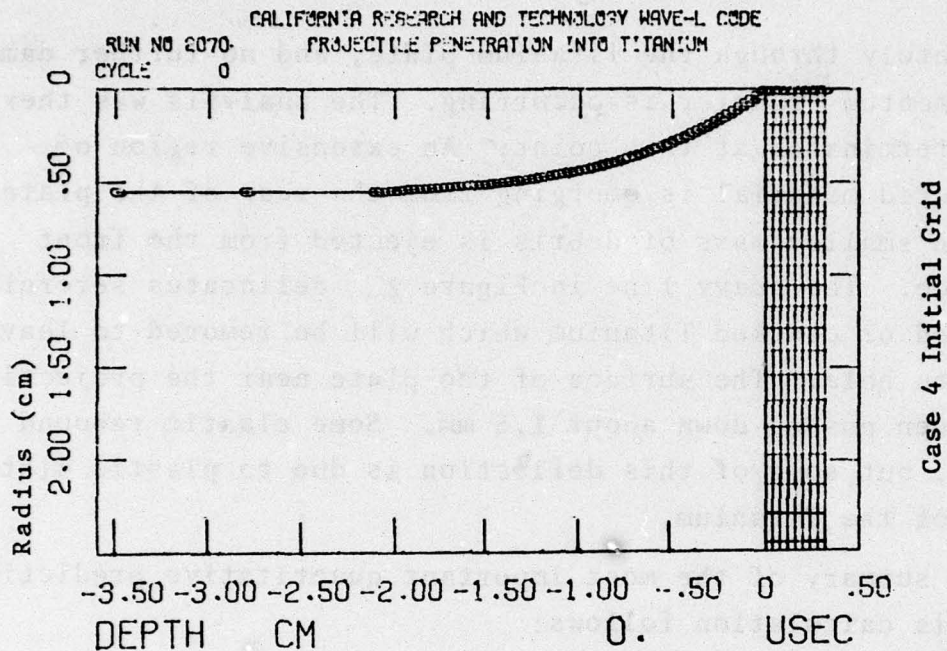


Figure 16. Comparison of Coarsely-Zoned (Case 1) and Finely-Zoned (Case 4) Initial Grid Configurations for the Penetration of a 1/8" Ti Plate by a 50-Caliber Core

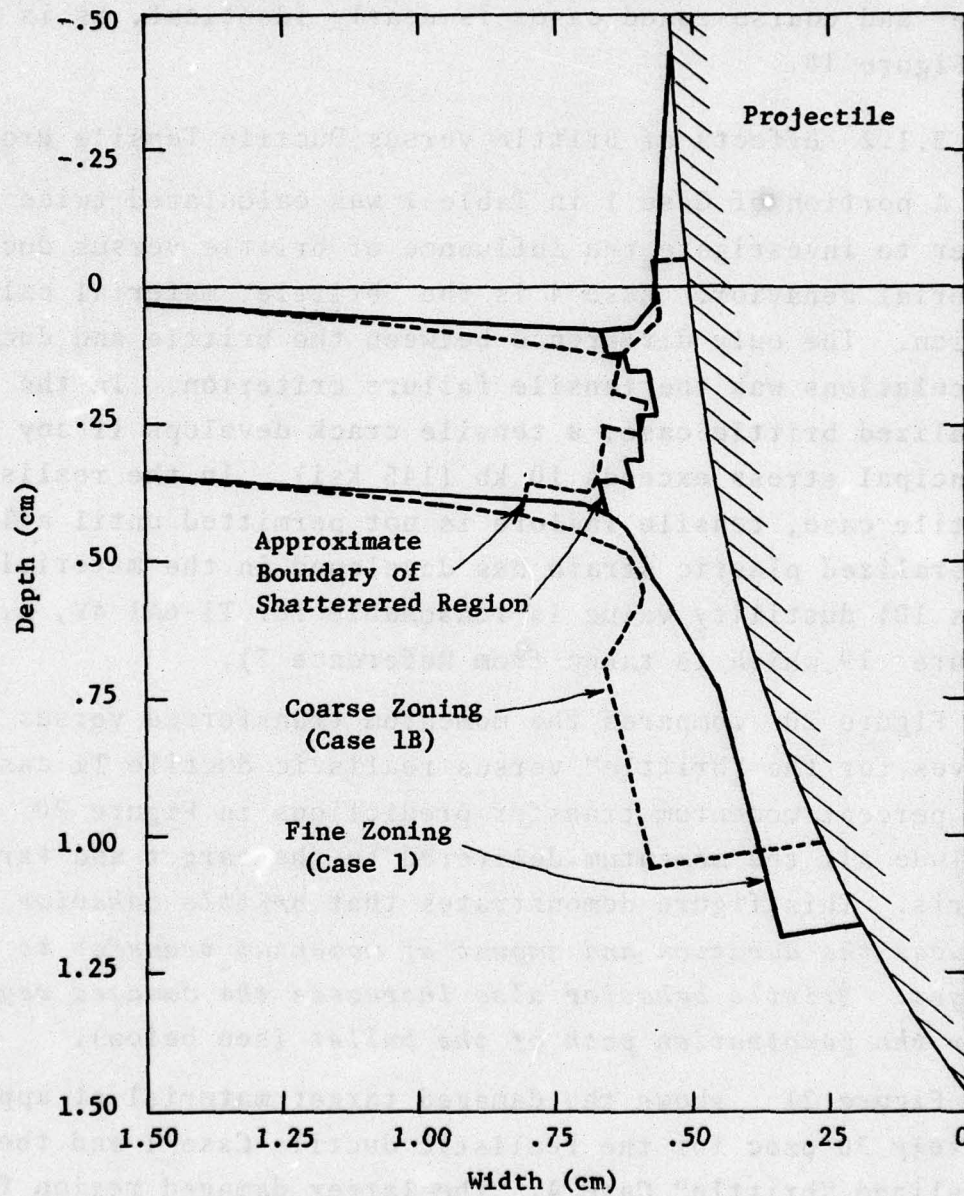


Figure 17. Zoning Comparison for Normal Impact Calculation of .50-Caliber Projectile on a 1/8" Titanium Plate.

The momentum transfer to the Titanium plate in the fine- and coarse-zoned cases is nearly identical, as is seen in Figure 18.

3.1.2 Effects of Brittle versus Ductile Tensile Properties

A portion of Case 1 in Table 1 was calculated twice in order to investigate the influence of brittle versus ductile material behavior. Case 4 is the "brittle" material calculation. The only difference between the brittle and ductile calculations was the tensile failure criterion. In the idealized brittle case, a tensile crack develops if any principal stress exceeds 10 kb (145 ksi). In the realistic ductile case, tensile failure is not permitted until a 10% generalized plastic strain has developed in the material. This 10% ductility value is reasonable for Ti-6Al-4V, e.g. see Figure 19 which is taken from Reference 7).

Figure 20 compares the momentum transferred versus time curves for the "brittle" versus realistic ductile Ti cases. The percent momentum transfer predictions in Figure 20 include all the momentum delivered to the target and target debris. This figure demonstrates that *brittle behavior reduces the duration and amount of momentum transfer to a target. Brittle behavior also increases the damaged region near the penetration path of the bullet* (see below).

Figure 21 shows the damaged target material at approximately 30 μ sec for the realistic ductile Case 1 and the idealized "brittle" Case 4. The larger damaged region for the brittle case is evident in this figure. Also, note that the effect of the increased damage is to allow earlier *decoupling* between the target and penetrating projectile. Thus, the forces acting between the projectile and target are reduced with the brittle behavior of the Ti as compared to the realistic ductile behavior.

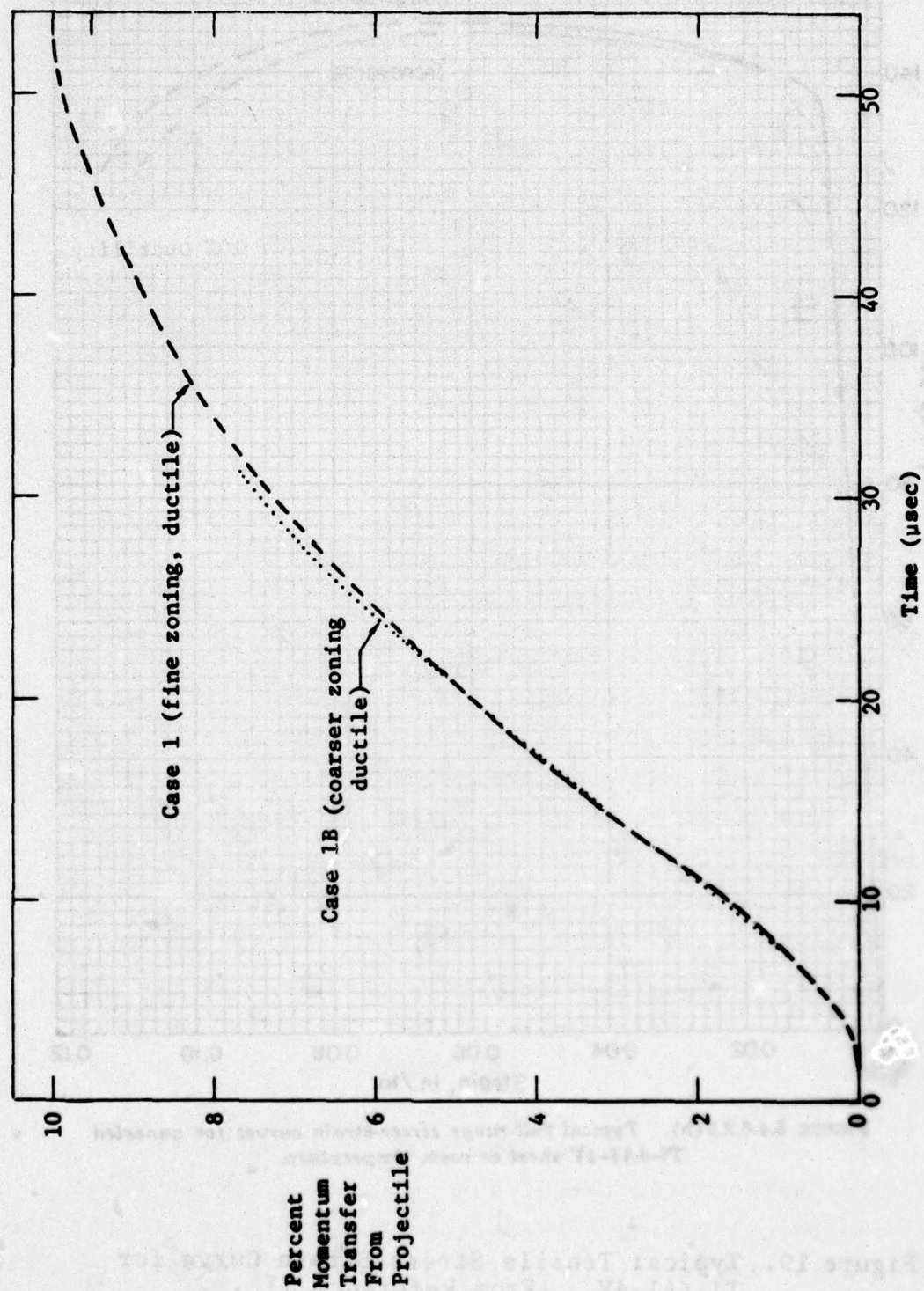


Figure 18. Percent Momentum Transfer versus Time for the .50-Caliber Core Normal Impacts on Ti Plates Using Fine and Coarser Zoning.

BEST AVAILABLE COPY

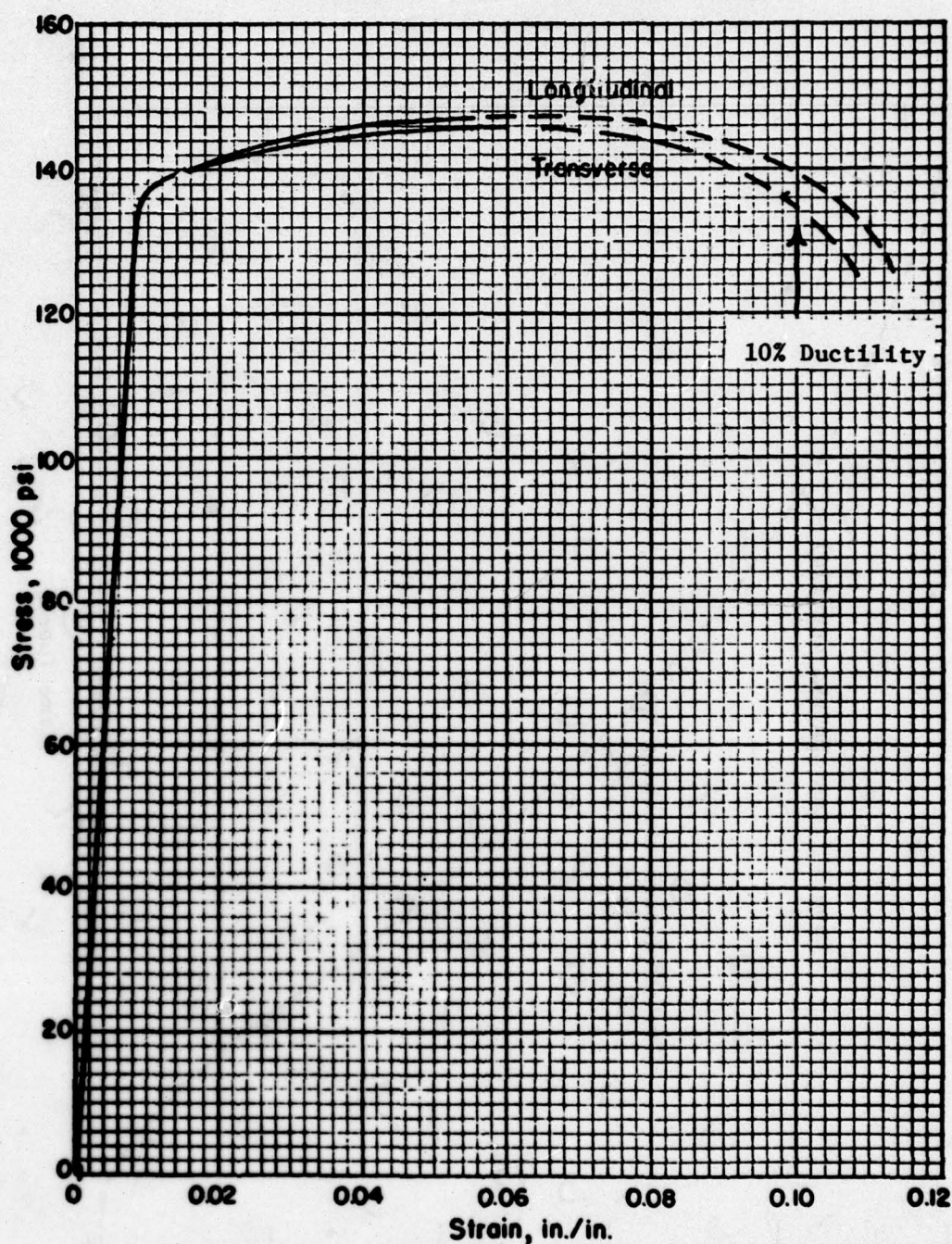


FIGURE 5.4.6.2.6(b). Typical full-range stress-strain curves for annealed Ti-6Al-4V sheet at room temperature.

Figure 19. Typical Tensile Stress-Strain Curve for Ti-6Al-4V. (From Reference 7)

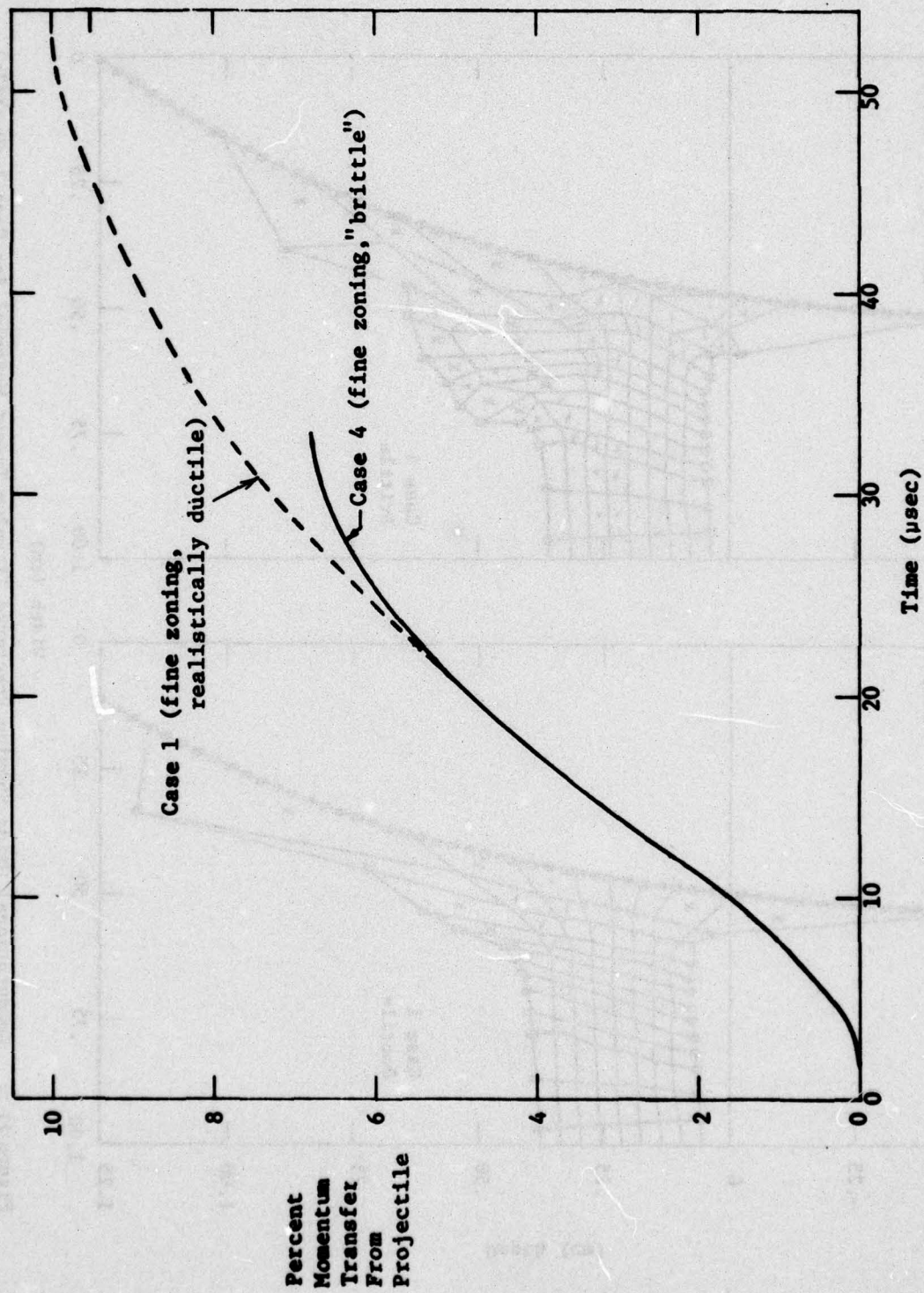


Figure 20. Percent Momentum Transfer versus Time for the .50-Caliber Core Normal Impacts on Realistic and Ideally Brittle T_i Plates.

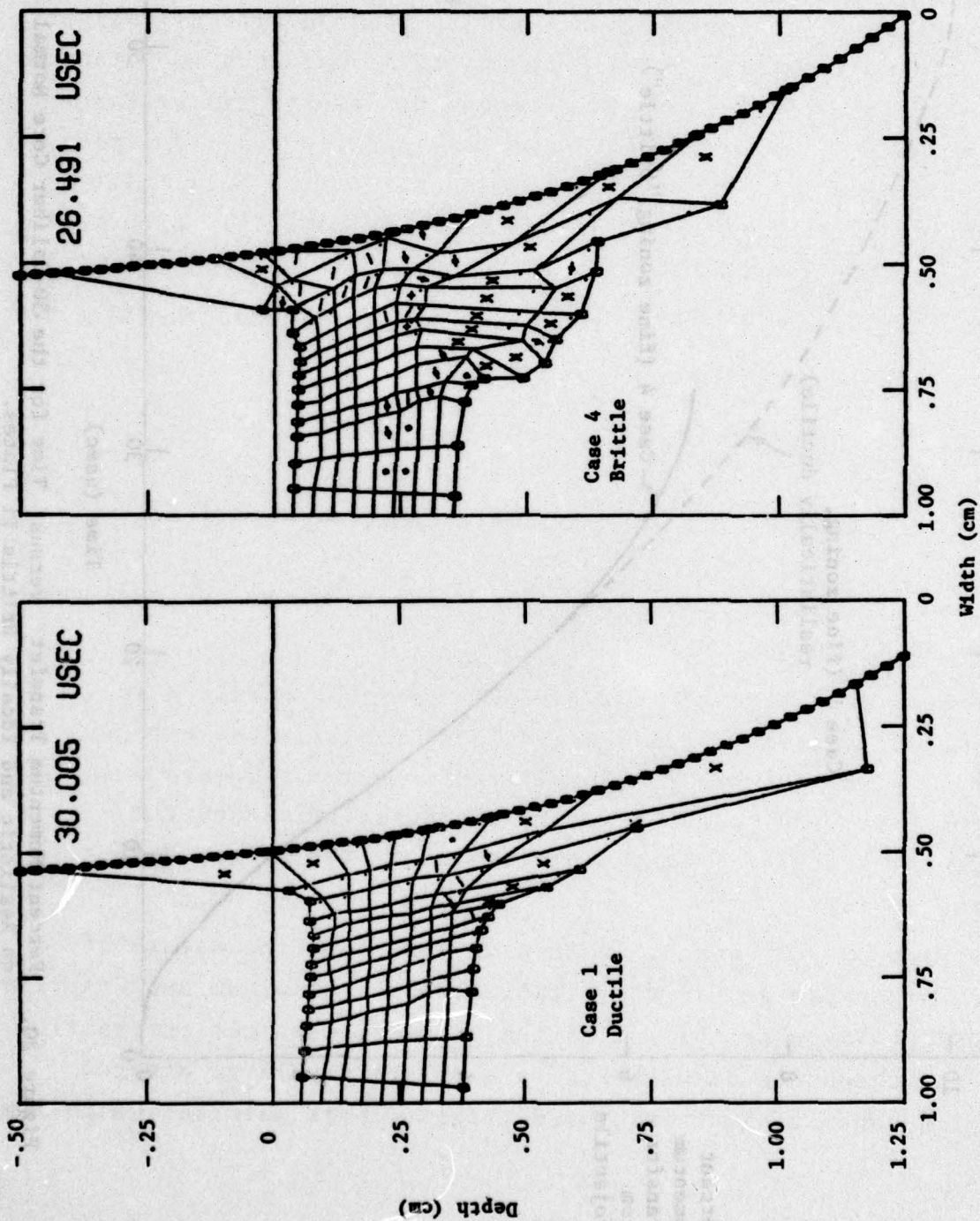


Figure 21. Computational Grids Showing Fractured Titanium Target Material for Case 1 (Ductile) and Case 4 (Brittle).

3.2 Boron-Aluminum and Graphite-Epoxy Composite Blades and Quantitative Comparisons with Titanium Blades

The eventual widespread use of composite turbine blades depends on 1) cost savings related to reduced aircraft weight, and 2) the composite blade performance as compared to Titanium blades. Therefore, in this section the results of the Boron-Aluminum and Graphite-Epoxy numerical solutions are described and compared to the Titanium solutions (Section 3.1). The most significant changes in the composite materials properties as compared to the Titanium properties involve

- o the factor of three reduction in yield strength (Y) and tensile strength (σ_t),
- o the lack of ductility, i.e. the composites are brittle, and
- o the decrease in material bulk density (ρ)

Table 4 summarizes these material properties for the composites and the Titanium.

The large changes in material properties resulted in important composite blade response characteristics which differ significantly from the Titanium blade response. In particular, the target fracture characteristics and the momentum transfer from the projectile to the target differ dramatically.

Figures 2,3, and 4, in Section 1.3, show the nature of the target damage for the Titanium, Boron-Aluminum and Graphite-Epoxy plates near the end of the projectile-target interaction. In the composite cases there is a relatively large damaged region consisting of fractured target debris material which has

essentially decoupled from the target by 30 μ sec. Also, note that some debonding of the ply layers occurs out to relatively large radii with the 20 ksi bonding strength assumed for both composite materials. Delamination of the blade material extends to about 2 cm radius for the Boron-Aluminum blade and to 1.2 cm radius for the Graphite-Epoxy blade.

Figure 1 compares the momentum transfer vs time curves for the normal impact cases on the Titanium, Boron-aluminum, and Graphite-Epoxy blades. The dramatic difference between the Titanium and composite blade response is due to the material property differences indicated in Table 4. The yield strength for the Titanium is roughly three times higher as compared to the composite materials. The separation of the momentum vs time curves in Figure 1 is initially due to the differences in yield strengths. However, at later times the perfectly brittle composite material model leads to an earlier decoupling of shattered target material from the remainder of the intact composite blades. Thus, the earlier decoupling also limits the duration and magnitude of momentum transfer between the projectile and intact target. In addition, some of the differences between the Boron-Aluminum and Graphite-Epoxy response is due to the difference in density. The higher the density, the greater the *inertial resistance* to penetration which reduces tensile strains which reduce tensile failure.

3.3 Experimental Comparisons for Normal Impacts

UDRI conducted two series of experiments intended to duplicate the impact conditions used in the numerical calculations. Their experimental procedures and results are reported in detail in their reports which are duplicated as Reference 14 and Appendix B. The conditions which they examined in the first series of experiments are described in Reference 14.

and are outlined below:

Impact velocity - nominal 1600 ft/sec = 448 m/sec
(Velocities varied from 323 m/sec to
517 m/sec)

Projectile - .50-caliber hardened steel ogive

Impact Obliquity - 90° and 60° (the 60° case is
described in Section 4.4)

Target Material - 1/8-in. thick Titanium
1/8-in. thick Boron-Aluminum
1/8-in. thick Graphite-Epoxy

Figure 22 shows comparisons of the experimental and numerical predictions of the percentage of initial projectile momentum which was transferred to the various targets as a function of initial projectile velocity. The agreement is satisfactory. The calculated values are shown as a range for the composites due to the inherent uncertainties in dynamic failure criteria in composites and the resulting uncertainty in the amount of momentum carried off in target debris. The target debris mass and momentum predicted by the WAVE-L code are treated as upper limits since real materials usually behave stronger under dynamic conditions, and static brittle properties were used in the calculation.

The calculated momentum transfer for the Titanium plate was 8.2% as compared to an experimental value of 7.6%. The experimental-numerical difference is less than 8%. Thus, normal impact calculations can agree very well with the experiments when physically realistic material models are used in the calculations. The primary uncertainty is with regard to the composite ductility and failure properties under dynamic conditions.

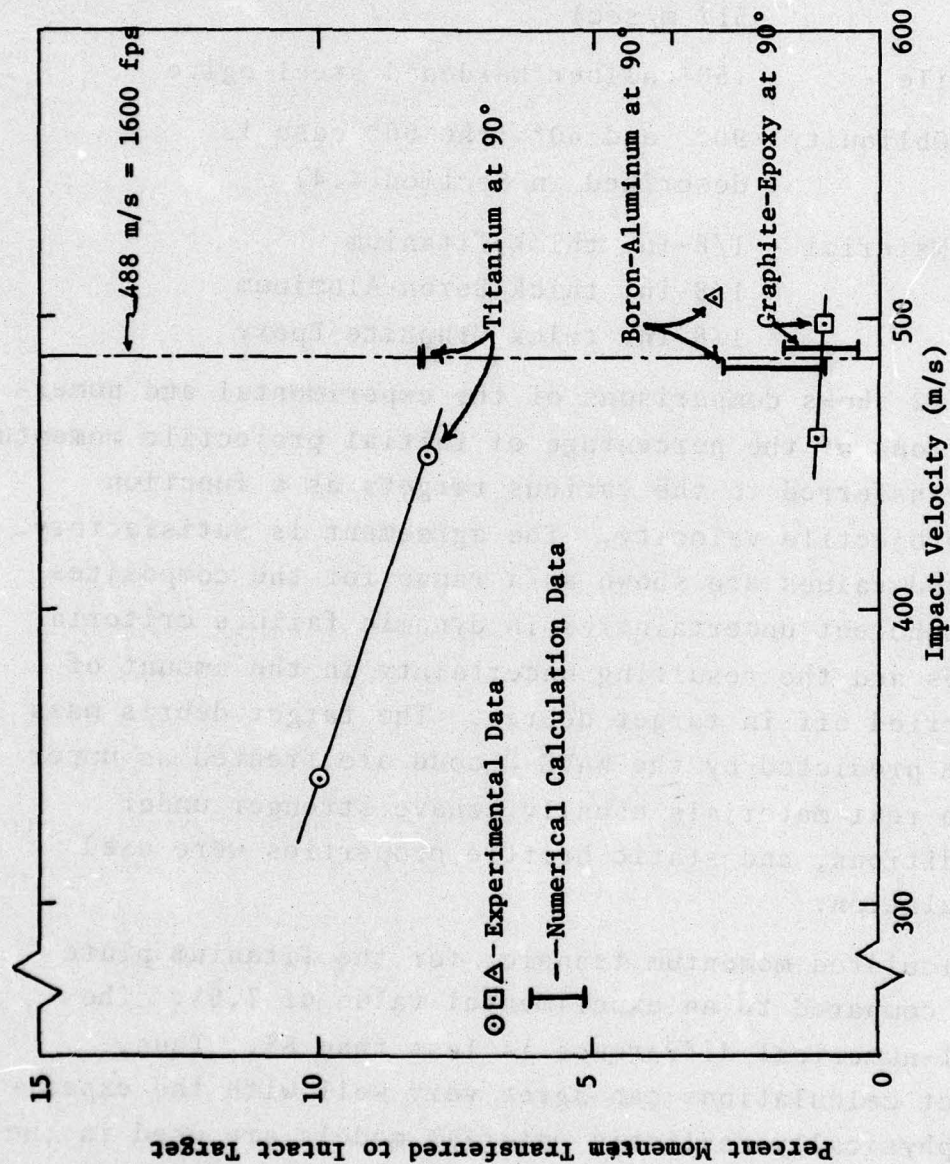


Figure 22. Comparison of Experimental Data and Numerical Calculation Predictions for Momentum Transferred in the Normal Impact Penetration of the T1, B/Al, and Graphite-Epoxy 1/8-in. Plates.

SECTION IV

OBLIQUE IMPACTS

Two-dimensional numerical codes are rigorous only for axisymmetric (normal) impacts of projectiles. Oblique impacts have previously been treated by two approaches:

- o 3-D codes - such codes are available, but at this time, they are of marginal utility for most real problems, due to complexity, high cost, and severely limited spatial resolution.
- o Plane strain (2-D) simulation - the projectile is treated as an infinitely wide wedge, and therefore this technique is of some qualitative utility, but plane strain calculations are not quantitatively accurate because motion and stress relief outside of the x-y plane are not allowed.

In this study, a modification of the 2-D plane strain equations has been performed which improves two-dimensional analysis capability for treating oblique impacts. The need for improving the plane strain equations can be seen in the following example which was performed early in this study.

An *axisymmetric* impact of the .50-caliber projectile into a Titanium plate at 1600 ft/sec was performed using the standard WAVE-L cylindrical symmetry code, and then repeated using the plane strain version of the WAVE-L code. Figure 23 shows a comparison of the radial compressive stress vs time for the first 6 μ sec. In the realistic cylindrical case, the radial stress is initially about 8 kbar and then gradually rises to a peak of 24 kbar. In the plane strain approximate simulations, the initial stress is higher (about 12 kbar) and the radial stress rises more rapidly to a peak of about 25 kbar and then at about

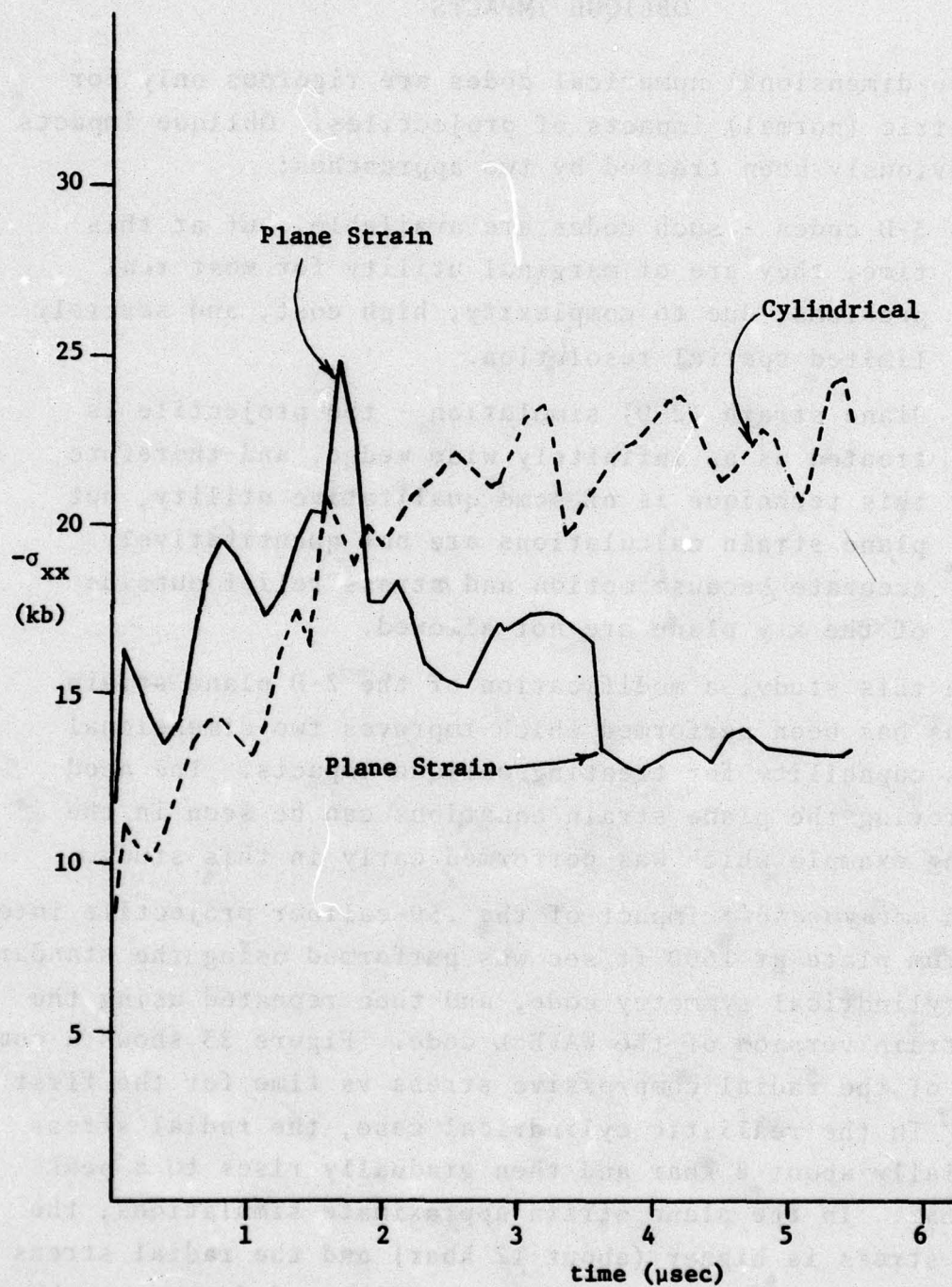


Figure 23. Comparison of Peak "Radial" Compressive Stress versus Time from the Cylindrical and Plane Strain Penetration Calculations of a Normal Impact into a Ti Plate at 1600 fps.

2 μ sec, the plane strain radial stress decreases and levels off at a low value of about 13 kbars. This is a characteristic feature for thin plate wedge impacts. A wedge will initially have higher stresses as compared to cylindrical penetrators because in the cylindrical case there is a hoop strain ($\epsilon_{\theta\theta}$) relief component which is not present in the plane strain case. At later times the reflected wave from the rear target surface causes an over estimation of relief processes in the plane strain case as compared to the cylindrical case.

The semi-elliptical coordinate scheme is a two-dimensional simulation technique which reduces to cylindrical coordinates in the limit of normal impacts. As the impact obliquity increases, the approximations become activated. This 2-D approximation method is described in Appendix A, and it has been applied to impacts at 60° obliquity on a Titanium blade and 45° obliquity on Aluminum blades.

In summary, oblique projectile penetrations through targets are seen experimentally to produce roughly elliptical holes. In the new semi-elliptical method, the usual plane strain coordinate system of the WAVE-L code is replaced with a semi-elliptical coordinate scheme which nominally matches the penetration hole in the target. Using semi-elliptical coordinates, the equations of motion are specified to account for geometric divergence outside the 2-D primary plane of the solutions. The primary plane is the plane which includes the projectile symmetry axis and velocity vector.

4.1 60° Projectile Impact on Titanium Blade

Case 5 is the 60° oblique impact of the .50-caliber penetrator on the Titanium plate. Figure 24 shows the configuration and initial conditions in the primary plane of the penetration. Figure 25 shows the velocity field 5 μ sec after impact. At this

08 AUG 75 CALIFORNIA RESEARCH AND TECHNOLOGY WAVE-L CODE
 RUN NO 2070- CASE 5 PROJECTILE PENETRATION INTO TITANIUM CELL SYN
 CYCLE 0

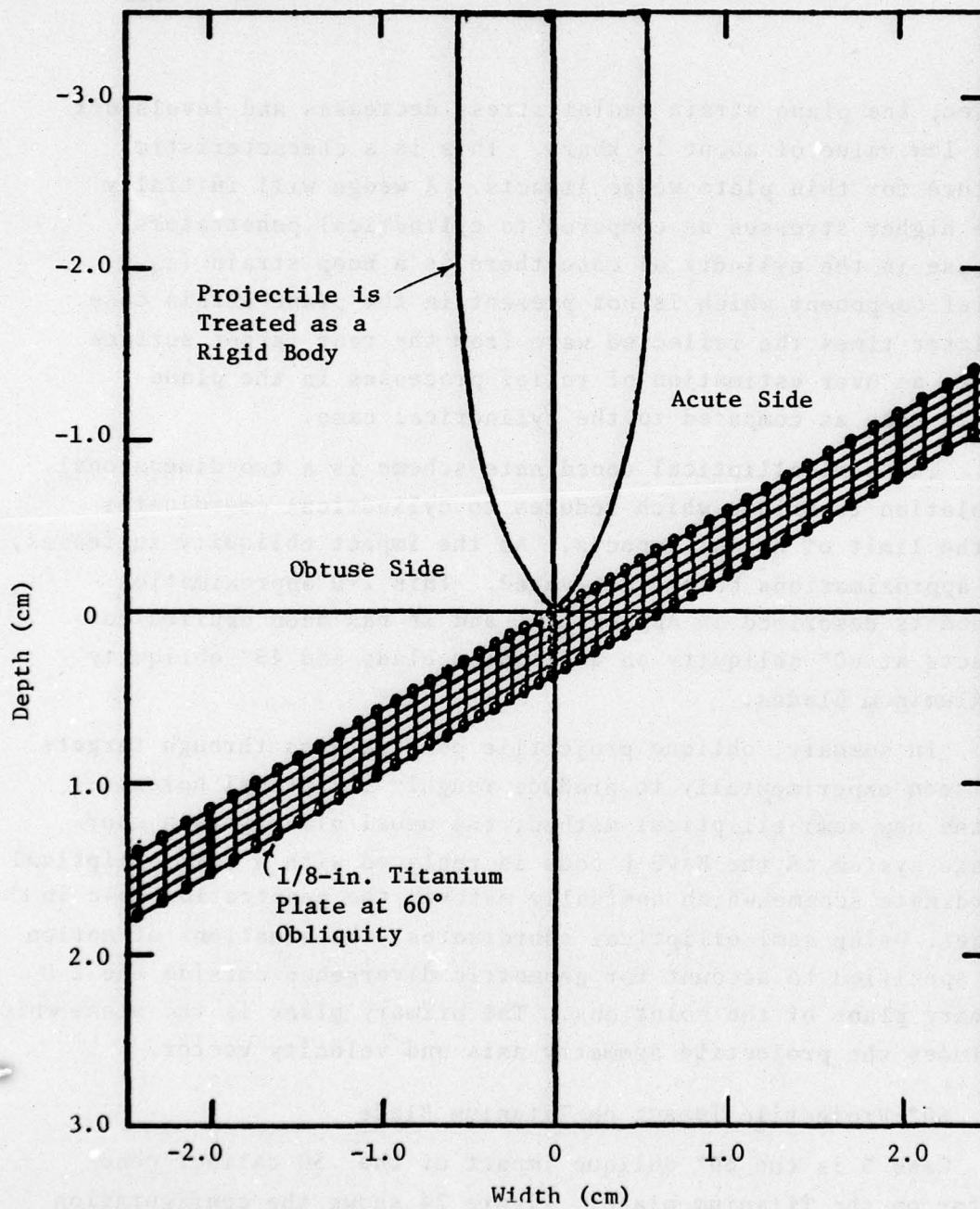


Figure 24. Initial Projectile and Target Grid Configuration for the 60° Oblique Impact on a Titanium Plate (Case 5).

time, the dominant interaction is on the acute side of the projectile-target interface. The target is accelerating normal to the penetrator surface. On the obtuse side, the penetration dynamics are much less severe and the target material is flowing up the penetrator surface as indicated in Figure 25.

Figure 26 shows the velocity field at 10 μ sec. The material on the acute side is easily deflected towards the target rear free surface as the projectile nose moves through the blade. The material on the obtuse side of the impact is compacted and driven outward by the advancing projectile nose. Also the material near the front surface on the obtuse side has a characteristic "splash" formation. This splash does not occur on the acute side of the impact.

Figure 27 shows the velocity field at 25 μ sec, and Figure 1, in Section 1.3, shows the final velocity field at 32.5 μ sec. Note in Figure 1 that the axis of the projectile has been shifted from the initial trajectory. This indicates that a slight yaw would develop which would lead to projectile tumbling. Note that in these calculations, rotation and yaw of the projectile were not treated, however, translational motion due to asymmetrical forces on the two sides of the projectile was treated. From the translational behavior, the yaw and rotational behavior can be inferred. In this thin plate impact, rotation during actual plate penetration is not a factor, however, for thicker targets, projectile rotation and yaw can create serious difficulties in predicting projectile-target interactions.

Figure 28 shows the predicted axial momentum transfer curve for the Ti oblique Case 5. The corresponding curve for the normal impact configuration is also on this figure. The two curves are very close indicating similar final momentum transfer. However, the oblique penetration remains in contact

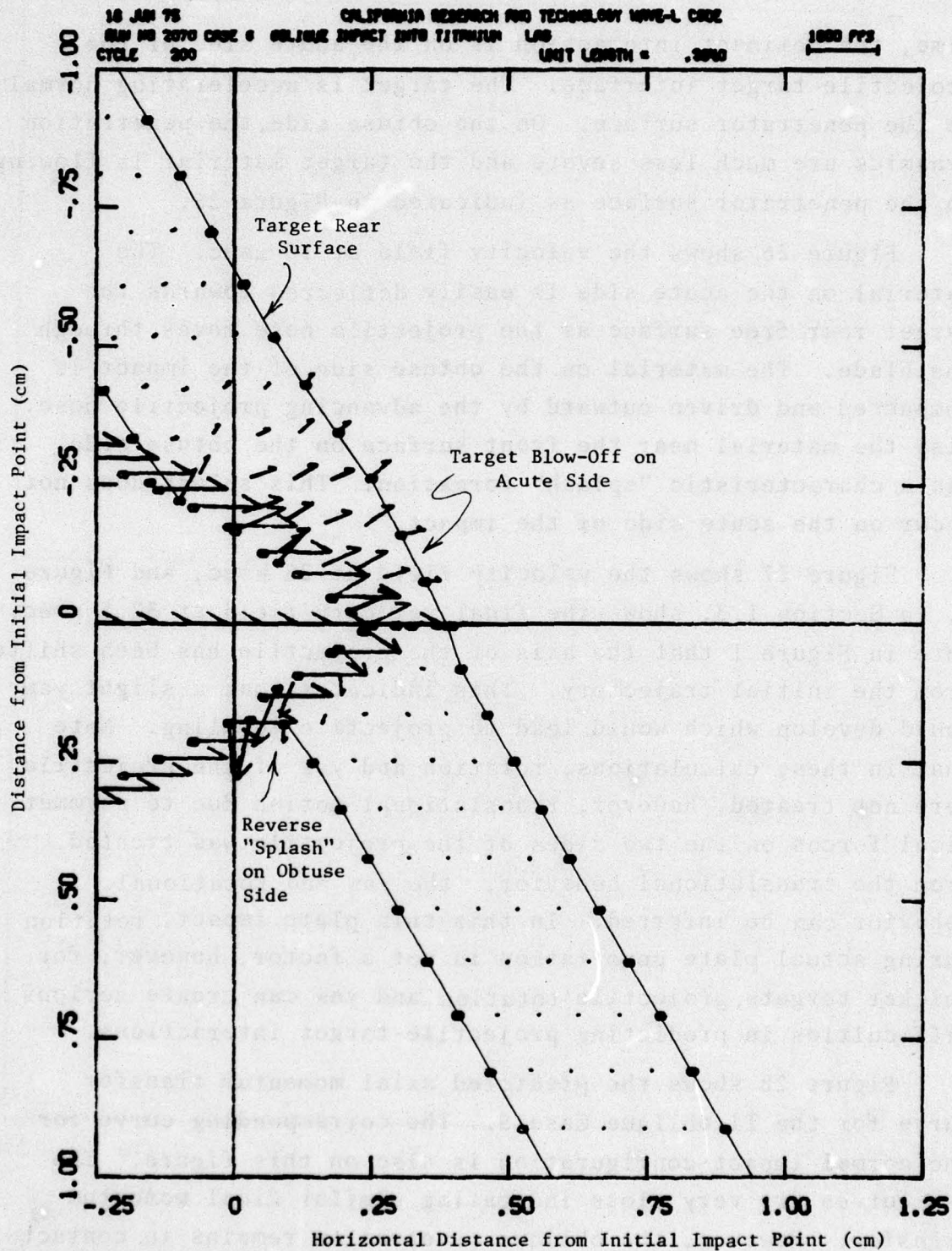


Figure 25. Velocity Field at 5 μ sec of a 1600 fps 60° Obliquity .50-Cal. Projectile Impact into 1/8-in. Titanium Blade (Case 5).

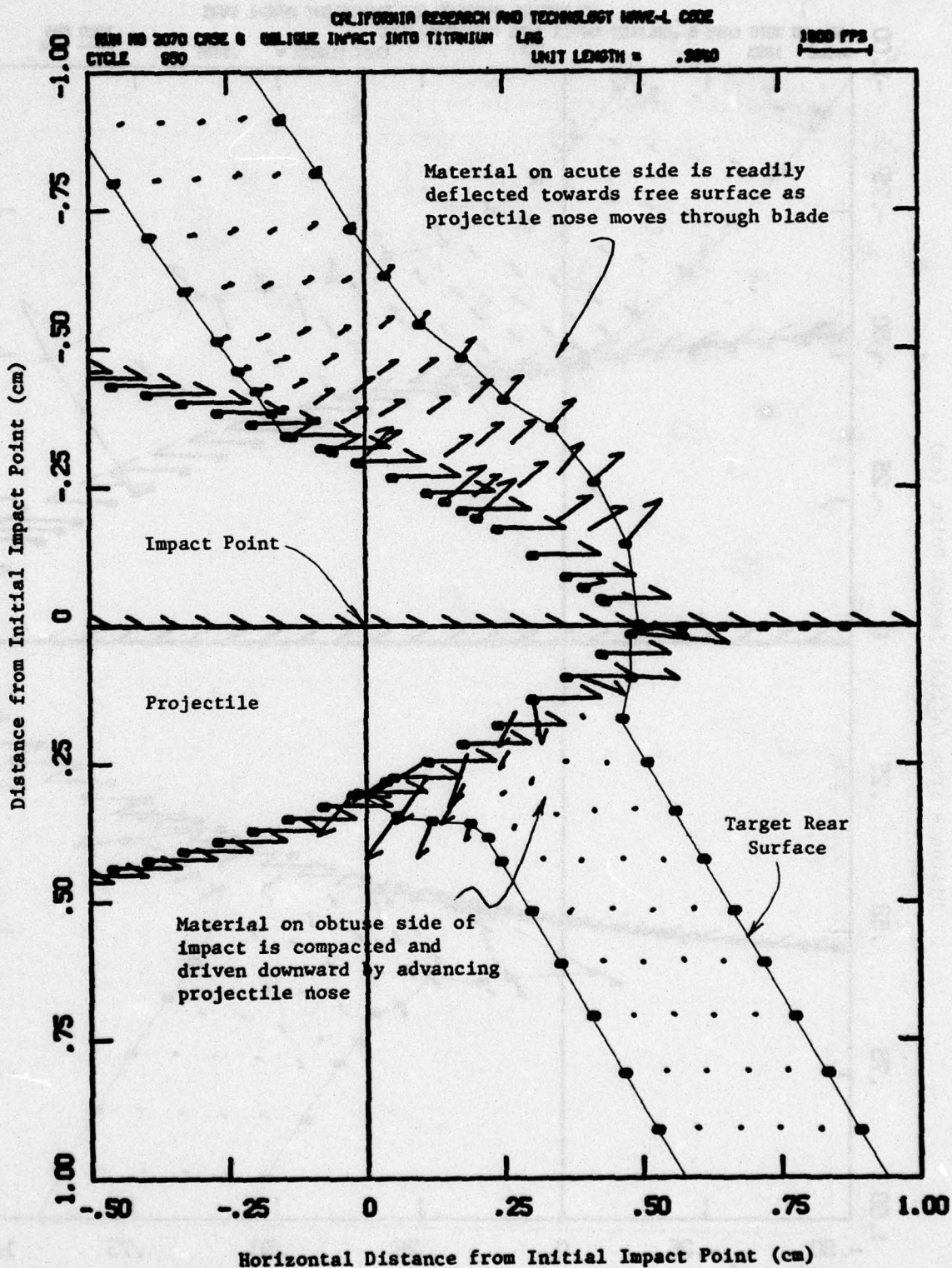


Figure 26.

Velocity Field at 10.3 μ sec of a 1600 fps 60° Obliquity
 .50-Cal. Projectile Impact into 1/8-in. Titanium Blase
 (Case 5).

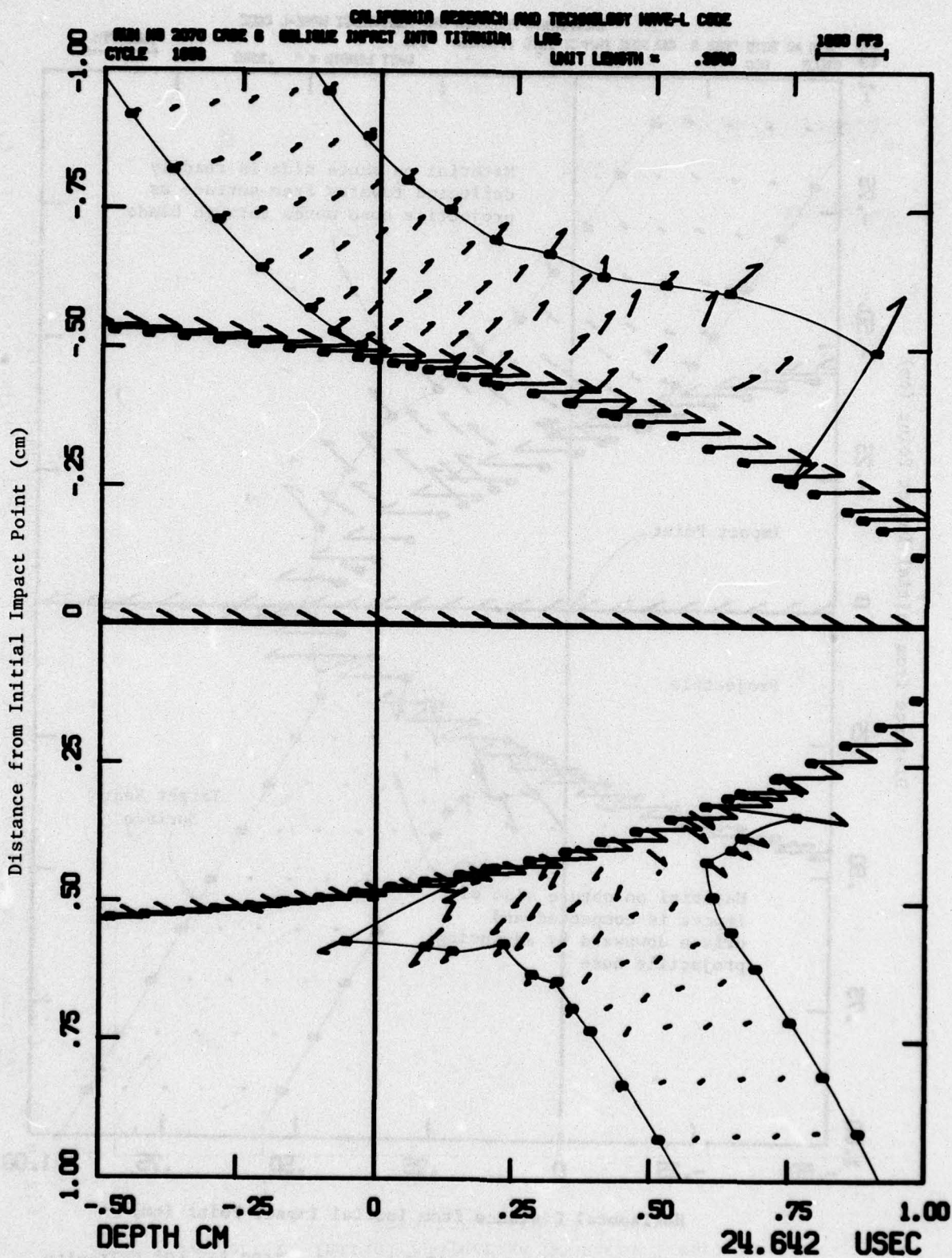


Figure 27. Velocity Field at 25 μsec of a 1600 fps 60° Obliquity .50-Cal. Projectile Impact into 1/8-in. Titanium Blade (Case 5).

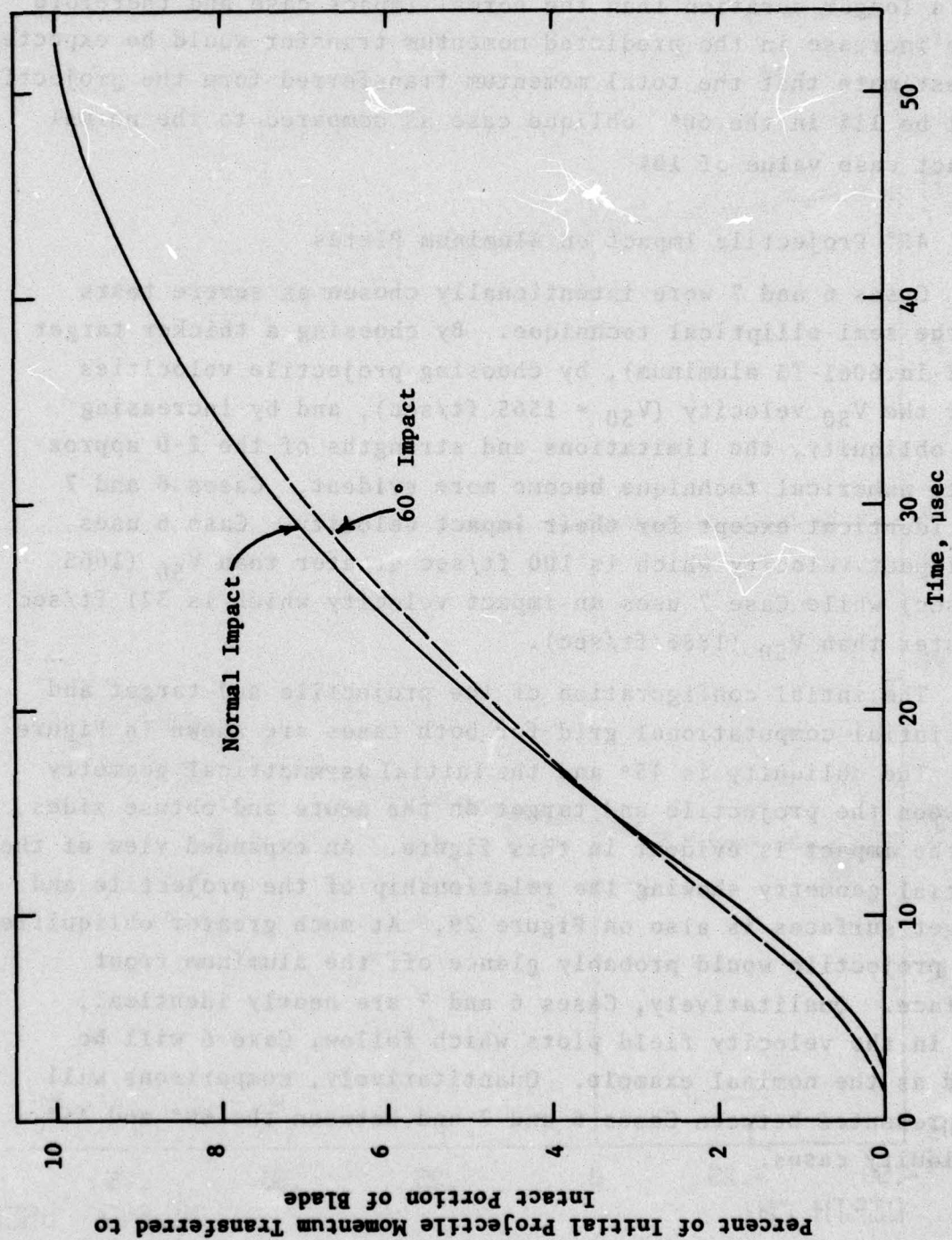


Figure 28. Comparison Showing Transfer of Projectile Momentum to Titanium Blades During Normal and 60° Oblique Impacts of .50-Cal. Projectile at 1600 fps.

for a longer duration than the normal impact case and therefore some increase in the predicted momentum transfer would be expected. We estimate that the total momentum transferred from the projectile will be 11% in the 60° oblique case as compared to the normal impact case value of 10%

4.2 45° Projectile Impact on Aluminum Plates

Cases 6 and 7 were intentionally chosen as severe tests of the semi-elliptical technique. By choosing a thicker target (1/2-in. 6061-T3 aluminum), by choosing projectile velocities near the V_{50} velocity ($V_{50} = 1565$ ft/sec), and by increasing the obliquity, the limitations and strengths of the 2-D approximate numerical technique become more evident. Cases 6 and 7 are identical except for their impact velocity. Case 6 uses an impact velocity which is 100 ft/sec greater than V_{50} (1665 ft/sec) while Case 7 uses an impact velocity which is 321 ft/sec greater than V_{50} (1886 ft/sec).

The initial configuration of the projectile and target and the initial computational grid for both cases are shown in Figure 29. The obliquity is 45° and the initial asymmetrical geometry between the projectile and target on the acute and obtuse sides of the impact is evident in this figure. An expanded view of the initial geometry showing the relationship of the projectile and target surfaces is also on Figure 29. At much greater obliquities the projectile would probably glance off the aluminum front surface. Qualitatively, Cases 6 and 7 are nearly identical; and in the velocity field plots which follow, Case 6 will be used as the nominal example. Quantitatively, comparisons will be presented between Cases 6 and 7 and between the 60° and 45° obliquity cases.

BEST AVAILABLE COPY

15 SEP 78
POQ III CASE 1 OBLIQUE PENETRATION IN TO ALUMINUM
CYCLE 0

CALIFORNIA RESEARCH AND TECHNOLOGY WAVE-L CODE

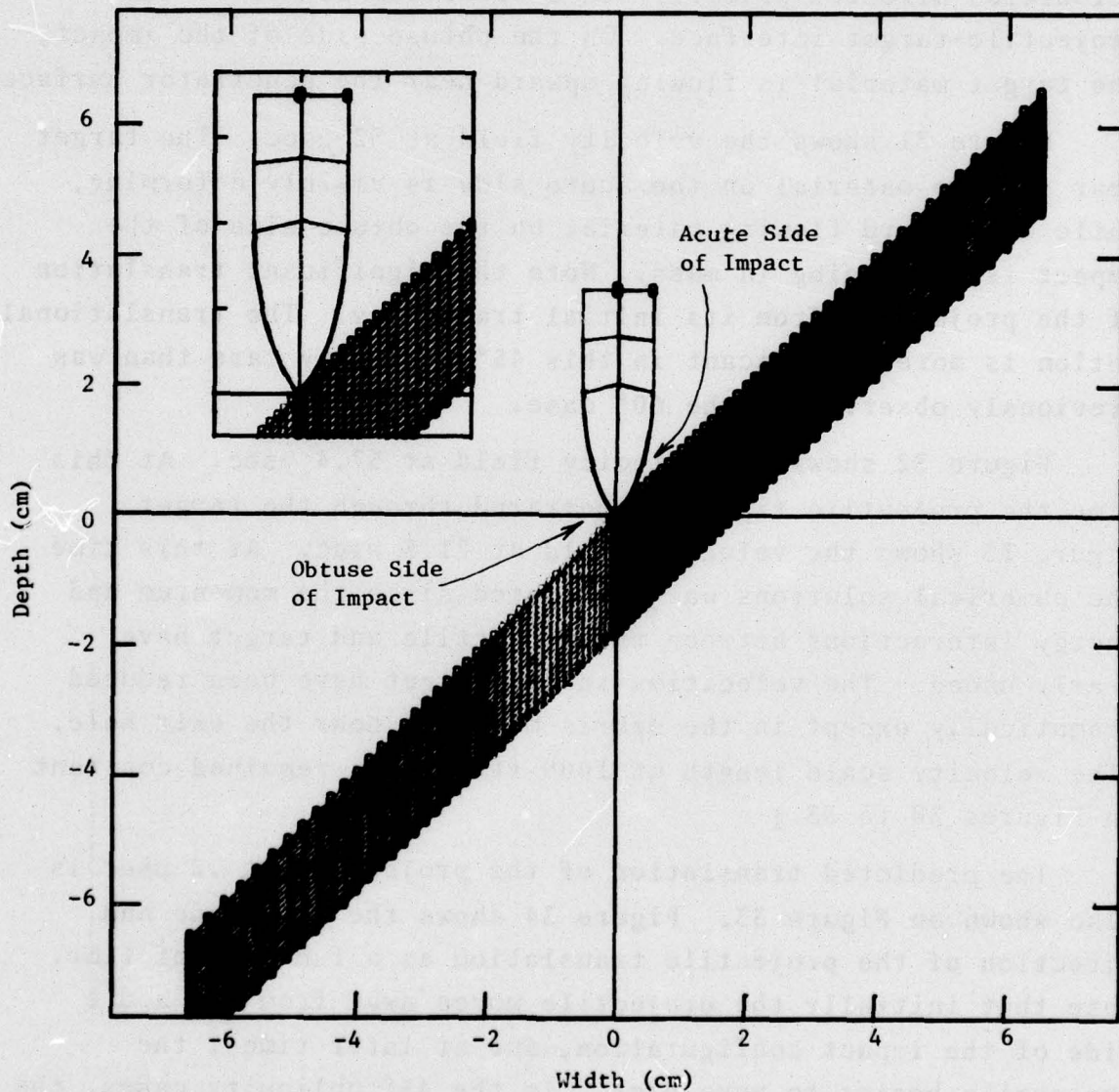


Figure 29. Initial Configuration and Computational Grid for 45° Obliquity Impacts of .50 Caliber Projectiles on 1/2-in. Aluminum Plate (Cases 6 and 7).

Figure 30 shows the velocity field at 13 μ sec for Case 6. The interaction is very strong on the acute side of the impact. The primary target response consists of momentum and material velocities directed primarily in a direction normal to the projectile-target interface. On the obtuse side of the impact, the target material is flowing upward near the penetrator surface.

Figure 31 shows the velocity field at 32 μ sec. The target rear surface material on the acute side is visibly deforming, while the upward flowing material on the obtuse side of the impact is increasing in mass. Note the significant translation of the projectile from its initial trajectory. The translational motion is more significant in this 45° obliquity case than was previously observed in the 60° case.

Figure 32 shows the velocity field at 57.4 μ sec. At this time the projectile tip has penetrated through the target. Figure 33 shows the velocity field at 71.5 μ sec. At this time the numerical solutions was terminated since the momentum and energy interactions between the projectile and target have nearly ended. The velocities in the target have been reduced dramatically except in the debris material near the exit hole. (The velocity scale length of 1000 ft/sec has remained constant in Figures 30 to 33.)

The predicted translation of the projectile at 72 μ sec is also shown on Figure 33. Figure 34 shows the magnitude and direction of the projectile translation as a function of time. Note that initially the projectile moves away from the acute side of the impact configuration, and at later times, the projectile begins to move back. In the 45° obliquity cases, the *exiting* projectile trajectory is translated (and therefore yawed) toward the obtuse side. In the 60° Titanium case, however, the reverse motion from the obtuse side toward the

BEST AVAILABLE COPY

UNIT= 2.00E-01

CALIFORNIA RESEARCH AND TECHNOLOGY, INC.
 PGD 111 CASE 2 OBLIQUE PENETRATION IN TO ALUMINUM
 CYCLE 1298

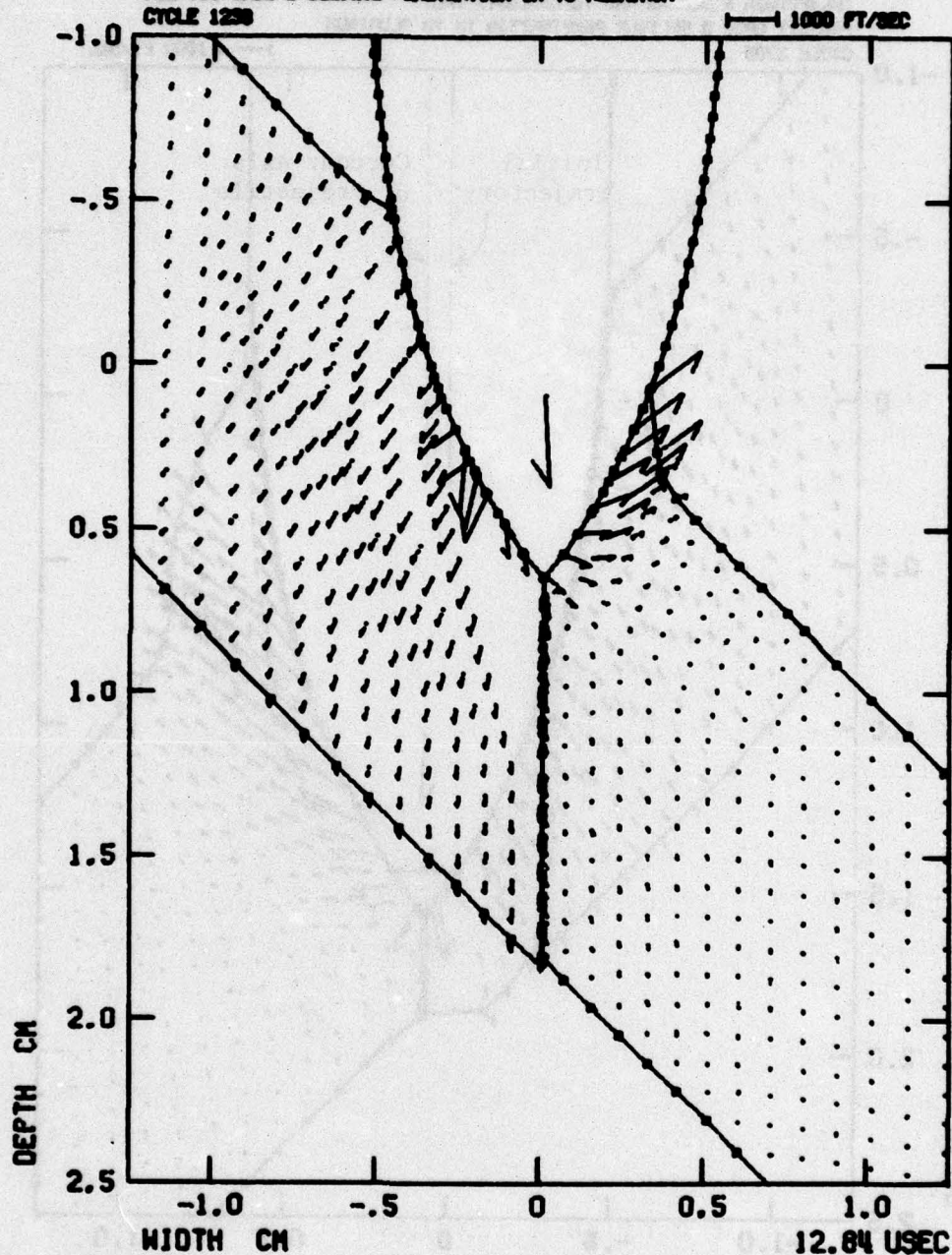


Figure 30. Velocity Field Plot at 13 μ sec of .50 Caliber Projectile Impact at 45° Obliquity (Case 6).

BEST AVAILABLE COPY

UNIT = 2.00E-01

CALIFORNIA RESEARCH AND TECHNOLOGY, INC.
 PRO 111 CASE 2 OBLIQUE PENETRATION IN TO ALUMINUM
 CYCLE 2705

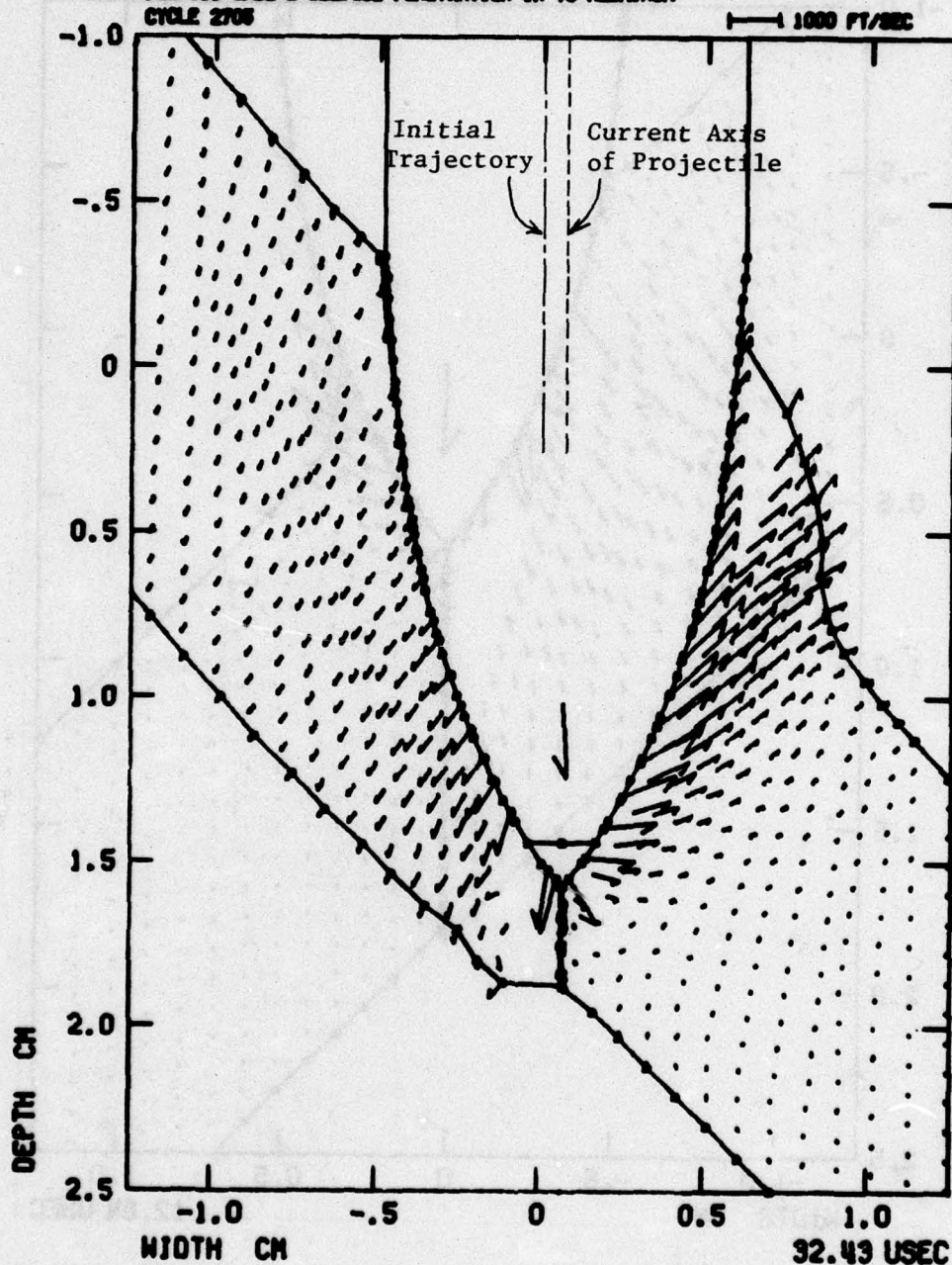


Figure 31. Velocity Field Plot at 32 μ sec of .50-Caliber Projectile Impact at 45° Obliquity (Case 6)

BEST AVAILABLE COPY

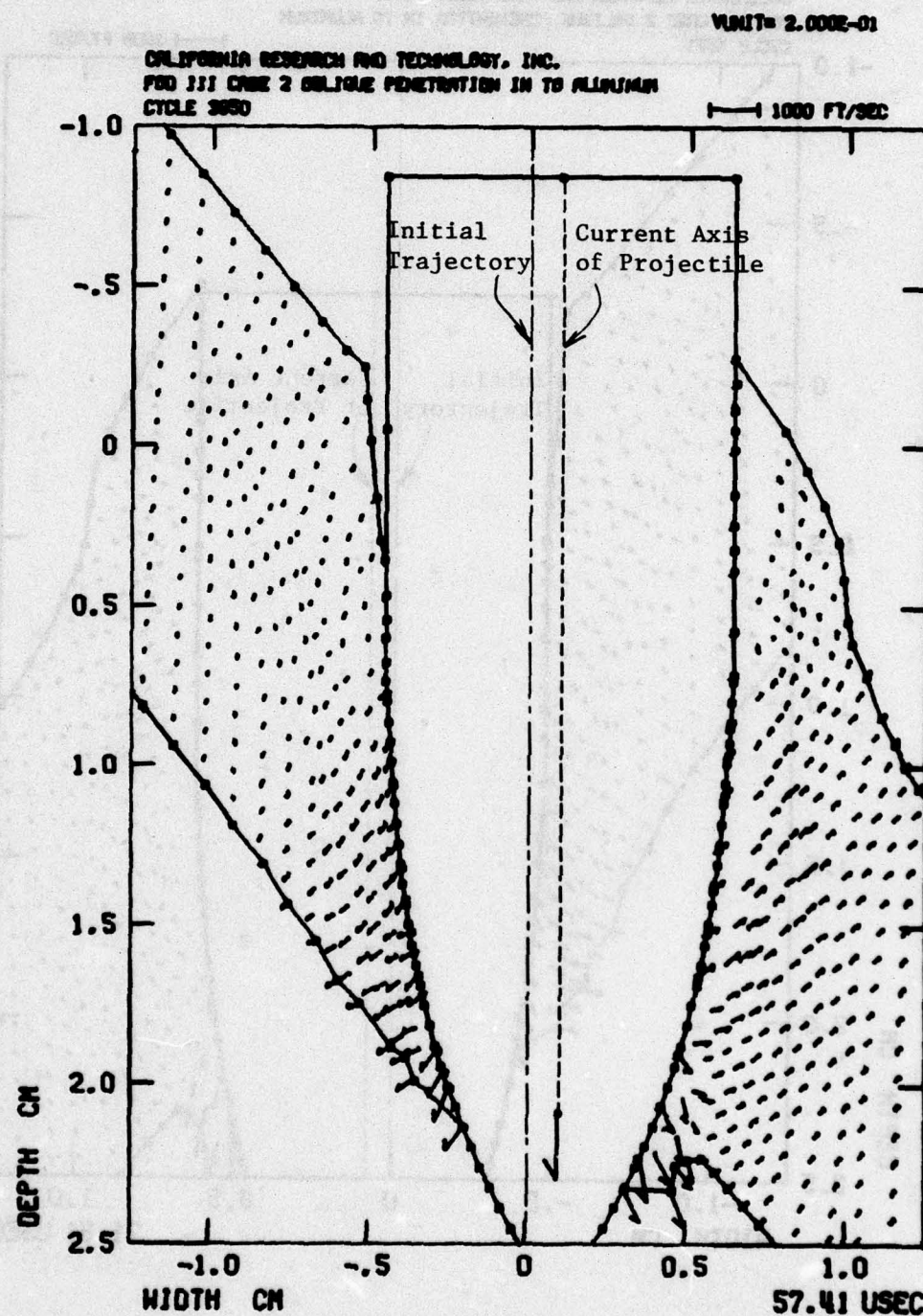


Figure 32. Velocity Field Plot at 57 μ sec of .50-Caliber Projectile Impact at 45° Obliquity (Case 6).

BEST AVAILABLE COPY

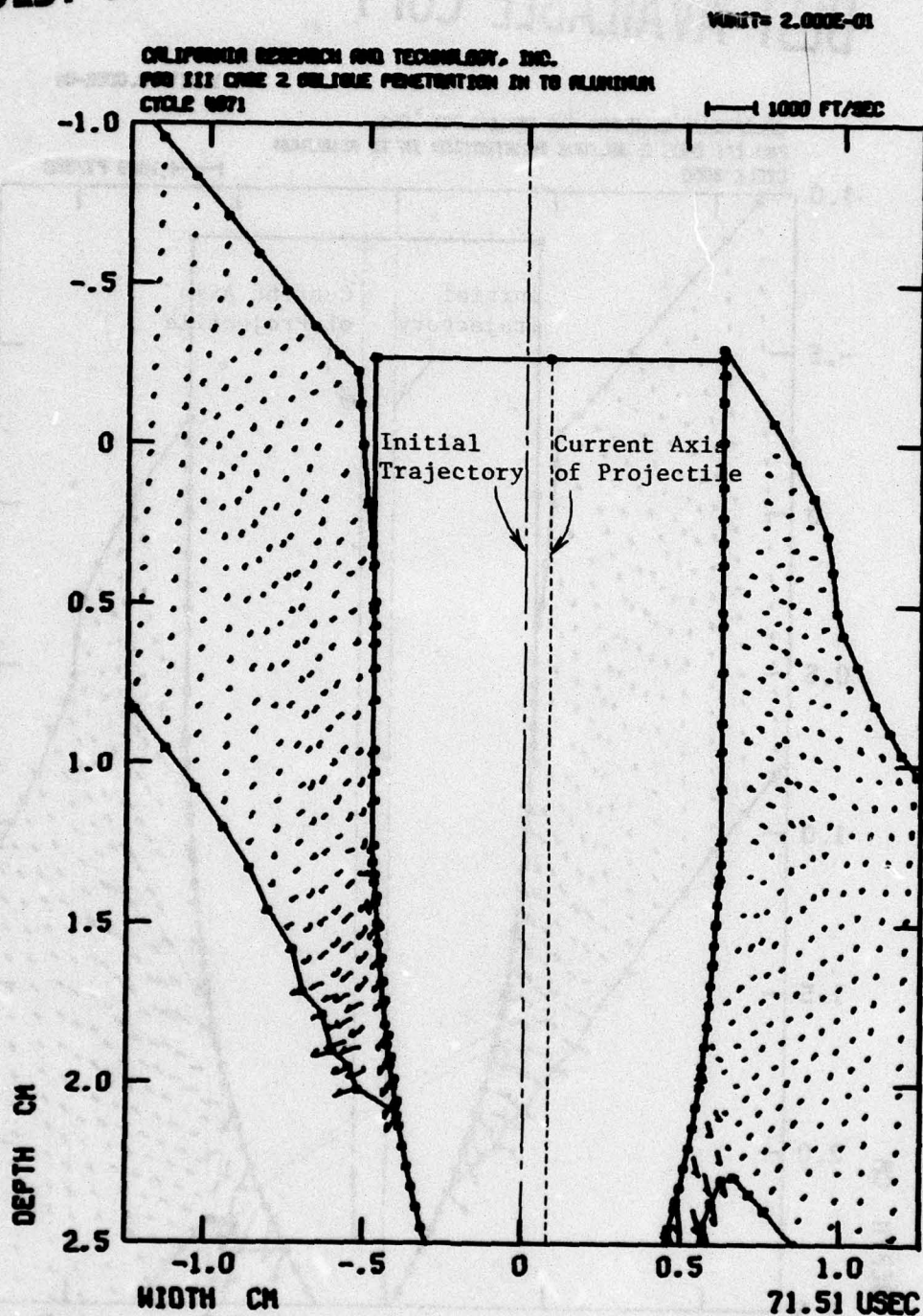


Figure 33. Velocity Field Plot at 72 μ sec of .50-Caliber Projectile Impact at 45° Obliquity (Case 6).

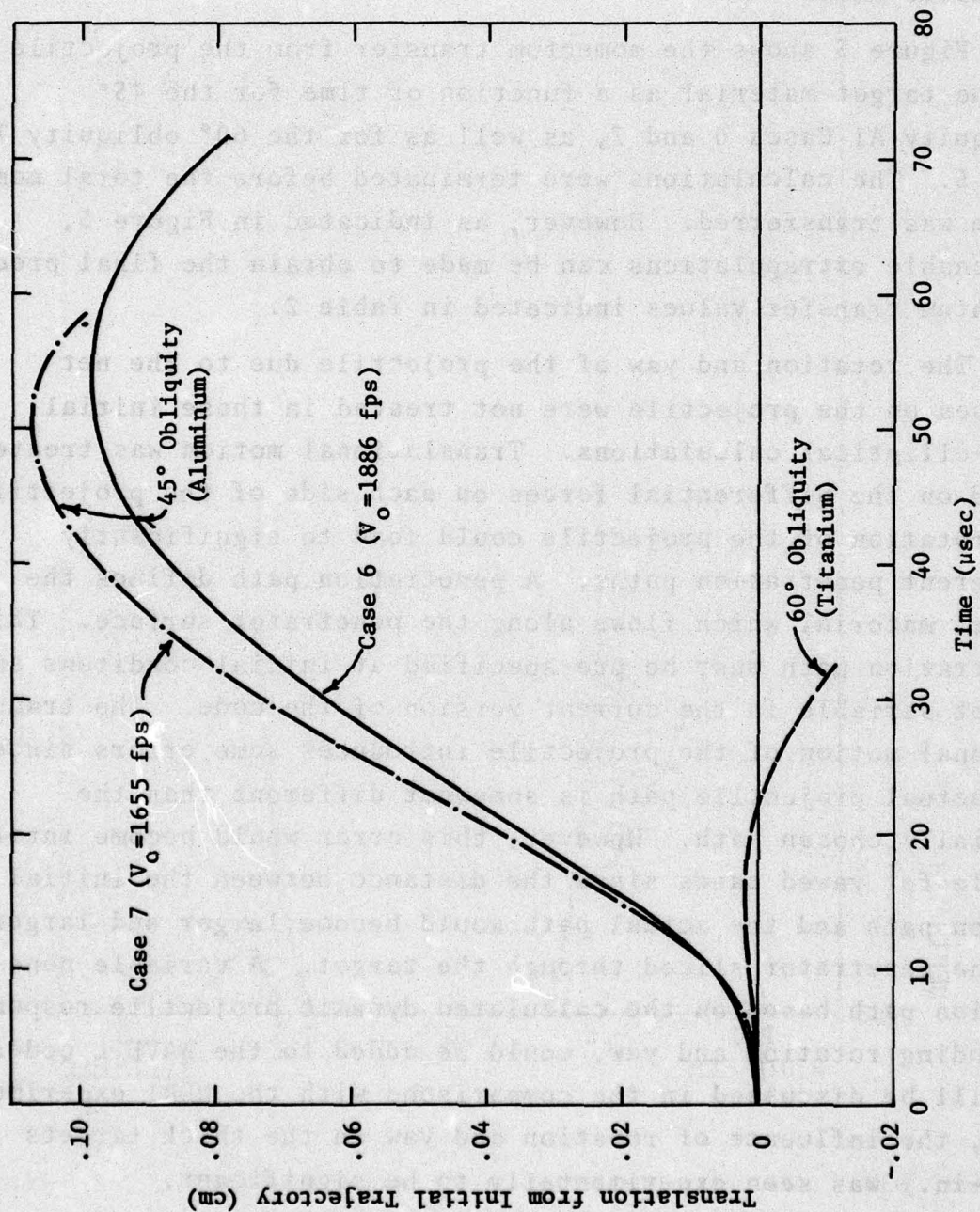


Figure 34. Translation of Projectile Axis from Initial Trajectory vs Time for 45° and 60° Obliquity Cases.

acute side was greater than the initial motion and the projectile in the 60° case exited with a net translation directed toward the acute side.

Figure 5 shows the momentum transfer from the projectile to the target material as a function of time for the 45° obliquity A1 Cases 6 and 7, as well as for the 60° obliquity Ti Case 5. The calculations were terminated before the total momentum was transferred. However, as indicated in Figure 5, reasonable extrapolations can be made to obtain the final predicted momentum transfer values indicated in Table 2.

The rotation and yaw of the projectile due to the net torques on the projectile were not treated in these initial semi-elliptical calculations. Translational motion was treated based on the differential forces on each side of the projectile, but rotation of the projectile could lead to significantly different penetration paths. A penetration path defines the target material which flows along the penetrator surface. This penetration path must be pre-specified at initial conditions and is not variable in the current version of the code. The translational motion of the projectile introduces some errors since the actual projectile path is somewhat different than the initially chosen path. However, this error would become intolerable for yawed cases since the distance between the initial chosen path and the actual path would become larger and larger as the penetrator sliced through the target. A variable penetration path based on the calculated dynamic projectile response, including rotation and yaw, could be added to the WAVE-L codes. As will be discussed in the comparisons with the UDRI experimental data, the influence of rotation and yaw in the thick targets (1/2-in.) was seen experimentally to be significant.

4.3 Experimental Comparisons for Oblique Impacts

4.3.1 60° Impacts on 1/8-in. Titanium Plates

Figure 35 shows the experimental data for the 60° oblique impacts on the 1/8-in. Titanium plates. The momentum transfer to the *intact plate* decreases rapidly as the impact velocity increases. Also on this figure is the predicted value of 9% from the Case 5 calculation.

The agreement is very good when one considers that

- 1) the semi-elliptical technique is a 2-D approximation to a 3-D problem, and
- 2) uncertainties exist in the experiments because in all the Titanium impact cases, except one, the .50-caliber projectile broke in two or more pieces. (The effect of projectile break-up on momentum transfer for oblique penetrations is not understood.)

4.3.2 45° Impacts on 1/2-in. Aluminum Plates

Appendix C contains the UDRI experimental procedure and their experimental results on the thick aluminum (1/2-in.) targets at 45° obliquity. The projectile velocity was measured before and after impact, and the total projectile momentum transfer was calculated. Mass loss of the target was consistently small. This mass loss resulted from the petalled portions of the target rear surface being broken off, or small particles being pulled out by the grooves of the ogives. The average target mass loss was .16 grams.

In the experimental program, V_{50} was determined to be 1565 ft/sec. Penetrations of the 1/2-in. thick Aluminum targets at 45° obliquity were then performed up to 842 m/sec = 2762 ft/sec. The following parameters were measured during

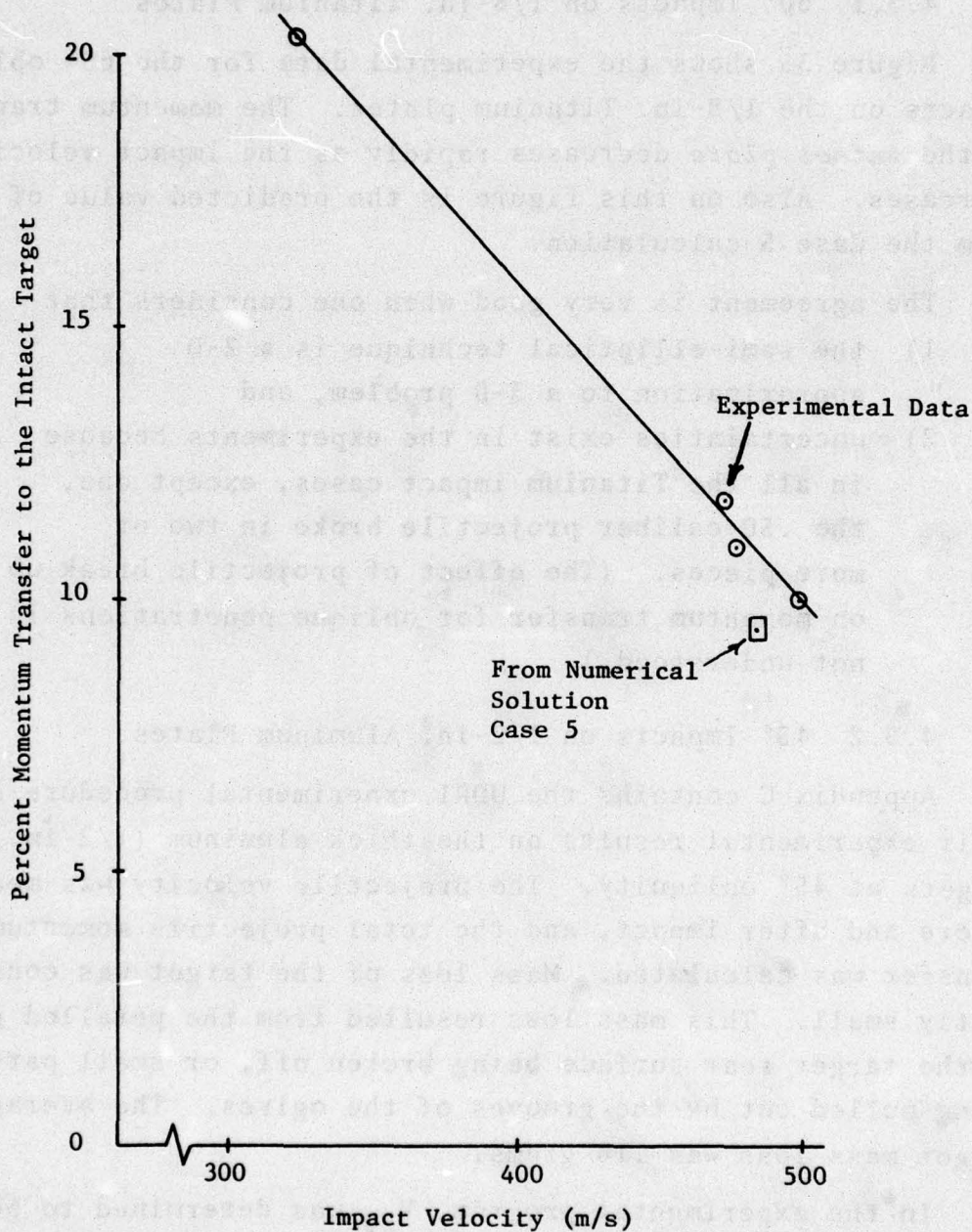


Figure 35. Experimental-Numerical Comparison of the Percentage Momentum Transfer to the Intact Titanium Blase versus the Impact Velocity for the 60° Oblique Impact of a .50-Caliber Projectile.

twelve experiments and are listed in Table 5: the impact and residual velocities of the projectile, the momentum lost by the projectile, the mass lost by the target, and the angular change in the trajectory of the projectile.

The momentum transfer data is plotted in Figure 7. The projectile loses more than 50% of its momentum for an impact velocity near V_{50} . A minimum momentum loss of 10.5% occurs for the maximum velocity of 2762 ft/sec. There is considerable scatter in the data; especially at the lower impact velocities. Similar projectile impact velocities results in widely different momentum transfer values.

An uncontrollable yaw of the projectile was experimentally observed in the photographs used to determine the initial impact velocity. (Yaw occurs when the projectile velocity vector is not aligned with the projectile symmetry axis.) This initial yaw or observed wobble was usually less than $\pm 2.8^\circ$. However, we believe that this yaw variation is a major cause of the scatter in projectile momentum. This is an important conclusion of this experimental and numerical investigation. Also, experiments with earth penetrators have indicated that small yaw angles (1° - 5°) can have significant influence on the stress loads between a projectile and target¹².

Projectile yaw is relevant not only during initial impact, but also during the penetration process and the exiting process. Figure 36 from the UDRI experimental results show a dramatic example of projectile yaw during the exiting phase of the projectile. At 138 μ sec, in Figure 36, the projectile is exiting in an upward orientation; however, as shown very clearly in the 5 remaining frames, the projectile rotates and its final trajectory is directed in a downward direction. The importance of projectile yaw and rotation in determining the projectile-target interaction should be examined in more detail both experimentally and computationally.

TABLE 5. EXPERIMENTAL DATA FROM THE 45° OBLIQUE IMPACTS
INTO 1/2-IN. ALUMINUM PLATES

Shot #	V_i (m/s)	V_r (m/s)	ΔP (%)	ΔM (gm)	θ (degrees)
5862	456	178	60.9	-0.30	9.4
5841	457	226	50.7	-0.05	12.1
5860	462	167	63.9	-0.01	5.0
5850	493	182	63.2	-1.00	6.2
5854	519	330	36.5	-0.10	8.9
5857	524	309	40.8	-0.05	6.4
5846	589	386	37.7	+0.07	5.6
5855	628	495	21.1	0.00	4.1
5852	637	492	22.7	-0.10	5.4
5861	641	507	20.8	-0.12	5.7
5849	688	539	21.7	0.00	3.1
5863	842	754	10.6	-0.20	0.0

V_i = impact velocity

V_r = residual velocity

ΔP = percent momentum transferred from projectile

ΔM = target mass loss

θ = change in projectile trajectory

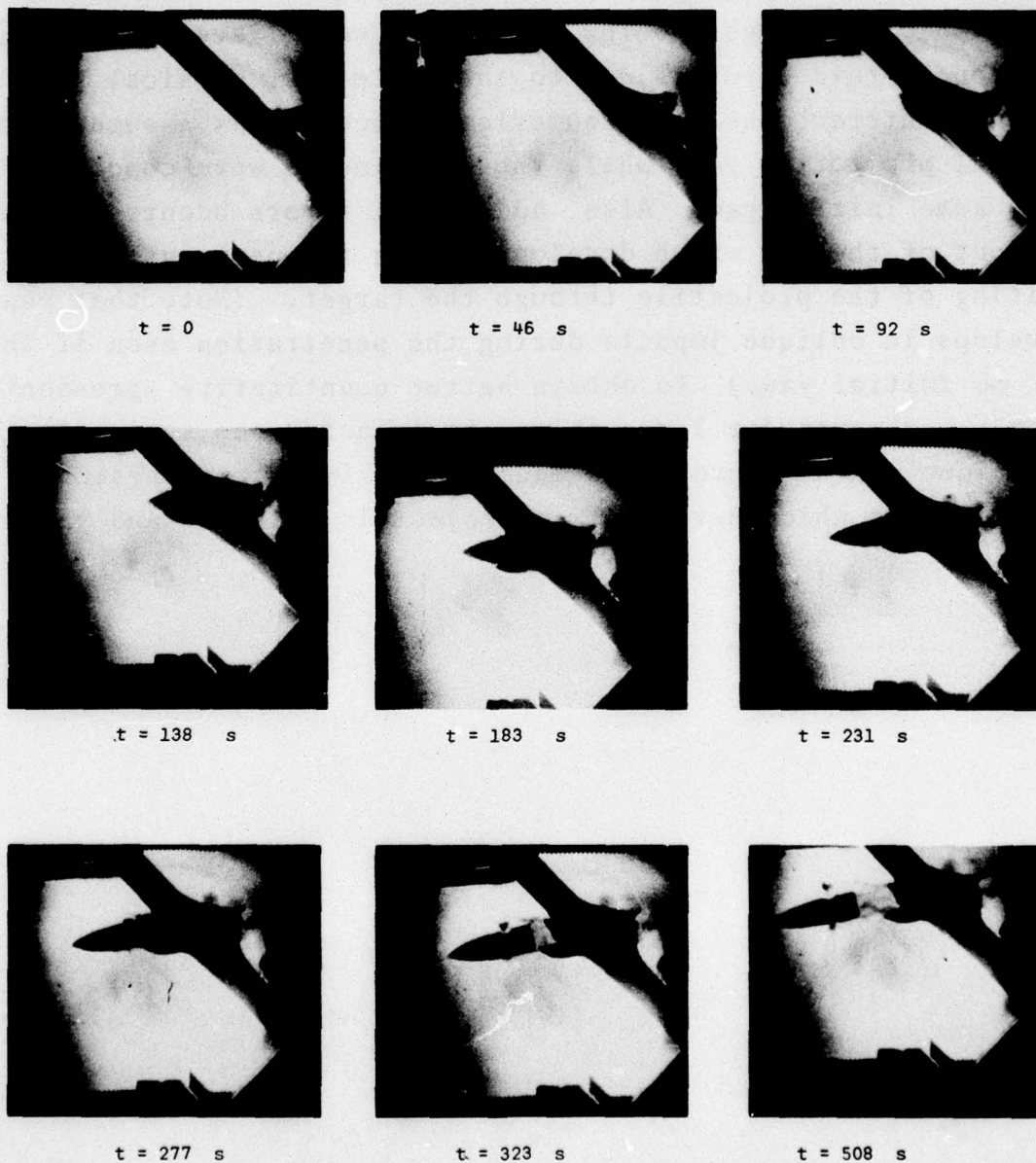


Figure 36. Framing Camera Record of Projectile Penetration through a Thick Target (UDRI Experimental Results, see Appendix B).

In the numerical calculations the effects of rotation and yaw were basically ignored due to computational difficulties which were not within the scope of the current effort. Figure 7, in Section 1.3, shows the predicted momentum transfer as a function of the two impact velocities used in Cases 6 and 7. The predicted values are low. However, we believe that the major portion of this error is due to the neglect of physical yaw induced interactions. The numerical calculations assumed zero initial projectile yaw, while the experiments were conducted with some initial yaw. Also, additional errors occurred in the neglect of the yaw which develops during the penetration and exiting of the projectile through the target. (Note that yaw develops in oblique impacts during the penetration even if there is no initial yaw.) To obtain better quantitative agreement with experiments for large obliquity impacts, the semi-elliptical technique can be improved to include the important physical interactions which develop from projectile rotation and yaw.

SECTION V

RECOMMENDATIONS

The following recommendations are made based on the results of this numerical-experimental investigation of normal and oblique impacts on fan blades:

- o Composite blade materials should be investigated further to better understand the influence of *ductility, yield, and ply (or anisotropic) tensile strengths* on local blade damage and momentum transfer.
- o The influence of projectile yaw and rotation upon impact, during target penetration, and during the exiting phase should be investigated further using both experimental and numerical techniques.
- o The numerical approach for normal impacts should be applied to other blade materials of potential interest, including advanced composites. Sensitivity studies can be performed on parameters which are either uncertain or variable
- o The semi-elliptical approximation technique can and should be expanded to include the effects of projectile yaw and rotation. Once this code modification is completed, the 2-D technique will be a powerful tool for investigating quantitative aspects of realistic 3-D oblique impacts on turbine blades as well as other thicker targets of interest to the Air Force.

REFERENCES

1. Wilkins, M. L., Lawrence Radiation Laboratory, *Calculation of Elastic-Plastic Flow*, January 1969. (UCRL-7322, Rev. I.)
2. M. H. Wagner, *Analytical Study of Penetration Mechanics*, Shock Hydrodynamics Rpt 3030-2020FR, Contract Nool23-68-C-0839, May 1969.
3. M. H. Wagner, *Analytical Studies of Projectile Design and Performance*, Shock Hydrodynamics Rpt 7584-06, Contract DAAG05-70-C-0584, 1971.
4. M. H. Wagner, K. N. Kreyenhagen, and W. S. Goerke, *Numerical Analysis of DNA Earth Penetrator Experiment at DRES*, DNA 3537F, June 1975.
5. M. H. Wagner, C. C. Fulton, and K. N. Kreyenhagen, *Finite Difference Code Analyses of Earth Penetrator Dynamics in Rock Media*, DNA 4069, November 1976.
6. M. Rosenblatt and K. N. Kreyenhagen, *SHAPE Code Modifications and Sensitivity Analyses*, SAMSO-TR-68-70, January 1968
7. *Military Handbook 5 - Property Data for Ti-6Al-4V Alloy*, Appendix to Battelle Memorial Institute Handbook, "Titanium Base Alloys, 6Al-4V", 1967.
8. Green, Babcock, and Maiden, *High Temperature Compression Strain-Rate Tests on Six Engineering Materials*, G.M. Defense Research Laboratories, 1966.
9. Young and Carlson, *Advanced Composite Material Structural Program*, AFML-TR-70-140, Vols. I and II.
10. P. W. R. Beaumont and B. Harris, *The Energy of Crack Propagation in Carbon Fibre-Reinforced Resin Systems*, J. of Materials Sci 7 (1972), pp. 1265-1279.
11. M. Rosenblatt, G. E. Eggum, L. A. DeAngelo, and K. N. Kreyenhagen, *Numerical Investigation of Water Drop Erosion Mechanisms in Infrared-Transparent Materials*, AFML-TR-76-193, December 1976.

REFERENCES (Cont'd)

12. AVCO Corporation, *Impact and Penetration Technology*, Progress Report No. 2, July 1976.
13. Rice, Walsh, and McQueen, *Compression of Solids by Strong Shock Waves*, Solid States Physics, Vol. 6, 1958.
14. Barber, John P., Taylor, Henry R., "Ordnance Impacts on Jet Engine Fan Blades", AFML-TR-76-34, April 1976.

REFERENCES (Cont'd)

11. AEC Corporation, "Titanium and Aluminum Material Models", Progress Report No. 1, July 1970.
12. R. W. Smith and M. J. Mooney, "Computerized Analysis of Stress in Titanium and Aluminum", Solid State Physics, Vol. 18, 1971.

APPENDIX A

DETAILS OF THE TITANIUM AND ALUMINUM MATERIAL MODELS AND OF THE SEMI-ELLIPTICAL COORDINATE METHOD

APPENDIX A

DETAILS OF THE TITANIUM AND ALUMINUM MATERIAL MODELS AND OF THE SEMI-ELLIPTICAL COORDINATE METHOD

A.1 Titanium Constitutive Model.

The Titanium is treated as a hydrodynamic-elastic-plastic material. The *hydrodynamic properties* are based on the Mie-Grüneisen equation of state

$$P = f(\rho) + \gamma p_e \quad (A-1)$$

where f and γ depend only on density (ρ). γ is the Grüneisen ratio which is assumed constant at a value of $\gamma = 1.18$ for Titanium (Ref. 1). The shock Hugoniot is specified by an experimentally measured (Ref. 13) linear relationship between shock velocity (D) and Hugoniot particle velocity (U_H). In particular, we use

$$D = A + B U_H \quad (A-2)$$

where for Titanium (Ref. 13)

$$A = .4786 \text{ cm/sec}$$

$$B = 1.066$$

Equation A-2 specifies the shock Hugoniot, and furthermore, it determines the form of $f(\rho)$ in the hydrodynamic equation of state (Eq. A-1). The result for $f(\rho)$ is

$$f(\rho) = \frac{\rho_0 A^2 \mu (1+\mu) (1 - \frac{\gamma}{2} \mu)}{(1 - (B-1)\mu)^2} \quad (A-3)$$

where $\mu = \rho/\rho_0 - 1$, $\rho_0 = 4.51 \text{ gm/cm}^3$.

Note that the hydrodynamic equations of state (Eqs. 1 and 3) depend only on the three experimentally determined parameters, A, B, and γ .

The *elastic properties* are specified by any two elastic constants. However, one of the elastic constants, namely the bulk modulus, K, is determined by the hydrodynamic equation of state.

In particular,

$$K = \rho_0 \left(\frac{dP}{d\rho} \right)_{\rho=\rho_0} = \rho_0 A^2 = 1.03 \text{ Mbars.}$$

The shear modulus, G, is used as the second elastic constant. $G = 6.2 \times 10^6 \text{ psi} = .43 \text{ Mb}$ represents a handbook value for Ti-6Al-4V alloy (Ref. 7).

Using these values of K and G, the complete set of elastic constants and wave speeds are determined. Table A-1 summarizes these elastic properties. Note that Young's modulus of $16.3 \times 10^6 \text{ psi}$ agrees very well with measured values on Ti-6Al-4V in Ref. 7.

Table A-1. Elastic Properties of Ti-6Al-4V

Bulk modulus,	K = 1.03 Mb	= $14.9 \times 10^6 \text{ psi}$
Shear Modulus,	G = .43 Mb	= $6.2 \times 10^6 \text{ psi}$
Young's Modulus,	E = 1.13 Mb	= $16.3 \times 10^6 \text{ psi}$
Poisson's Ratio,	$\nu = .32$	
Dilational Wave Speed,	$C_D = .6 \text{ cm}/\mu\text{sec}$	= 19,500 ft/sec
Shear Wave Speed,	$C_S = .3 \text{ cm}/\mu\text{sec}$	= 10,000 ft/sec

A perfectly-plastic yielding model is assumed for Titanium. The yield value is $Y = 165$ Ksi. For tensile failure, we assume a nominal strain to failure (ductility) value of 10%.

A.2 Aluminum Constitutive Properties

The Aluminum material model is also hydrodynamic-elastic-plastic in nature. The hydrodynamic portion of the 6061-T6 Aluminum is modeled with the Los Alamos hydrodynamic equation of state described in Table A-2. This equation of state implies an elastic bulk modulus of .791 Mb. The elastic shear modulus is $G = .274$ Mb.

Table A-2. Hydrodynamic Equation of State for 6061-T6 Al
Los Alamos Form.

$$P = \frac{A + B\epsilon + C\epsilon^2}{\epsilon_0 + \epsilon}$$

where

$$\epsilon = \rho_0 e$$

$$\mu = \eta - 1$$

$$A = \mu(a_1 + a_2|\mu|)$$

$$B = b_0 + b_1\mu + b_2\mu^2$$

$$C = c_0 + c_1\mu$$

CONSTANTS:

	<u>Aluminum*</u>
ρ_0	2.7
a_1	1.1867
a_2	0.7630
b_0	3.445
b_1	1.545
b_2	0.9643
c_0	0.4338
c_1	0.5487
ϵ_0	1.5

* Source of data:

L-401, 8 Jan. 1960, R. L. Bjork, The RAND Corporation

The inelastic properties are treated with a plasticity model including the effects of *work hardening*. The plastic yield surface is described by the following equation which is a fit to the experimental data in Reference 8.

$$Y(Mb) = .00292 + .02598 \epsilon_p^{-.12233} \epsilon_p^2, 0 \leq \epsilon_p \leq .106$$

$$Y(Mb) = .0043, \epsilon_p > .106$$

where ϵ_p is the generalized plastic strain

Tensile failure is treated using the ultimate tensile failure criteria of $\sigma_t = .0043 Mb$, which is equivalent to a 10.6% ductility. Note that tensile failure is treated with a direct model which permits crack propagation.

A.3 Semi-Elliptical Coordinate Method

The new semi-elliptical approach involves the 2-D solution of the impact dynamics in the same x-y plane as is used in plane strain simulations (i.e., the plane which is defined by the velocity vector and the normal to the target surface at the impact point). Our approach differs from plane strain, however, in that an *elliptical* coordinate scheme is used in the governing equations of motion. Divergent motion (outside of the primary x-y plane) is thus taken into consideration in a manner which is analogous to azimuthal divergence in axisymmetric solutions. Use of the elliptical coordinate scheme in the target representation does not affect the impacting projectile geometry, which is effectively treated as an axisymmetric body.

Consider a rigid-projectile penetration through a thin plate. The projectile penetration path makes a trace (or carpet) on a horizontal plane at any depth, y , in the target. If the projectile is cylindrical, this trace is an ellipse with major and minor semi-axes of length "a" and "b" respectively. This elliptical approximation provides the necessary basis for an elliptical coordinate scheme with the elliptical parameter $c^2 = a^2 - b^2$ or $c = \sqrt{a^2 - b^2}$. In this elliptical system, the governing equations of motion are specified so as to take into account geometric divergence out of the primary (x,y) plane. Table A-3 compares the terms affecting divergence in axisymmetric, plane strain, and elliptical coordinate systems. Note in this table that the elliptical terms degenerate to the axisymmetric case when c becomes small relative to x .

Table A-3. Comparison of Axisymmetric, Plane Strain, and Semi-Elliptical Strain Rates and Equations of Motion

	Axisymmetric	Plane Strain	Semi-Elliptical
Strain Rate, $\dot{\epsilon}_{33} =$	\dot{x}/x	0	$\frac{\dot{x}x}{x^2 - c^2}$
$\rho \dot{x} = \frac{\partial \sigma_{11}}{\partial x} + \frac{\partial \sigma_{12}}{\partial y} +$	$\frac{\sigma_{11} - \sigma_{33}}{x}$	0	$\frac{(\sigma_{11} - \sigma_{33})x}{x^2 - c^2}$
$\rho \ddot{y} = \frac{\partial \sigma_{22}}{\partial y} + \frac{\partial \sigma_{12}}{\partial x} +$	$\frac{\sigma_{12}}{x}$	0	$\frac{\sigma_{12}x}{x^2 - c^2}$

An important aspect of the elliptical coordinate scheme is that every point in the primary plane on the obtuse side of the impacting body has a paired, or conjugate point on the acute side. Conditions at conjugate points are generally not the same for oblique impacts. (For normal impacts, conjugate points would have the same physical conditions.) Conjugate points are not coupled in the present formulation. This situation seems reasonably appropriate, at least for an initial formulation, since conditions on the obtuse and acute sides of an oblique impact are dissimilar and probably weakly coupled.

Conditions at conjugate points in the primary (x,y) plane of a solution provide the basis for estimating the stresses off of that plane. However, this aspect of the scheme has not yet been implemented. One obvious way to determine out-of-plane conditions is by interpolation around the ellipse between the conjugate points. Through such interpolation, the stresses throughout the 3-D field can be estimated.

APPENDIX B
PROJECTILE IMPACT ONTO THICK ALUMINUM TARGETS
MOUNTED AT 45° TO TRAJECTORY

TABLE OF CONTENTS

SECTION		PAGE
I	INTRODUCTION	1
II	EXPERIMENTAL PROCEDURE	2
III	RESULTS	6
IV	CONCLUSION AND SUMMARY	13

LIST OF ILLUSTRATIONS

FIGURE		PAGE
1.	Ballistic Range.	2
2.	Targets Simply Supported at 45° to Trajectory.	3
3.	50 cal. Ogive and Two-Piece Copper Sabot.	3
4.	Residual Velocity Measurement Stations.	4
5.	Momentum vs. Velocity for Shots Used to Determine V-50.	5
6.	Momentum Transferred as a Function of Impact Velocity.	7
7.	Framing Camera Record of Projectile Penetration through a Thick Target.	8
8.	Target for which Perforation Did Not Occur.	9
9.	Perforated Target.	9
10.	Deviation in Trajectory as a Function of Impact Velocity.	10
11.	Deviation in Trajectory as a Function of Residual Velocity.	10

LIST OF TABLES

TABLE		PAGE
1.	SHOT DATA	12

SECTION I

INTRODUCTION

Jet engine fan blades are frequently damaged when debris from the runway or other objects are ingested by the engine. Often, the impact can cause the fan blade to break into fragments which are also ingested by the engine. Computer programs can be a particularly efficient tool for analyzing the failure of both actual and proposed fan blade materials. However, before the results can be applied to a large class of impacting objects and fan blade materials, they must be verified for several cases by laboratory measurements. Therefore, a multi-phase program composed of computer and analytical techniques and experimental data was initiated to investigate the failure modes of fan blades.

During the first phase, projectile impacts onto fan blade materials were investigated. Computations of the momentum transfer were made with a two-dimensional Lagrangian wave propagation computer routine (WAVE-L). The momentum transfer for identical conditions was measured in the laboratory. Good agreement was obtained for impacts at 90° , but agreement was less satisfactory for impacts at oblique angles (60°). In this phase, the computations were extended to calculations of oblique impact of projectile cores with thicker targets closer to the perforation velocity. This report discusses the laboratory portion of this phase of the study.

Thick aluminum targets were mounted at 45° to trajectory and were impacted at velocities near V-50 (50% of the projectiles impacting at this velocity perforate the target). These conditions were difficult to simulate correctly for the computer and therefore provided a stringent test of the program.

SECTION II

EXPERIMENTAL PROCEDURE

Thick aluminum targets were impacted at an oblique angle with nondeformable ogives, and projectile velocity was measured before and after impact. The momentum transferred to the target was determined from the projectile mass and change in velocity. (A schematic of the ballistic range is shown in Figure 1.)

The targets were 12 mm thick plates (15 x 18 cm) of 6061-T6 aluminum. The plates were simply supported at an angle of 45° to trajectory as shown in Figure 2; the edges were free to rotate but the target could not displace.

The projectiles were reproductions of cores of 50 caliber AP (Armor Piercing) ammunition. They were hardened to Rockwell C 45-50 to coincide with the rigid projectile model used in the computer calculations. The ogive and a two-piece copper sabot are shown in Figure 3.

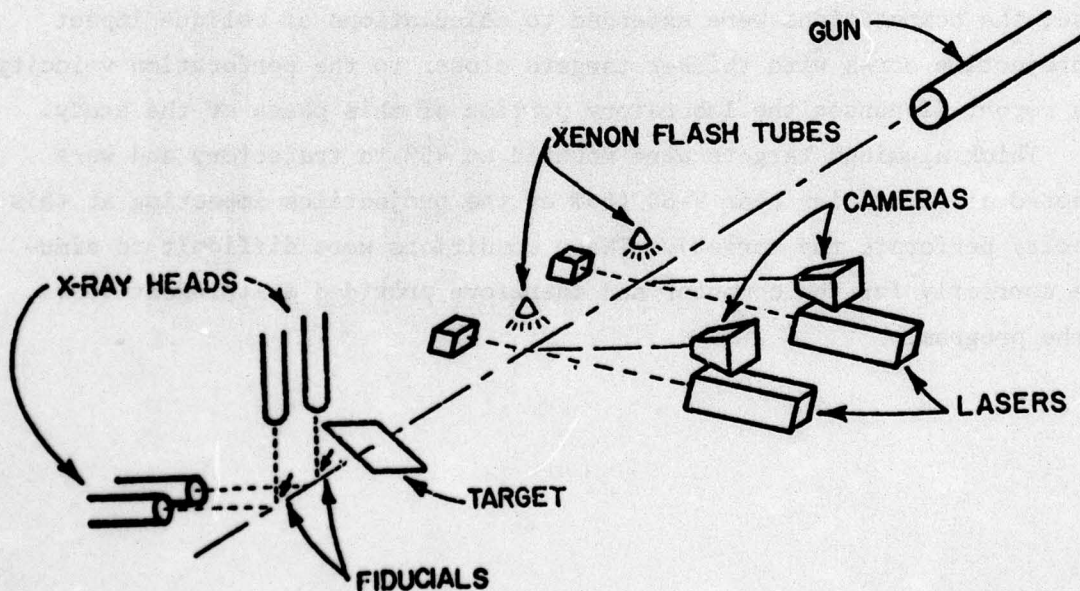


Figure 1. Ballistic Range.

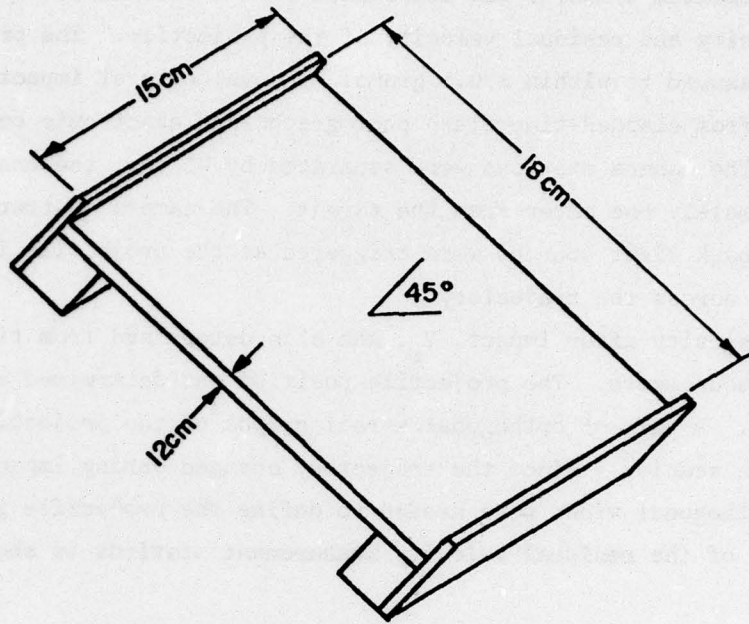
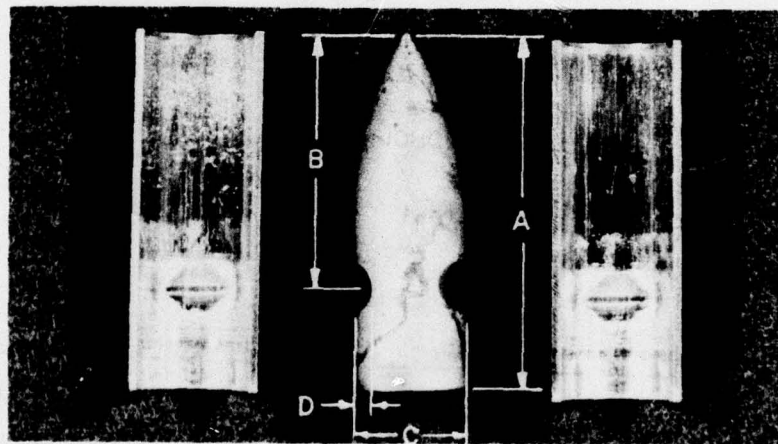


Figure 2. Targets Simply Supported at 45° to Trajectory .



A = 35.05 mm
 B = 25.15 mm
 C = 11.13 mm
 D = 2.36 mm

Figure 3. 50 cal. Ogive and Two-Piece Copper Sabot.

The momentum transfer was determined from measurements of the mass, impact velocity and residual velocity of the projectile. The projectile mass was measured to within ± 0.1 grams. The velocity at impact, V_i , was determined from elapsed-time flash photographs and electronic counter readings. The camera stations were separated by 45 cm; the nearest station was approximately one meter from the target. The camera shutters were left open, and spark light sources were triggered as the projectile interrupted laser beams across the trajectory.

The velocity after impact, V_r , was also determined from time and distance measurements. The projectile position was determined at two stations 15 cm apart. A pair of orthogonal x-radiographs of the projectile were made at each station. Since the trajectory changed during impact, the two pairs of orthogonal views were needed to define the projectile position. A schematic of the residual velocity measurement stations is shown in Figure 4.

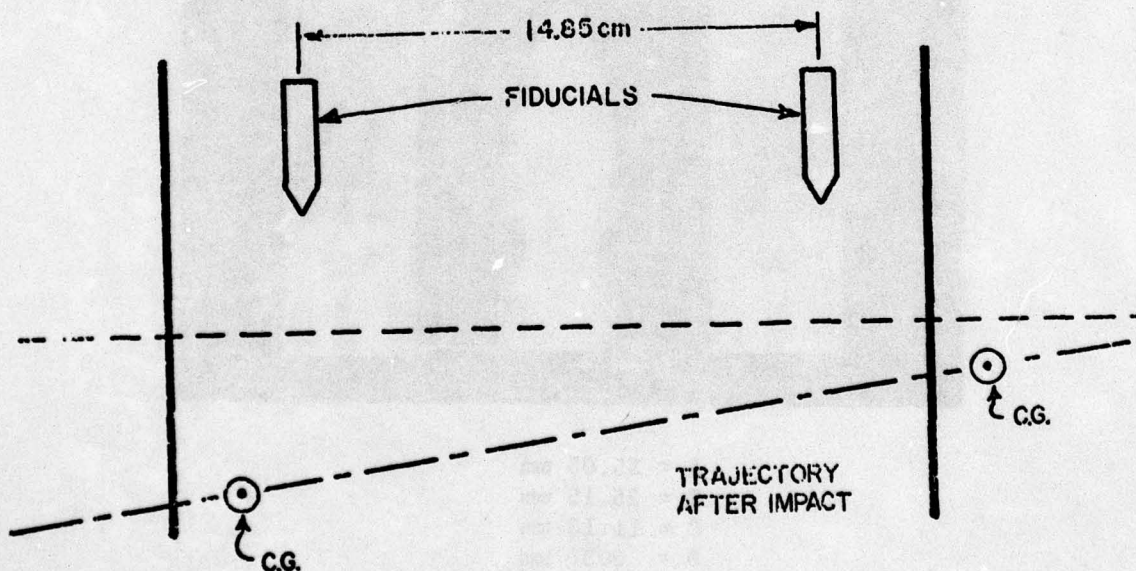


Figure 4. Residual Velocity Measurement Stations.

V-50 is the velocity at which the projectile has a 0.5 probability of penetrating the target. A series of nine shots was used to determine V-50. Projectiles first were fired at low velocities at which target perforation did not occur; the velocities were increased until perforation did occur. V-50 was defined as the average of six test velocities; the three highest velocities where perforation did not occur and the three lowest velocities where perforation did occur. V-50 was determined to be 474 m/s. The impact velocity and momentum transfer are plotted in Figure 5.

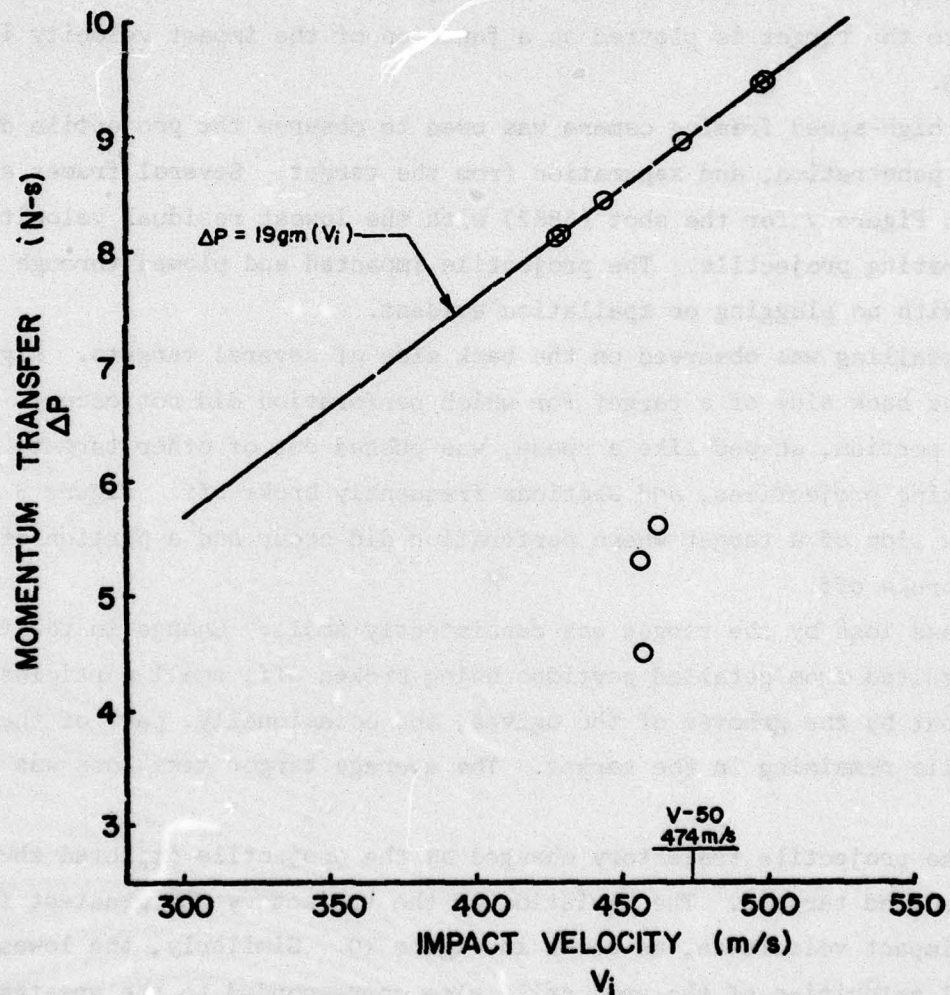


Figure 5. Momentum vs. Velocity for Shots Used to Determine V-50.

SECTION III

RESULTS

The following parameters were measured for this project: the impact and residual velocities of the projectile, the momentum lost by the projectile, the mass lost by the target, and the angular change in the trajectory of the projectile. The data are tabulated in Table 1 (at the end of this section) for the 12 shots for which sufficient information was available to calculate the momentum lost by the projectile. The momentum transferred to the target is plotted as a function of the impact velocity in Figure 6.

A high-speed framing camera was used to observe the projectile during impact, penetration, and separation from the target. Several frames are shown in Figure 7 for the shot (5862) with the lowest residual velocity of a perforating projectile. The projectile impacted and plowed through the target with no plugging or spallation evident.

Petalling was observed on the back side of several targets. Figure 8 shows the back side of a target for which perforation did not occur. The cracked portion, shaped like a spade, was pushed out of other targets by perforating projectiles, and sections frequently broke off. Figure 9 shows the back side of a target where perforation did occur and a portion of the target broke off.

Mass loss by the target was consistently small. Change in the target mass resulted from petalled portions being broken off, small particles being pulled out by the grooves of the ogives, and occasionally, part of the projectile remaining in the target. The average target mass loss was 0.16 grams.

The projectile trajectory changed as the projectile impacted the thick, angled targets. The deviation of the trajectory was greatest for lowest impact velocities, as shown in Figure 10. Similarly, the lowest residual velocities of the projectile also corresponded to the greatest deviation of the trajectory, as shown in Figure 11.

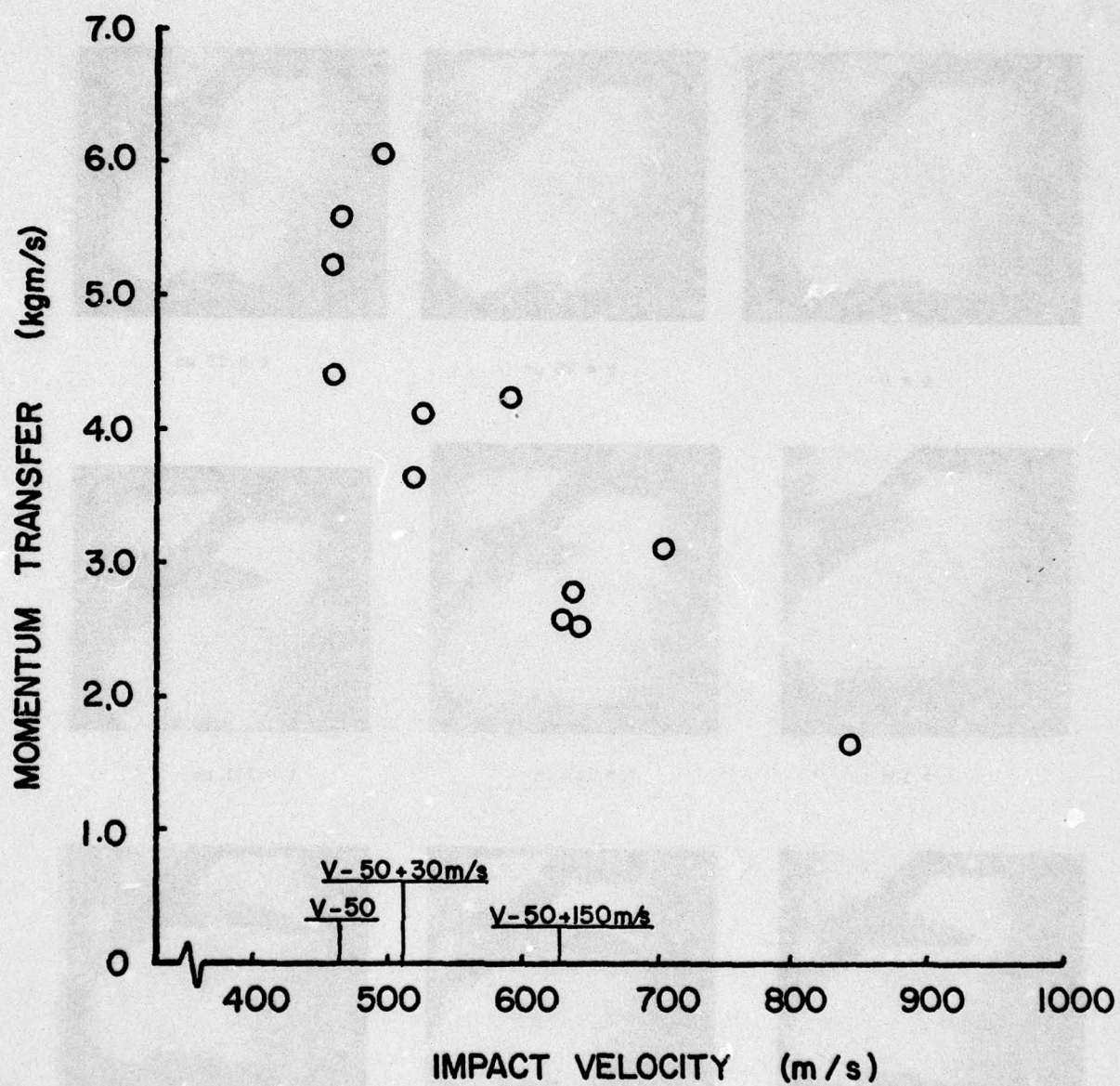


Figure 6. Momentum Transferred as a Function of Impact Velocity.

AD-A041 780

DAYTON UNIV OHIO RESEARCH INST
INVESTIGATION OF LOCAL DAMAGE AND IMPULSE DELIVERED TO TURBINE --ETC(U)
JAN 77 M ROSENBLATT, T R ISBELLE, P F FRY F33615-75-C-5052
AFML-TR-76-208 NL

UNCLASSIFIED

2 OF 2

ADA041 780



END

DATE
FILMED

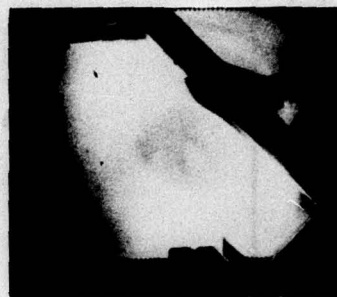
8-77



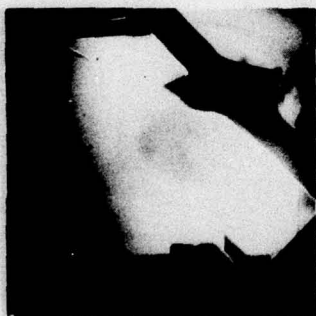
$t = 0$



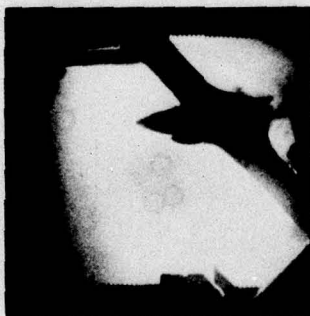
$t = 46 \mu s$



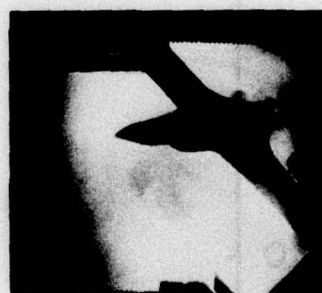
$t = 92 \mu s$



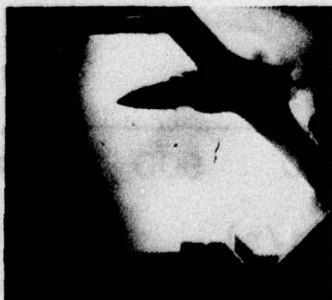
$t = 138 \mu s$



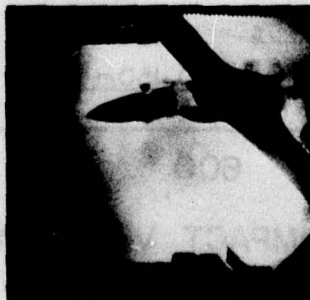
$t = 185 \mu s$



$t = 231 \mu s$



$t = 277 \mu s$



$t = 323 \mu s$



$t = 508 \mu s$

Figure 7. Framing Camera Record of Projectile Penetration through a Thick Target.



Figure 8. Target for which Perforation Did Not Occur.

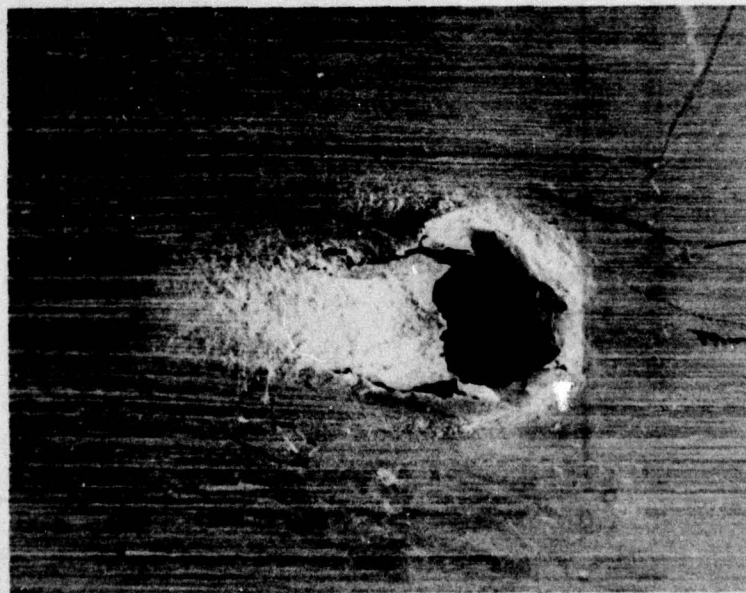


Figure 9. Perforated Target.

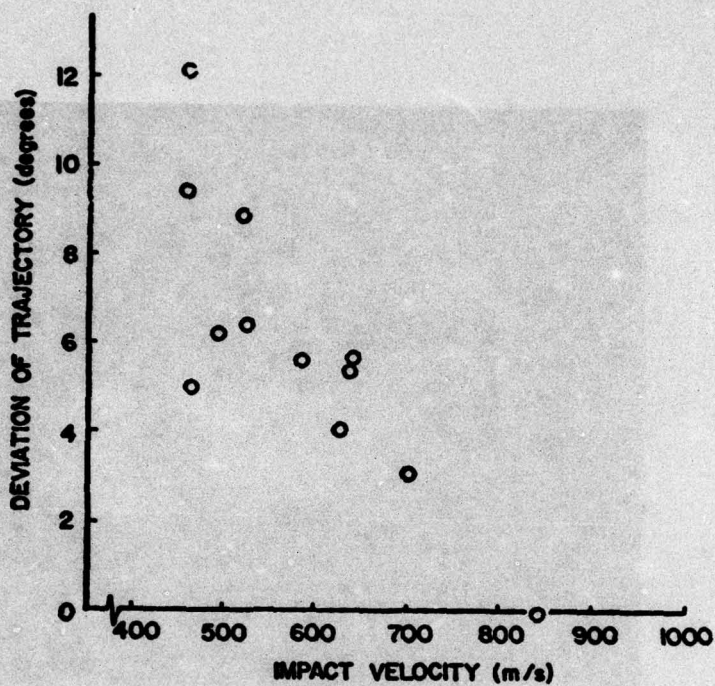


Figure 10. Deviation in Trajectory as a Function of Impact Velocity.

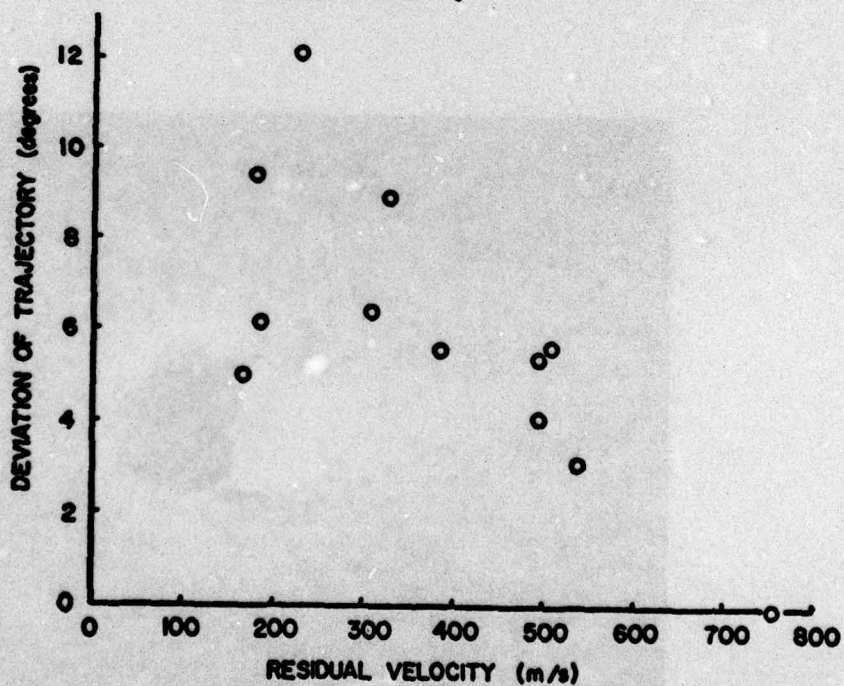


Figure 11. Deviation in Trajectory as a Function of Residual Velocity.

All of the factors that affect momentum transfer were held constant except the impact velocity. Nevertheless, scatter in the data is evident; at the lower impact velocities, similar projectile impact velocities result in widely different momentum transfers. A slight uncontrollable wobble of the projectile was noticed in the photographs used to determine V_i . This slight wobble (usually less than $\pm 2.8^\circ$) allowed the tip of the projectile to be slightly off trajectory. Thus, at the instant of impact a random moment was imparted to the projectile. The principal cause of scatter in the momentum transfer data is therefore considered to be the random surface forces between the projectile and the target during penetration, resulting from an uncontrollable wobble of the projectile at impact.

Errors in reading the film were estimated and their effects on the velocity calculations computed. Distances were read from the film to within $\pm .02$ cm and the actual distance between fiducials was determined to within $\pm .01$ cm. Calculations of the distance the projectile traveled between X-rays required eight measurements from the film: two projectile diameters (to find magnifications), two projectile lengths (to locate the center of gravity), and four measurements of the projectile position (from the center of gravity to a fiducial). Since the fiducial separation was known within $\pm .01$ cm and all of the other distances were measurable on the film to within $\pm .02$ cm, the projectile displacement between X-rays could be determined within $\pm .2$ cm. Typical time for the projectile to traverse the distance between X-rays was approximately 600 microseconds. Neglecting error in the counter, the velocity measurements were accurate within $\pm .3$ meters/second.

TABLE 1. SHOT DATA

Shot #	V_i (m/s)	V_r (m/s)	M (gm)	ΔP (kgm/s)	ΔM (gm)	θ (degrees)
5841	457	226	19.3	4.47	-0.05	12.1
5846	589	386	19.3	4.29	+0.07	5.6
5849	688	539	19.3	2.88	0.00	3.1
5850	493	182	19.3	6.01	-1.00	6.2
5852	637	492	19.4	2.81	-0.10	5.4
5854	519	330	19.5	3.69	-0.10	8.9
5855	628	495	19.6	2.60	0.00	4.1
5860	462	167	19.0	5.61	-0.01	5.0
5861	641	507	19.1	2.55	-0.12	5.7
5862	456	178	19.0	5.28	-0.30	9.4
5863	842	754	18.9	1.68	-0.20	0.0
5857	524	309	19.3	4.13	-0.05	6.4

V_i = impact velocity

V_r = residual velocity

M = projectile mass

ΔP = projectile momentum change

ΔM = target mass change

θ = change in projectile trajectory

SECTION IV

CONCLUSION AND SUMMARY

Impacts of 50 cal ogive projectiles onto thick aluminum targets mounted at an angle to trajectory were investigated. Impact and residual velocities and the changes in the trajectory during impact were measured. Projectile velocities near V-50 were of particular interest; they are characterized by low residual projectile velocities and large deviations in the projectile trajectory. Momentum transfer was determined to within $\pm 1.0\%$.

It is recommended that the tumble and spin of the projectile be measured after impact. Yaw of the projectile before impact should be eliminated, or at least measured. The projectile momentum transferred to the target varies for similar impact velocities. Projectile yaw at impact is considered to be a major cause of the variance.